Development in seismic interferometry for subsurface monitoring - an application to the 2011 Tohoku-oki earthquake -

博士論文

Development in seismic interferometry for subsurface monitoring – an application to the 2011 Tohoku-oki earthquake –

(地下構造モニタリングのための地震波干渉法の高度化
–2011 年東北地方太平洋沖地震への適用–)

髙木 涼太

平成 25 年

Doctoral Thesis

Development in seismic interferometry for subsurface monitoring – an application to the 2011 Tohoku-oki earthquake –

地下構造モニタリングのための地震波干渉法の高度化 –2011 年東北地方太平洋沖地震への適用–

Ryota Takagi

(髙木 涼太)

Department of Geophysics
Graduate School of Science
Tohoku University

Thesis Committee Members

Associate Professor	Tomomi Okada (Chair, Supervisor)
Professor	Toru Matsuzawa
Professor	Ryota Hino
Associate Professor	Hisashi Nakahara
Assistant Professor	Mare Yamamoto

2013

Acknowledgments

I would like to express my deep gratitude to Associate Prof. Tomomi Okada, my supervisor, for his support, guidance, and encouragement throughout this study. I would also like to express my deep gratitude to Associate Prof. Hisashi Nakahara for his specific suggestions, valuable advice, and deep discussion. I am deeply grateful to Prof. Toru Matsuzawa, Prof. Ryota Hino, Assistant Prof. Mare Yamamoto for their valuable comments and constructive discussion.

I am also deeply grateful to Visiting Prof. Akira Hasegawa and Emeritus Prof. Haruo Sato for their suggestions and constant encouragements. I would like to extend my thanks to Emeritus Prof. Hiromi Fujimoto, Profs. Takeshi Nishimura, Norihito Umino, Satoshi Miura, Dapeng Zhao, Shinji Toda, Associate Profs. Yasuo Yabe, Junichi Nakajima, Motoyuki Kido, Assistant Profs. Naoki Uchida, Yusaku Ohta, Takeshi Iinuma, Genti Toyokuni, Masahiro Ichiki, Ikuko Wada, and Ryosuke Azuma.

I would like to offer my special thanks to Associate Prof. Kiwamu Nishida of Earthquake Research Institute, the University of Tokyo, for his constructive comments and useful discussion. I would like to thank Associate Prof. Yoshihiro Ito of Disaster Prevention Research Institute, Kyoto Univertisy for his guidance and encouragements. I also appreciate the member of workshop on wave propagation and heterogeneous structure.

I owe a very important debt to Toshio Kono for his enormous contribution to data acquisition at Tono array. I am also thankful to Takashi Nakayama, Shuichi Suzuki, Satoshi Hirahara, Yuko Daikoku, Mika Iibuchi, and the member of the Research Center for Prediction of Earthquakes and Volcanic Eruptions and the Solid Earth Physics Laboratory, Tohoku University.

This study was supported by JSPS KAKENHI Grant Number 11J03229. I acknowledge the National Research Institute for Earth Science and Disaster Prevention, Japan (NIED) for providing the KiK-net waveform data. I also acknowledge the Nationwide Ocean Wave information network for Ports and Harbours (NOWPHAS) for providing ocean wave data. The figures in this manuscript were drawn using the Genetic Mapping Tools (GMT) [Wessel and Smith, 1991].

Special thanks to Keisuke Yoshida, Satoshi Kurita, Toshiki Kaida, Masaki Akatsuka, Yo Kitamura, Takahiro Yanada, Takayoshi Watanabe, Shiori Ii, and Shoko Koga. I also appreciate Ayumi Sasaki for her hearty cheer. Last, I am really deeply grateful to my parents for their warm encouragements and continuous support.

Abstract

Seismic interferometry is a method to retrieve Green's function by cross-correlating passive wavefield such as ambient noise and coda wave. Green's function contains information of wave propagation. Thus, we can explore subsurface structure using the Green's function retrieved by seismic interferometry. An advantage of seismic interferometry is repeatability of Green's function retrieval. Meanwhile, subsurface monitoring is one of important issues in seismology. That is because the measurement of the temporal variation in subsurface structure will give us useful information about change in soil condition, crack density or aspect ratio, fluid distribution, and/or static stress. For reliable measurements of the temporal change in subsurface structure by seismic waves, the source of the seismic waves must be repeatable and/or stable. Therefore, seismic interferometry is a useful tool to monitor subsurface structure, giving repeatable and/or stable sources by cross-correlation functions of ambient noise or coda wave.

On 11 March 2011, the M9.0 Tohoku-Oki earthquake took place off NE Japan which various seismic observations cover. In order to deepen our understanding of the temporal change in subsurface structure related to the Tohoku-Oki earthquake, I deal with four subjects. The key words of the present study are three-component observation and array observation. I use two kinds of data: KiK-net and Tono array. Each KiK-net station has two of three-component accelerometers both on the surface and the bottom of borehole, configurating a vertical array. Tono array is a small-aperture, three-component, and broadband seismic array.

First, in Chapter 2, using the cross-correlation functions of coda wave observed at two horizontal components of KiK-net vertical array, I examine temporal change in shear velocity and polarization anisotropy related to the Tohoku-Oki earthquake. After the Tohoku-Oki earthquake, shear velocity within near surface layer decrease by up to 5-10% in the wide are in NE Japan. In contrast, the fast directions of polarization anisotropy do not show significant changes, which suggest that the static stress change due to coiseismic slip is not sufficient to change the orientations of cracks and/or the principle axes of crustal stress field. This study adds new information of the temporal change in subsurface structure related to the 2011 Tohoku-Oki earthquake.

Second, in Chapter 3, using the cross-correlation functions of ambient noise observed at vertical components of Tono array, I examine the frequency dependence of the coseismic velocity change related to the Tohoku-Oki earthquake in a wide frequency range of 0.3-1.9 Hz with a high frequency resolution of 0.18 Hz. Below 1.1 Hz, the coseismic phase velocity reduction linearly increases with respect to frequency, which is indicative of the near-surface velocity reduction. However, above 1.2 Hz, the phase velocity change shows more complicated behavior. Here, I develop a method to estimate the phase velocity and the noise source distribution simultaneously based on the spatial auto-correlation (SPAC) method. Based on the method, I show the suppression of the apparent velocity change due to the temporal

change in the noise source distribution. This study shows that array observations of ambient noise have a potential to measure the temporal velocity change in a wide frequency band with a high frequency resolution and to suppress the effect of the change in noise source distribution by the simultaneous measurement of the phase velocity and the noise source distribution.

Third, in Chapter 4, using the cross terms of the cross-correlation tensor of ambient noise, I develop a novel method to separate body and Rayleigh waves. The method is based on a theoretical discovery that vertical-radial (ZR) and radial-vertical (RZ) components of the cross-correlation tensor have the opposite signs for elliptic Rayleigh wave and the same signs for rectilinear P wave. Accordingly, I separate P and Rayleigh waves by just taking sum and difference of ZR and RZ correlations. Furthermore, the application to Tono array data validates the effectiveness of the method. The method can be performed without any knowledge of velocity structure, using only two stations on the free surface, even in the case of anisotropic wave incidence, and with the quite simple procedure. This study proposes an effective use of three-component observation of ambient noise.

Fourth, in Chapter 5, using cross-correlation tensor of ambient noise observed at three components of Tono array, I reveal the composition of ambient noise. For estimating the composition ratio between Rayleigh, Love, and P waves, I extend the SPAC method to body wave incidence. The extended SPAC method shows a good agreement between the theoretical and observed cross spectra. The obtained composition of ambient noise significantly changes at 1 Hz. While the P wave composition in total power is 5-15% and the lowest one below 1 Hz, the P wave composition suddenly increases above 1 Hz and reaches 50% and the highest one in those of three wave modes. The change at 1 Hz is attributed to the attenuation of high-frequency surface waves. This study demonstrates the effective use of the three-component array allowing us to decompose the ambient noise wavefield and to reveal the composition of ambient noise. The significant P wave above 1 Hz revealed in Chapter 5 is the cause of the complicated behavior of the phase velocity change in Chapter 3.

Seismic interferometry is a powerful tool for subsurface monitoring. However, we should take account of the effects of change in noise source distribution and the contamination of other wave modes to correctly interpret observed temporal variations in subsurface properties as shows in Chapter 3 and Chapter 5. Moreover, the present study shows that effective use of three-component array is a key for detecting change in not only seismic velocity but also anisotropy, for minimizing the effect of temporal change in noise source distribution, for measuring broadband velocity change with a high frequency resolution, for separating body and Rayleigh waves effectively, and for understanding the composition of ambient noise.

Contents

Acknowledgment **i**

Abstract **iii**

Contents **v**

1. General Introduction **1**

1.1. Seismic Interferometry 1

1.2. Subsurface Monitoring 2

1.3. Objective 3

2. Temporal change in shear velocity and polarization anisotropy related to the 2011 M9.0 Tohoku-Oki earthquake examined using KiK-net vertical array data **5**

2.1. Introduction 6

2.2. Data and Method 6

2.3. Results 7

2.4. Discussion and Conclusions 9

3. Monitoring seismic velocity structure before and after the 2011 M9.0 Tohoku-Oki earthquake using array observation of ambient noise **19**

3.1. Introduction 20

3.2. Data and Cross-Correlation Function 20

3.3. Measurement of Phase Velocity and Noise Source Distribution 22

3.4. Annual Average of Phase Velocity and Noise Source Distribution 24

3.5. Temporal Change in Phase Velocity and Noise Source Distribution 24

3.6. Discussion 25

3.7. Conclusions 26

4. Separating body and Rayleigh waves with cross terms of the cross-correlation tensor of ambient noise **39**

4.1. Introduction 40

4.2. Characteristic Cross-Correlation Tensor 41

4.3. Cross Spectra of Uncorrelated Plane Waves 43

4.4. Relationship between ZR and RZ Cross Spectra 45

4.5. Representation of Cross Spectra for Isotropic Incidence 47

4.6. Representation of Cross Spectra for Anisotropic Incidence 49
4.7. Application to Tono Array Data 51
4.8. Discussion and Conclusions....52
Appendix 4.A: Response Functions for P and SV Wave Incidences....53
Appendix 4.B: Derivation of Cross Spectra for Anisotropic Wave Incidence 54

5. Composition of ambient noise at Tono array 63
5.1. Introduction....64
5.2. Tono Array Data 66
5.2.1. Ambient Noise at Tono Array 66
5.2.2. Observed Cross-Correlation Tensor 66
5.3. SPAC Method Extended to Body Wave Incidence....68
5.3.1. Theoretical Cross-Spectral Tensor 68
5.3.2. Fitting the Theoretical Cross-Spectral Tensor to the Observed Cross-Spectral Tensor ...70
5.4. Composition of Ambient Noise 73
5.4.1. Annual Average in 2010....73
5.4.2. Temporal Variation in 2010....74
5.5. Discussion 75
5.6. Conclusions....77

6. Discussion 93
6.1. Answer to the Question in Chapter 3 93
6.2. Future Work 94

7. Conclusions 97

References 99

1. General introduction

1.1. Seismic Interferometry

Seismic interferometry is a method to extract impulse response by cross-correlating observed wavefield (Figure 1.1). The impulse response is also termed Green's function. Thus, with the term "retrieval", we also refer to seismic interferometry as Green's function retrieval. Since Green's function contains information of wave propagation within a medium, seismic interferometry allows us to investigate properties of the medium using the retrieved Green's function.

The basement of seismic interferometry dates back to an early work by Aki [1957] known as the spatial auto-correlation (SPAC) method. Aki [1957] proposed that the cross spectra of random and stochastic wavefield observed at two stations retrieve the information of wave propagation between two stations and deduce the dispersion curve of surface wave which composes of the random wavefield. Another early work was made by Claerbout [1968]. Claerbout [1968] proposed that the auto-correlation of a seismogram on a free surface retrieves a reflection response due to impulsive source on the free surface, which is known as daylight imaging.

These early works have been spotlighted again since a series of studies in helioseismology [Duvall et al., 1993], ultrasonic acoustics [Weaver and Lobkis, 2001, 2002], and seismology [Campillo and Paul 2003; Shapiro and Campillo, 2004]. Duvall et al. [1993] showed Green's function retrieval of acoustic wave traveling in the sun from cross-correlation functions of observed wavefield. Weaver and Lobkis [2001, 2002] succeeded in retrieving Green's function from cross-correlation of diffused ultrasonic wavefield. In seismological field, multiply scattered coda waves and ambient noise are candidates of the diffused wavefield. Campillo and Paul [2003] demonstrated that Green's function of surface waves emerges from long-range cross-correlation functions of diffused coda waves. Shapiro and Campillo [2004] showed that Green's function was also retrieved from cross-correlation functions of ambient noise. From these pioneering studies, it took little time to apply the Green's function retrieval to subsurface structure exploration. Shapiro et al. [2005] and Sabra et al. [2005] performed a surface wave travel-time tomography based on ambient noise cross-correlation. Such surface wave tomography using Green's functions retrieved from ambient noise, called ambient noise tomography, has been widely applied to explore subsurface heterogeneities in local [e.g., Brenguier et al., 2007], regional [e.g., Yao et al., 2006; Yang et al., 2007; Nishida et al., 2008a], and global scales [Nishida et al., 2009]. Seismic interferometry is also applicable to body wave. Pseudo reflection response retrieved from cross-correlation function allows us to make reflection image of subsurface structure using traditional seismic reflection techniques [e.g., Schuster et al., 2004; Abe et al., 2007; Tonegawa et al., 2009].

Green's function retrieval has also been developed by theoretical studies. Lobkis and Weaver [2001] demonstrated the emergence of Green's function from diffused wavefield based on the equipartition of

normal modes. Derode et al. [2003] showed Green's function retrieval based on the principle of time reversal. Snieder [2004] derived Green's function retrieval from multiply scattered waves based on the stationary phase method. Wapenaar [2004] and Wapenaar and Fokkema [2006] used reciprocity theorem and the principle of time reversal for deriving Green's function retrieval. Nakahara [2006] connected the frequency domain SPAC representation and the time domain Green's function, showing a relationship between Aki's SPAC method and seismic interferometry. Figure 1.2 summarizes the theory and examples of the applications of seismic interferometry.

1.2. Subsurface Monitoring

Monitoring the seismic velocity in the Earth's crust is one of primary targets of seismological studies. The seismic velocity is affected by stress accumulation and pore pressure change, which could directly relate to the occurrence of earthquakes. In addition, estimating site effects after large earthquakes in shallow layers is important in order to accurately predict strong ground motion.

For reliable monitoring of subsurface structure using seismic waves, the source of seismic wave has to be repeatable in time. Doublet earthquakes and repeated explosions are such repeatable passive and active sources, respectively. Using doublet earthquakes and active explosions, temporal velocity changes associated with large earthquakes and volcanic activity have been observed in several previous studies. Poupinet et al. [1984] observed a velocity decrease after the Coyote Lake earthquake in 1979 using moving window cross-spectral analysis for coda wave of an earthquake doublet observed at the same station. Snieder [2002] developed a method using multiply scattered waves for measuring weak change of seismic velocity, named coda wave interferometry. Peng and Ben-Zion [2006] detected coseismic velocity drops and postseismic recovery, applying coda wave interferometry to repeating earthquakes clusters around the fault zones of the 1999 İzmit and Düzce earthquakes. Nishimura et al. [2005] applied a similar method to repeated active experiments near Mt. Iwate and detected a velocity decrease of 1%. Nakamura et al. [2002] revealed a P wave velocity change of at least 1% in shallow regions associated with the 1998 M6.1 Shizukuishi earthquake in NE Japan, using earthquake doublets and active experiments. Based on observations of the delay of the coda wave, they also reported that crustal heterogeneity at greater depths should be changed.

Seismic interferometry is also a powerful tool providing repeatable and/or stable sources because we can retrieve Green's function from passive wavefield. In particular to ambient noise, Green's function can be extracted anytime and anywhere. Sens-Schönfelder and Wegler [2006] measured seasonal variations of seismic velocity correlated to precipitation at Merapi volcano by applying coda wave interferometry to Green's function retrieved from ambient noise by seismic interferometry, called passive image interferometry. Brenguier et al. [2008] observed a coseismic decrease and post seismic recovery in the seismic velocity associated with the 2004 Mw6.0 Parkfield earthquake from ambient noise correlation. A

coseismic velocity change up to 0.5% was also detected after the 2004 Mw6.4 Mid-Niigata earthquake using auto-correlation and cross-correlation of ambient noise [Wegler and Sens-Schönfelder, 2007; Wegler et al., 2009].

Green's functions extracted from cross-correlation or deconvolution of coda waves are also used for subsurface monitoring. Sawazaki et al. [2006, 2009] applied seismic interferometry to KiK-net vertical array and reported a shear velocity decrease within a shallow layer up to 100 m from the surface associated with the 2000 Mw6.0 Western Tottori earthquake. Yamada et al. [2010] also found velocity decreases in the source region of the 2008 Iwate-Miyagi Nairiku earthquake by the vertical array method. The vertical array analysis based on seismic interferometry provides information of velocity change within near-surface layer from borehole to surface.

Some studies also reported the location of velocity change related to large earthquakes. Takagi et al. [2012] localized coseismic velocity change in the focal region using direct part of noise correlation associated with the 2008 Iwate-Miyagi Nairiku earthquake. Takagi et al. [2012] also discussed that the shear velocity decrease up to 5% obtained by the vertical array method is consistent with the phase velocity change obtained by the ambient noise correlation because of the sensitivity kernel of surface wave, suggesting that seismic velocity change is concentrated in near surface up to a few hundred meters depth. For the same earthquake, Hobiger et al. [2012] also estimated location of velocity change using a tomographic method based on the delta-like sensitivity kernel of diffused wave.

1.3. Objective

On 11 March 2011, the 2011 M9.0 Tohoku-oki earthquake occurred off northeast Japan which various seismic observations cover. In order to deepen our understanding of temporal change related to the Tohoku-Oki earthquake, I deal with four subjects. In Chapter 2, for adding new information of structural change, I examine temporal change in both shear velocity and polarization anisotropy within near-surface layer up to a few hundreds meters depth using KiK-net vertical array. In Chapter 3, for giving a constraint of depth extent of the velocity change, I revel frequency dependence of phase velocity change in wide frequency band and with high frequency resolution. In Chapter 3, I also address the problem of apparent velocity change due to change in noise source distribution. The three-component analysis will be also useful to investigate temporal change in subsurface structure. In Chapter 4, based on wave theory, I clarify the characteristics of the full-component cross-correlation tensor. I develop a novel method to separate P and Rayleigh wave with cross terms of the cross-correlation tensor of ambient noise. In Chapter 5, for understanding the nature of ambient noise, I reveal the composition ratio of ambient noise at Tono array.

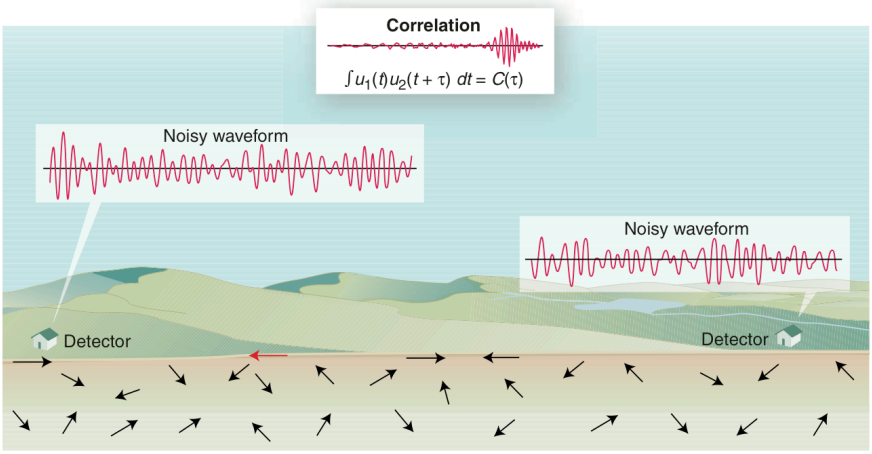

Using noise in seismology. When a diffuse wave field is generated by distant sources and/or by multiple scattering, detectors report random signals. Occasionally a ray (for example, the one shown in red) passes through both detectors. As a result, the signals are weakly correlated.

Figure 1.1 Concept of seismic interferometry [Weaver, 2005]

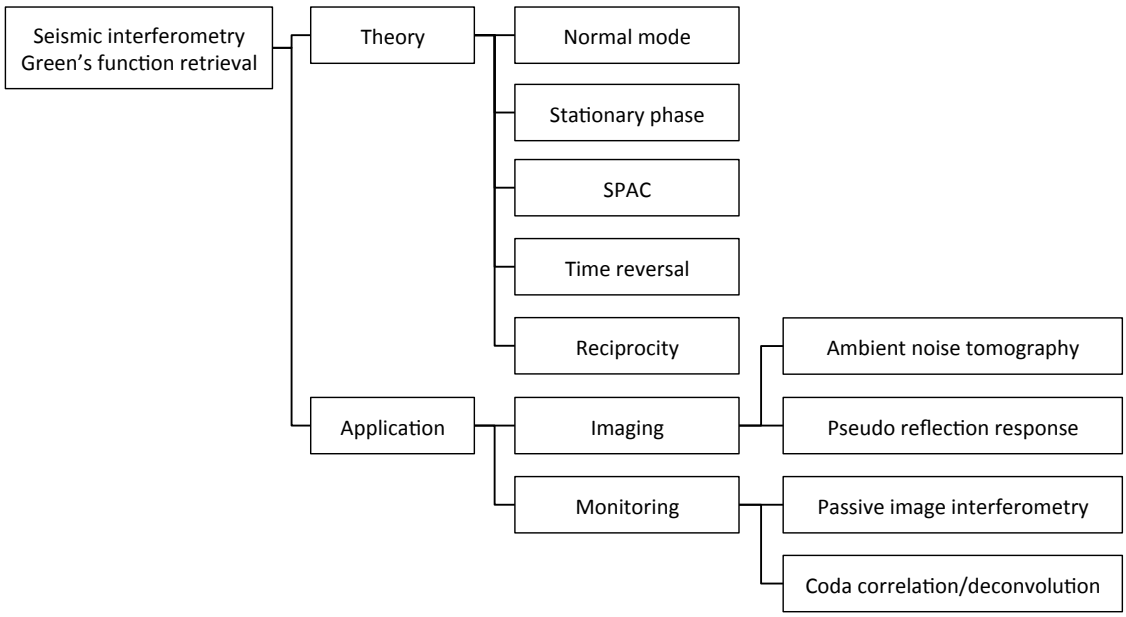

Figure 1.2 Theory and examples of applications of seismic interferometry. We can apply various seismological methods to retrieved Green's function for subsurface imaging and monitoring.

2. Temporal change in shear velocity and polarization anisotropy related to the 2011 M9.0 Tohoku-Oki earthquake examined using KiK-net vertical array data

Ryota Takagi[1] and Tomomi Okada[1]

[1]Research Center for Prediction of Earthquakes and Volcanic Eruptions, Graduate School of Science, Tohoku University, Sendai, Japan.

Summary

The M9.0 Tohoku-Oki earthquake took place off NE Japan, which is covered by a dense seismic network. In particular, KiK-net observed the strong motions of the main shock and numerous aftershocks both on the ground and at the bottom of boreholes of a few hundred meters deep. We applied cross-correlation analysis to the coda part of a seismogram observed by KiK-net and estimated not only the temporal change in shear velocity but also the change in polarization anisotropy between the bottom of the borehole and the ground. The shear velocity was suddenly reduced by 5 to 10 % after the Tohoku-Oki earthquake over a wide area of NE Japan, which is consistent with the results of a previous study. Although some stations also reveal a change in polarization anisotropy, the polarization anisotropy change is smaller than the velocity change, which may suggest that the static stress change due to the coseismic slip on the Pacific plate is not large enough to change the crack orientation and/or the direction of the deviatoric stress in the land area of NE Japan.

2.1. Introduction

Seismic velocity changes associated with large earthquakes have been observed from several types of data, such as repeating earthquakes, ambient noise, and coda waves. Repeating earthquakes are suitable for the detection of temporal change by comparing waveforms of different time periods because the locations of the hypocenters of these earthquakes are the same and the seismic waves pass though the same region [e.g., Poupinet et al., 1984]. Repeated active experiments can be used as an analogy for repeating earthquakes [e.g., Nishimura et al., 2000]. Recently, with the development of theoretical and observational seismic interferometry, ambient noise has provided powerful data for monitoring the subsurface structure [Brenguier et al., 2008; Wegler et al., 2009]. In addition, interferometric analysis of earthquake coda waves enables estimation of the temporal variation of seismic velocity and site response [Sawazaki et al., 2009]. Sawazaki et al. [2009] analyzed the coda wave observed at a vertical array of KiK-net and found that the velocity of the wave decreased as a result of the 2000 Western Tottori Earthquake. The advantage of the vertical array is that a velocity change within a shallow layer can be confirmed, which could be a major contribution to velocity changes in the crust.

Another advantage of the vertical array is the ability to directly measure polarization anisotropy [Miyazawa et al., 2008]. On 11 March 2011, the M9.0 Tohoku-Oki earthquake occurred near the nationwide KiK-net network. Such a large earthquake can cause changes in seismic velocity or anisotropy due to, e.g., strong motion and stress changes. We investigate the temporal change in seismic velocity and polarization anisotropy using KiK-net vertical array data. Nakata and Snieder [2011] reported a coseismic velocity change based on deconvolution analysis using KiK-net data. In the present study, we focus not only on the velocity change, but also on the polarization anisotropy change.

2.2. Data and Method

The KiK-net is a nationwide network that is used to observe strong ground motion, and is operated by the National Research Institute for Earth Science and Disaster Prevention (NIED) [Okada et al., 2004]. Each KiK-net station is equipped with two accelerometers. One is situated on the ground and the other is situated at the bottom of a borehole of 100 to 3,000 m in depth. We analyzed the earthquake data observed by 135 KiK-net stations in NE Japan from 2000 to December 2011. The depths of boreholes of 117 stations are smaller than 300 m and the deepest borehole of all stations used in the present study is 2000 m.

Since each sensor has three orthogonal components, we can compose waveforms for any polarization direction. After applying a second-order Butterworth filter with a passing frequency band of 4 to 16 Hz, we composed the waveforms from the bottom sensor and the surface sensor for the same polarization angle by rotating the two horizontal components data. We then computed a CCF (cross-correlation function) in frequency domain and applied an inverse Fourier transform. We also computed the CCF

between vertical components of the bottom and the surface sensor. The time window used in the present study starts from twice the S-wave travel time and has a length of 10.24 s. We can ignore the variation in the incident angle because the coda wave is randomly scattered by the inhomogeneous structure. Therefore, the coda wave is suitable for the detection of temporal variation [Sawazaki et al., 2009; Nagaoka et al., 2010]. In order to enhance the temporal resolution of the CCFs, we expanded the CCFs in a Fourier series and interpolated with a sampling frequency of 25.6 kHz.

We selected earthquake records for which the epicentral distance is smaller than 300 km, the signal-to-noise ratio is larger than 3, and the maximum accelerations at both the borehole sensor and the surface sensor are smaller than 50 gal.

Figure 2.1 shows an example of CCFs for the N-S direction, the E-W direction and the U-D direction at station IBRH14 and FKSH14 (see Figure 2.5 for the station locations). The CCFs for the horizontal directions at both stations have clear peaks near the theoretical travel times of S-wave based on logging data. In addition, at FKSH14, the CCF for the vertical direction shows the peak corresponding to P-wave. We could extract S-wave and P-wave from the cross-correlation of the coda part of the S arrival. The CCF for the vertical direction at IBRH14 shows the zero-lag peak because the wavelength of P-wave (approximately 200 m at 16 Hz) is larger than the length of the borehole (100 m). In this study, in order to examine the temporal change in shear velocity and polarization anisotropy of shear wave, we used the extracted S-wave from CCFs for the horizontal directions. Although we did not use the extracted P-wave, we would like to note that the information of P-wave would add valuable information to temporal change of subsurface structure. The peak time for the N-S direction lags 3 msec from that for the E-W direction at IBRH14 (Figure 2.1(c)). This indicates that the shear wave polarized in the E-W direction is faster than that polarized in the N-S direction, i.e., polarization anisotropy. Figure 2.1(d) is a lineup of individual CCFs for the N-S direction at IBRH14. This figure shows that the cross-correlation of the coda wave is also stable in time as the deconvoution waveform used by Nakata and Snieder [2011].

2.3. Results

First, we computed the shear velocity as a function of polarization angle over several time periods by selecting the maximum amplitudes of the averaged CCFs (Figure 2.2). As shown in Figure 2.1, the shear velocity in the E-W direction is faster than that in the N-S direction at IBRH14, where the shape of the plot does not change over several time periods, which means that the estimated polarization anisotropy is stable and does not vary with time. However, the extent of the plot becomes smaller after 11 March 2011, which means that the average shear velocity decreases after the Tohoku-Oki earthquake. In contrast, at FKSH14, the polarization angle rotates from the N-S direction to the E-W direction and the velocity decreases after the earthquake. At FKSH12, the plot becomes narrower. Therefore, the intensity of the polarization anisotropy increased after the earthquake at FKSH12.

The temporal variation of the seismic velocity and the anisotropy could be enhanced by using a moving window. We used a moving window of 10 events with an overlap of five events and averaged the CCFs over each window. In order to prevent the selection of neighboring peak of CCFs, we estimated the travel time from the relative time shift, which gives the maximum cross-correlation between the moving windowed CCF and the reference CCF. The reference CCF was computed by stacking the CCFs over all events and over all polarization directions. The time window to compute the cross-correlation is centered at the peak time of the reference CCF and has a duration of 0.25 s. The moving averaged CCFs are stable in time and the cross-correlation coefficients between the reference and the moving averaged CCFs within the time window are larger than 0.9 (Figure 2.3). Figure 2.4 depicts the temporal variations of the fast direction, the intensity of the anisotropy, and the azimuthal average of shear velocity at FKSH14, FKSH12, and IWTH03. The intensity of the anisotropy is defined as a percentage of the maximum velocity relative to the minimum velocity. Before the 2011 Tohoku-Oki Earthquake, the fast directions at FKSH14 are distributed in and around 0° or 180°, which is the N-S direction. After the event, the fast direction rotates to the E-W direction by approximately 60°. The intensity of the anisotropy at FKSH14 does not exhibit a clear coseismic change. In contrast, at FKSH12, we observed a coseismic increase in intensity without rotation of the fast direction. A coseismic increase of the intensity similar to that at FKSH12 is also observed at IWTH03. At the three stations, clear velocity decreases of 5 to 10% were observed at the occurrence time of the earthquake. The amplitude of the velocity decrease is consistent with the results reported by Nakata and Snieder [2011]. Postseismic recoveries of velocity changes are also recognizable. In particular, at IWTH03, the shear velocity has fully recovered after seven months.

Figure 2.5 shows the spatial distribution of the fast direction, the change of the anisotropy intensity, and the velocity change before and after the 2011 Tohoku-Oki earthquake. The fast directions, the intensity change, and the velocity changes are computed by averaging the temporal variations shown in Figure 2.4. Most stations do not exhibit a clear change of the fast direction after the earthquake except for a significant coseismic rotation at FKSH14. Although the intensity changes are also small, some changes are distributed more widely than the direction change. In contrast to the small change in anisotropy, the velocity decreases are distributed over a wide area of NE Japan. In particular, large coseismic decreases are observed near the Pacific coast. The distribution of the coseismic velocity change is similar to the results reported by Nakata and Snieder [2011]. Here, the coseismic velocity changes are computed based on the averages of relative velocity changes of two time periods from 1 January 2009 to 11 March 2011 and from 11 March 2011 to 11 April 2011 in order to remove the effect of the postseismic recovery and large inland earthquakes, such as the 2008 Iwate-Miyagi Nairiku Earthquake (M7.2) and the M7.0 event in the southeastern part of Fukushima prefecture.

2.4. Discussion and Conclusions

First, we discuss the velocity change. The estimated velocity change represents the reduction in shear modulus near the surface within a few hundred meters. The decrease in near-surface velocity could be interpreted as being caused by damage due to strong ground motion [e.g., Sawazaki et al., 2009]. The large coseismic drop observed near the Pacific coast is consistent with the ground acceleration (Figure 2.6(a)). Figure 2.7(a) depicts the relationship between the peak ground acceleration (PGA) on the surface and the velocity change. The positive correlation between PGA and fractional velocity change, dv/v, implies that the main factor related to the velocity decrease is the strong ground motion. The variation might be caused by near-surface geology, as suggested by Nakata and Snieder [2011]. We also plotted the travel time shift of the CCFs as a function of the maximum value of the dynamic strain change in Figure 2.7(b). The maximum value of the dynamic strain change is roughly proportional to the amplitude of seismic waves [Love, 1927] and estimated by dividing the peak ground velocity (PGV) by average shear velocity up to 30 m depth (i.e., V_{S30}) based on logging data. Figure 2.7(b) shows clearer correlation between the dynamic strain change and the travel time shift with the cross-correlation coefficient of 0.6, suggesting that the dynamic strain is a better indicator of the strong motion for seismic velocity change. In Figure 2.7(b), we used the travel time shift, dt, instead of dv/v. This is because the dv/v depends on the depth of boreholes in the case of vertical inhomogeneous velocity change. We also checked the relationship between the depth of boreholes and the travel time shift at five stations in the Ibaraki prefecture (Figure 2.7(c)). We selected the five stations because the dynamic strain changes are comparable and these stations have boreholes with different depths. The dynamic strain changes at IBRH12, IBRH15, IBRH16, IBRH17, and IBRH18 are 7.1×10^{-4}, 7.9×10^{-4}, 4.8×10^{-4}, 9.1×10^{-4}, and 5.2×10^{-4}, respectively. At the five stations, the variation of the travel time shifts is smaller than 34% and the travel time shifts are independent of the depths of boreholes. The almost constant time shifts at the five stations regardless of different depths of boreholes might suggest that major velocity decrease is localized in shallow layer up to 100 m at least at the these stations.

In contrast to the velocity change, the change in anisotropy is small. The polarization anisotropy in the crust can be classified as either stress-induced anisotropy or structural anisotropy [Boness and Zoback, 2006]. Stress-induced anisotropy indicates that deviatoric stress causes the preferred crack orientation, which results in polarization anisotropy parallel to the maximum horizontal stress. Stress-induced anisotropy dominates in rocks with randomly oriented fractures, such as granite. Structural anisotropy is attributed to the alignment of parallel planar features, such as parallel sedimentary bedding planes, which dominate in sedimentary rocks such as shale and silt. According to logging data, FKSH14 consists of a thick sand gravel layer and silt and sandstone. Such soft rock may also be strongly affected by the strong motion. Therefore, the large strong motion might cause the change in polarization anisotropy at FKSH14 as a result of crack generations, where the estimated dynamic strain change is 3.1×10^{-3} at FKSH14.

Nakata and Snieder [2012a] reported that the near-surface anisotropy at hard-rock sites is consistent with the strain field estimated from geodetic data, which supports stress-induced anisotropy. After the 2011 Tohoku-Oki earthquake, a change in seismicity of the inland earthquake was observed [e.g., Okada et al., 2011]. Yoshida et al. [2012] reported the possibility of coseismic stress change in the overriding plate due to the the coseismic slip of 2011 Tohoki-Oki earthquake at the interplate boundary by using the stress tensor inversion of the focal mechanism [e.g., Asano et al., 2011]. However, in this study, clear coseismic changes in the fast direction were not observed at many hard rock sites, regardless of the static stress change due to the coseismic slip. One possible interpretation is that the static stress change is not sufficient to change the orientation of cracks or the direction of the deviatoric stress.

Although the orientations of the deviatoric stress did not change, the amplitude of the stress field might be affected by the static stress change. We computed the static stress change based on the equation by Okada [1992] and using a slip model by Iinuma et al. [2011]. The horizontal compressional axes and extensional axes of the static stress change are shown in Figure 2.6(b). Roughly speaking, since the direction of the static stress change is the E-W-oriented extension in NE Japan, the anisotropy of the N-S oriented fast direction is expected to be amplified after the Tohoku-Oki earthquake and the anisotropy of the E-W-oriented fast direction is expected to be suppressed. The coseismic increase in the anisotropy at IWTH03 is consistent with the interpretation above because of the N-S-oriented fast direction at IWTH03. However, at FKSH12, the anisotropy appears to increase regardless of E-W fast direction. The static stress change might be complexly intertwined with other related factors, such as large aftershocks along the normal faults with E-W extension near FKSH12 and the dynamic stress changes due to the strong motion. Figure 2.7(d) and 2.7(e) show the counted number of stations on hard-rock sites and soft-rock sites according to angle between the fast direction and the horizontal compressional axis. We divided the sites of stations into the hard-rock sites and the soft-rock sites because we consider sensitivity for the static stress change of the hard-rock sites is higher than that of the soft-rock sites. We followed a definition of the hard-rock sites and the soft-rock sites by Nakata and Snieder [2012a]. The averaged shear velocity between the bottom and the surface estimated from the peak time of CCF of the hard-rock sites is greater than 600 m/s and that of the soft-rock sites is less than 600 m/s. The increase of the anisotropy intensity within a range from 0° to 45° and the intensity decrease within a range from 45° to 90° are consistent with the expected change due to the static stress change. At the hard-rock sites, 64% of stations fit the expected intensity change, which might mean an existence of correlation between the static stress change and the anisotropy intensity change. In contrast, at the soft-rock sites, only 45% of stations fit the expected intensity change. The strong motion may also affects the intensity of polarization anisotropy as a result of change in the number of cracks and in aspect ratio of cracks [Nakata and Snieder, 2012b]. Such micro-scale changes in cracks due to the strong motion and the static stress change result in the macro-scale changes in seismic velocity and polarization anisotropy.

Interferometric analysis of vertical array data has the potential for monitoring not only velocity but also polarization anisotropy. Although we cannot directly observe the temporal change in structure in the seismogenic layer using this method, information on the near-surface velocity change and the near-surface anisotropy change is important in order to validate temporal variations at deeper regions inferred from ambient noise analysis [Brenguier et al., 2008] and repeating earthquake data [Rubinstein et al., 2007].

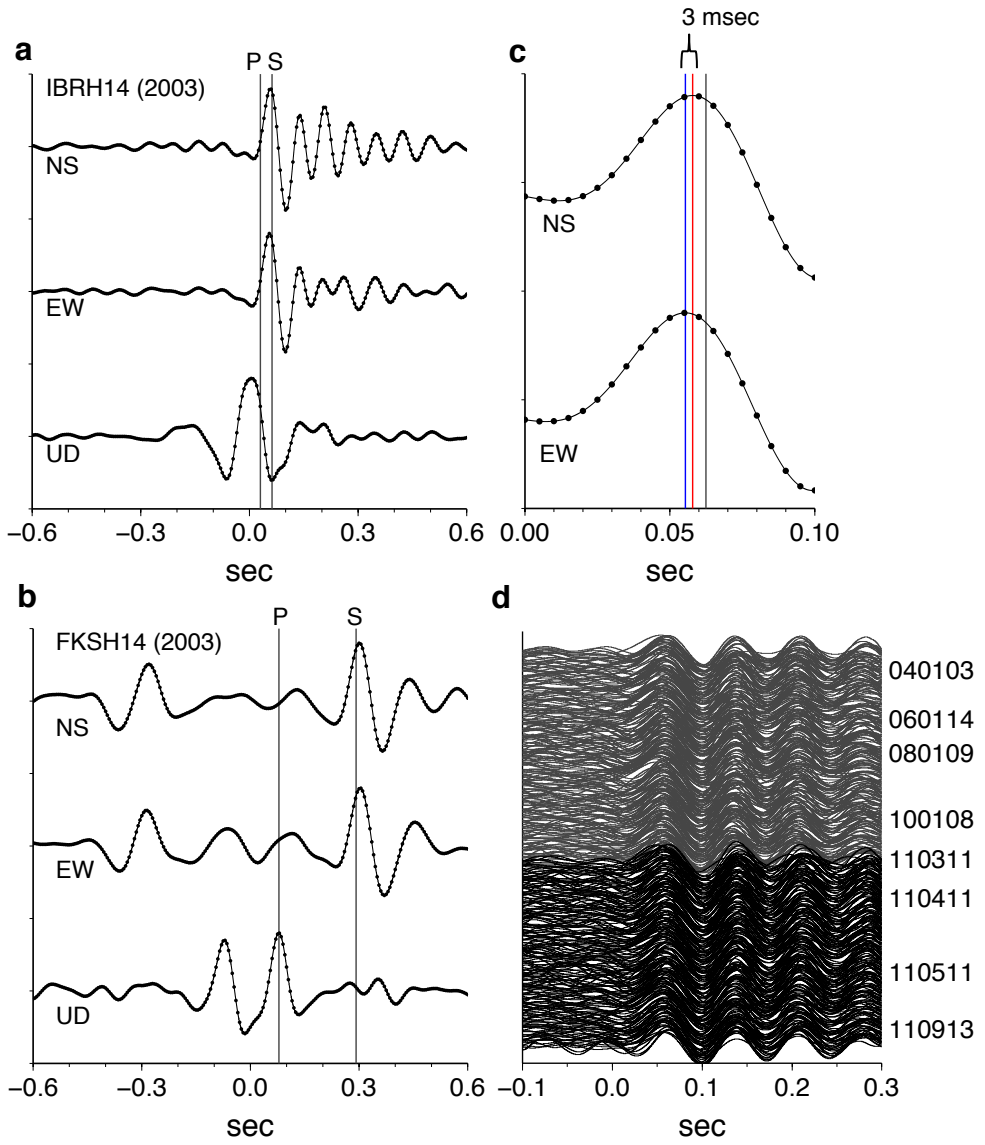

Figure 2.1. Cross-correlation functions for the N-S and E-W polarization direction and for the vertical direction at (a) IBRH14 and (b) FKSH14. The CCFs are averaged over all events in 2003. Data points (black dots) are interpolated by Fourier series (thin lines). The gray vertical lines indicate the theoretical travel times of P and S wave between the bottom and the surface based on logging data. (c) Enlargement of Figure 2.1a. The red and blue lines indicate the peak time of the CCFs for the N-S and E-W directions. The time difference between the two CCFs is 3 ms. (d) Individual CCFs for the N-S direction at IBRH14 arranged by occurrence times of used events. The gray waveforms are CCFs before the Tohoku-Oki earthquake and the blacks are CCFs after the earthquake.

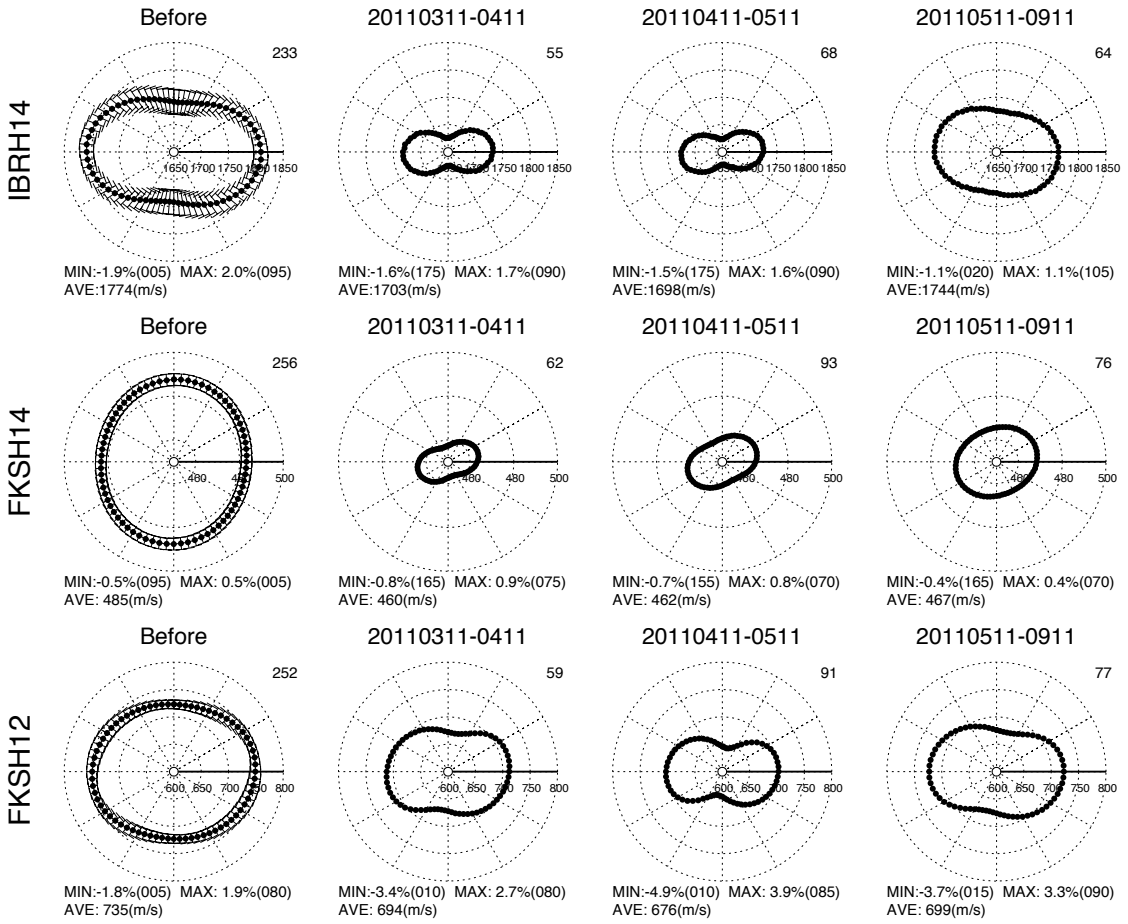

Figure 2.2. Shear velocity as a function of the polarization direction at IBRH14, FKSH14, and FKSH12. The shear velocities of every year from 2000 to 2010 are estimated from yearly averaged CCFs. In 2011, we estimated the shear velocities of four time periods from 1 January to 11 March, from 11 March to 11 April, from 11 April to 11 May, and from 11 May to 11 September. The shear velocities of all time periods before 11 March 2011 are averaged as the shear velocity before the 2011 Tohoku-Oki earthquake. The error bars show the standard deviations of shear velocities for each polarization direction. The minimum and maximum velocities with respect to the azimuthal average are shown below each plot with these directions clockwise from the north. The number of stacked events is shown at the top right of each plot.

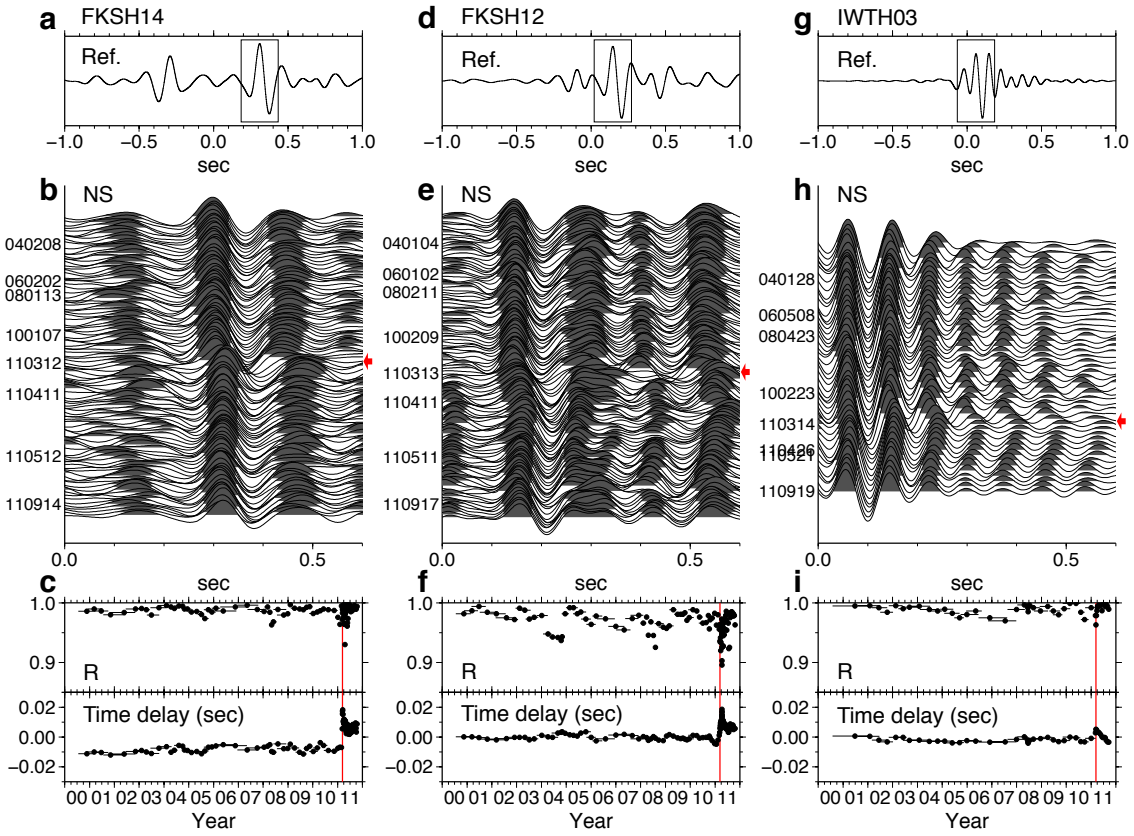

Figure 2.3 (a), (d), and (g) Reference CCFs at FKSH14, FKSH12 and IWTH03. (b), (e), and (h) CCFs for the N-S direction averaged over 10 events, which are arranged by the average occurrence time. Red arrows indicate the occurrence time of the Tohoku-Oki earthquake. (c), (f), and (i) Temporal variations of cross-correlation coefficient, R, and travel time delay between the reference CCFs and the moving averaged CCFs for the N-S direction within the time window indicated in (a), (d), and (g).

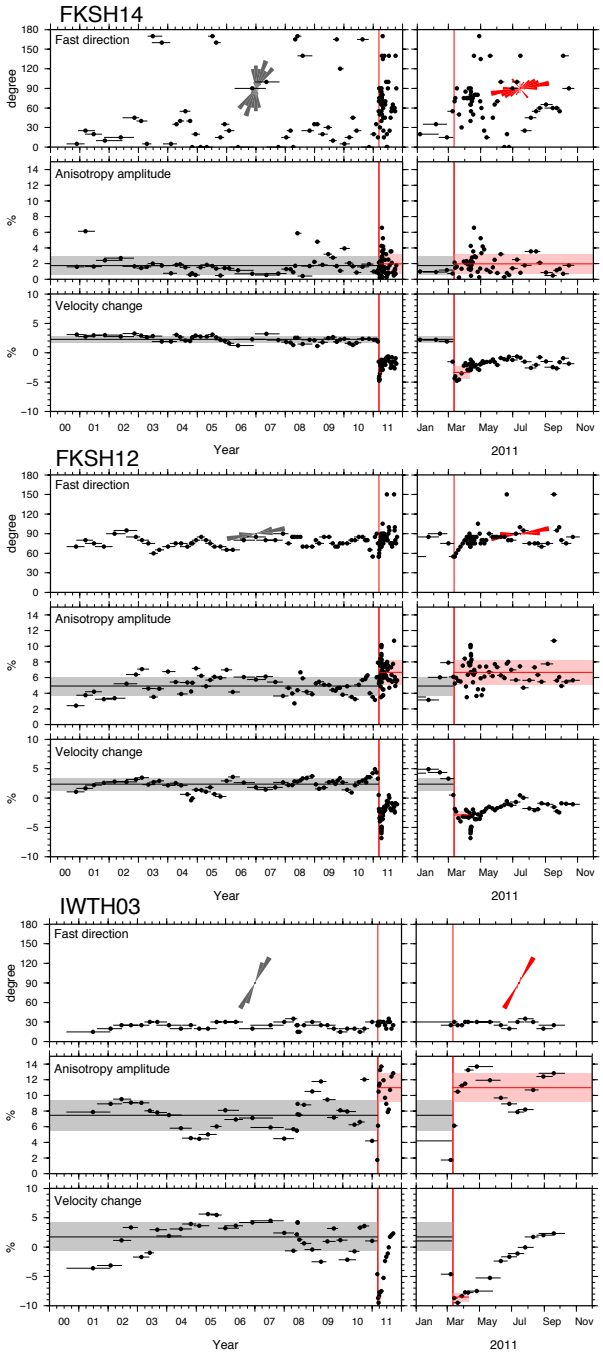

Figure 2.4. Temporal variation of polarization anisotropy and average velocity at FKSH14, FKSH12, and IWTH03. The figures on the right are enlargements of the figures for 2011. The red vertical lines indicate the time at which the 2011 Tohoku-Oki earthquake occurred. The gray and red sectors represent rose diagrams of the fast directions before and after the earthquake, respectively. The gray and red horizontal lines and shadows represent the averages and standard deviations, respectively, during the corresponding time periods.

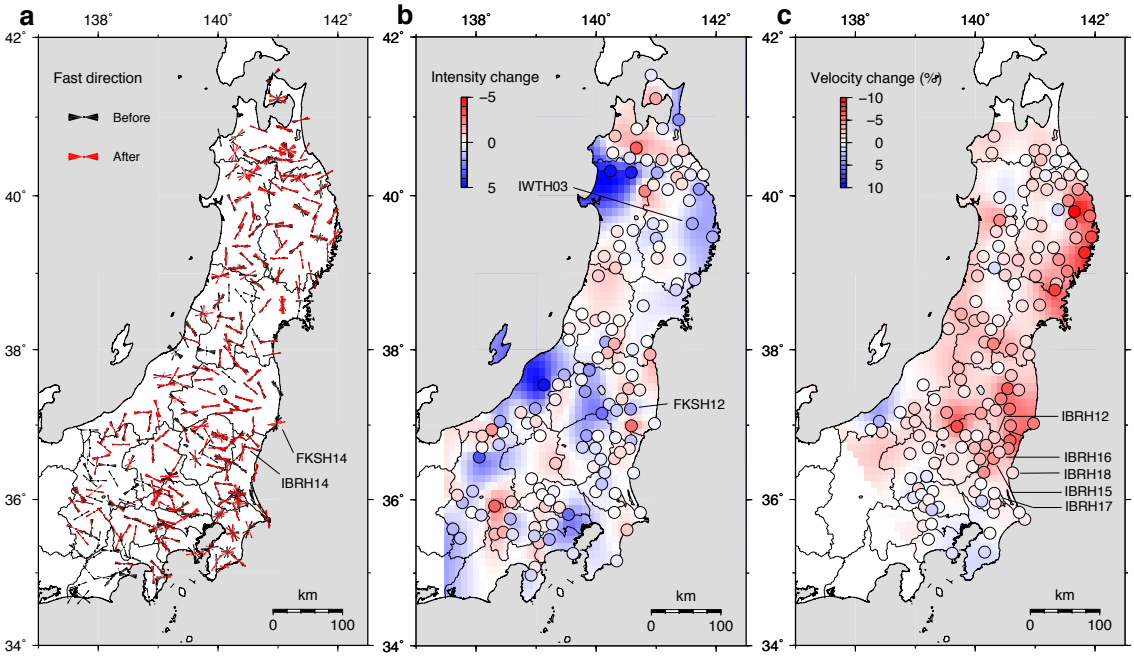

Figure 2.5. Spatial distributions of the fast directions, the intensity change, and the velocity change. (a) The fast directions are measured every 10º. The red and black sectors are the fast directions before and after the Tohoku-Oki earthquake, respectively. The radii of the rose diagrams represent the normalized maximum count. (b) The intensity change is defined as the difference between the average intensities before and after the earthquake. We plotted only data for which the error is smaller than 2.5 points. (c) Relative velocity change, dv/v, before and after the Tohoku-Oki earthquake. Stations that have more than 10 events from 11 March to 11 April 2011 are indicated on the map (Figure 2.5(c)).

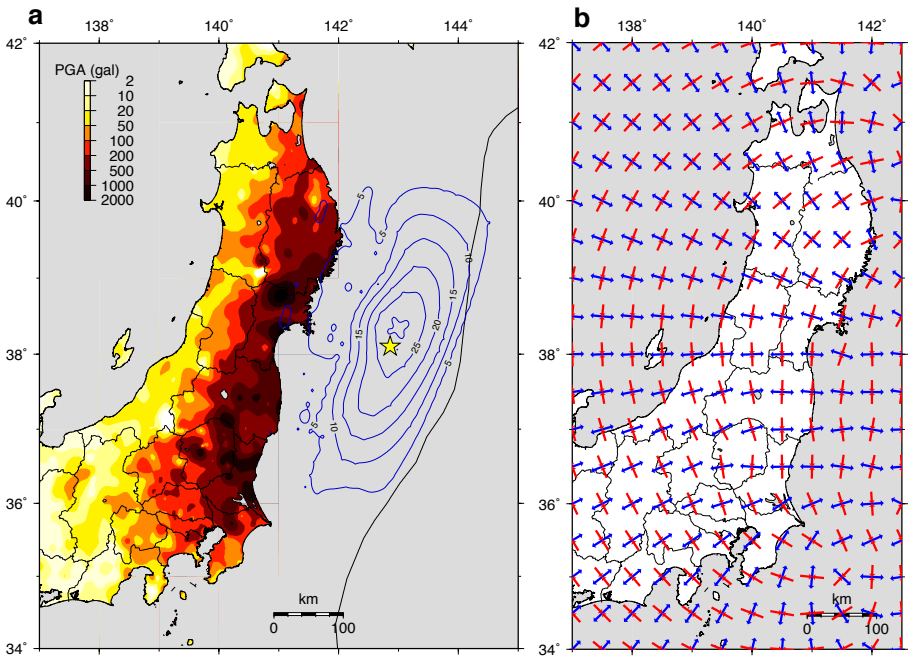

Figure 2.6. (a) Map of the coseismic slip distribution by Iinuma et al. [2011] (blue contours) and PGA observed by the surface sensors of KiK-net and K-NET. Yellow star is the epicenter of the Tohoku-Oki earthquake. (b) Horizontal compressional axes and extensional axes of the static stress change computed using the slip model by Iinuma et al. [2011]. Red and blue arrows represent the compressional and extensional axes, respectively.

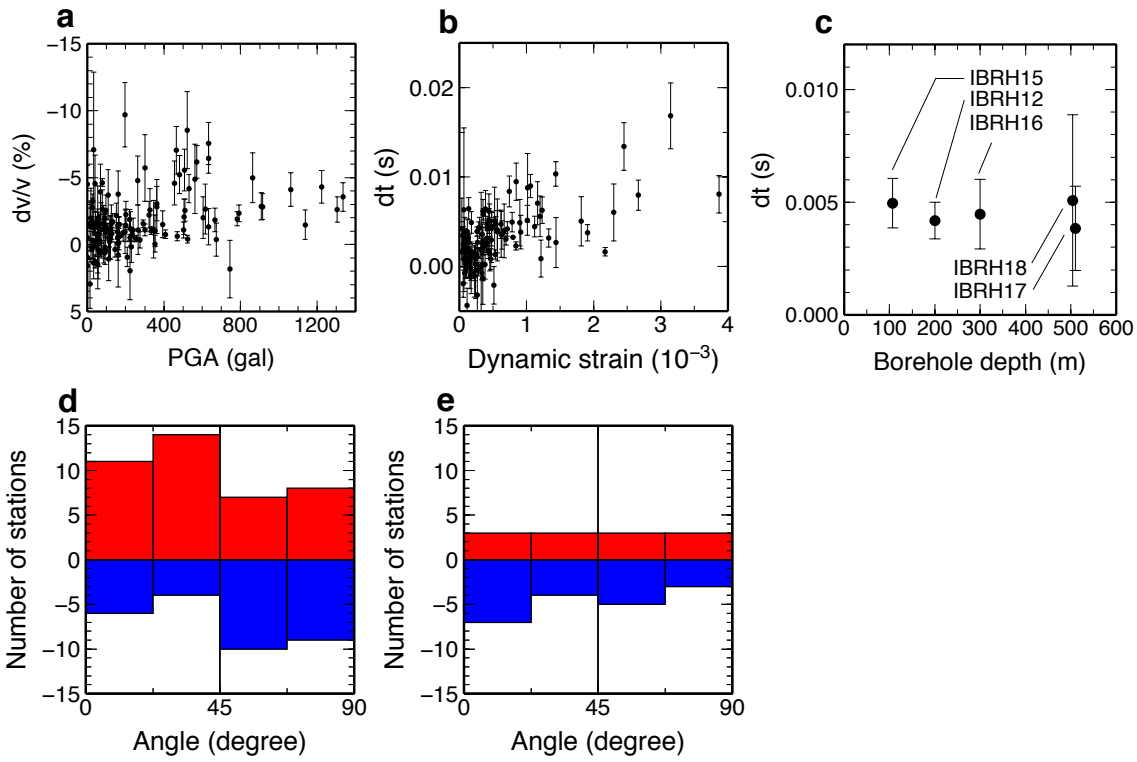

Figure 2.7. (a) Relationship between PGA and relative velocity change, dv/v. The PGA is the maximum amplitude of the three-component vector. The velocity change and the errors are computed from the average and the standard deviations of the relative velocity changes during the periods before and after the earthquake, which are shown in Figure 2.4. (b) Relationship between the maximum of the dynamic strain change and the travel time shift, dt. (c) The travel time shifts at five stations shown in Figure 2.5(c) according to the depth of the boreholes. (d) Counted number of stations on hard-rock sites according to angle between the fast direction and the horizontal compressional axis of the static stress change. Blue bars mean the number of the stations at which anisotropy intensity increase and red bars means the number of the stations at which anisotropy intensity decrease. (e) Similar plots as Figure 2.7(d), but for soft-rock sites.

3. Monitoring seismic velocity structure before and after the 2011 M9.0 Tohoku-Oki earthquake using array observation of ambient noise

Ryota Takagi,[1] Tomomi Okada,[1] Toshio Kono,[1] and Akira Hasegawa[1]

[1]Research Center for Prediction of Earthquakes and Volcanic Eruptions, Graduate School of Science, Tohoku University, Sendai, Japan.

Summary

We detect a temporal velocity change before and after the 2011 Tohoku-Oki earthquake by analyzing ambient noise record observed at a seismic array in Tono, northeast Japan. We use vertical-component records of nine stations during three years from 2010 to 2012 and extract the fundamental-mode Rayleigh wave by computing cross-correlation functions. By fitting the theoretical cross-spectra to the observed cross-spectra at each frequency, we estimated the dispersion curve of the phase velocity of Rayleigh wave within the array. For the fitting, we treat the theoretical cross-spectra for anisotropic wave incidence by expanding the azimuthal noise source distribution by a Fourier series, which allows us to estimate the phase velocity and the noise source distribution simultaneously. Without the modeling of the noise source distribution, the phase velocity shows a large annual variation at a low frequency of 0.4 Hz. The large variation might be an apparent velocity change due to the temporal change in noise source and is suppressed by the simultaneous estimation with the noise source distribution. Clear offsets of phase velocity are observed at the time of the Tohoku-Oki earthquake. The phase velocity suddenly drops after the earthquake, and the offset remains after 21 months. The coseismic decrease of phase velocity shows frequency dependence. From 0.3 to 1.1 Hz, the magnitude of the phase velocity reduction linearly increases from 0.1% to 0.5%, which suggests a near-surface velocity reduction consistent with previous studies. However, in higher frequencies from 1.2 Hz, frequency dependence is not so simple, and the reason is not clarified in the present study. The present study shows the temporal change in Rayleigh wave phase velocity in a wide frequency range of 0.3-1.9 Hz with a better frequency resolution of about 0.2 Hz as compared to previous studies by applying the frequency domain SPAC method to array observation.

3.1. Introduction

Owing to the development of seismic interferometry, ambient noise and coda wave have become powerful tools to monitor subsurface structure [e.g., Brenguier et al. 2008]. Applying seismic interferometry to ambient noise and/or earthquake record, previous studies observed seismic velocity changes after large earthquakes in various regions [e.g., Brenguier et al. 2008; Wegler et al., 2009; Takagi et al., 2012; Hobiger et al., 2012]. After the M9.0 Tohoku-Oki earthquake on 11 March 2011, Nakata and Snieder [2011], Takagi and Okada [2012], and Sawazaki and Snieder [2013] applied seismic interferometry to KiK-net vertical array data and detected 5-10% shear velocity decreases within a few hundred meters. Minato et al. [2012] detected seismic velocity changes up to 1.5% using auto-correlation of ambient noise. Tonegawa et al. [2013] also detected a coseismic velocity reduction by auto-correlating ambient seismic noise recorded on ocean bottom seismometers that is located 100-400 km east of the Japan Trench.

These studies and most of other previous studies on seismic velocity change have detected coseismic velocity changes within limited frequency ranges and with limited frequency resolutions. However, in order to understand the velocity changes in more detail such as the depth extent of the velocity change, frequency dependence of the velocity change is informative because the phase velocity of surface wave at different frequency has different sensitivities in the depth direction.

In addition to coseismic velocity change, some studies have reported seasonal variations in seismic velocity [Meier et al., 2010; Hobiger et al., 2012]. The possible mechanisms of the seasonal variation are thermoelastically induced strain variations [Meier et al., 2010] and water-level variation related to precipitation [Sens-Schönfelder and Wegler, 2006; Nakata and Snieder, 2012a]. However, the ambient noise source also exhibits seasonal variations. Since the subsurface monitoring relies on the stability of ambient noise wavefield, the change in noise source distribution causes a bias for measurement of seismic velocity change [Weaver et al., 2009; Froment et al., 2010; Hadziioannou et al., 2011].

In the present study, we deal with the two issues: the frequency dependence of seismic velocity change and the effect of noise source distribution. In order to address the issues, we take advantage of array observation that allows us to measure the phase velocity of Rayleigh wave in frequency domain and to estimate the noise source distribution simultaneously.

3.2. Data and Cross-Correlation Function

We analyzed ambient noise record observed at Tono array that is operated by Tohoku University. Figure 3.1 shows a map of Tono array. The center of the array is 182 km away from the epicenter of the M9.0 Tohoku-Oki earthquake (11 March 2011). Tono array consists of 10 high sensitivity broadband sensors (STS-1 or STS-2). The minimum and maximum separations of the stations are 2.4 km and 18 km,

respectively. The sampling frequency is 100 Hz. In the present study, we used vertical-component record during three years from 2010 to 2012.

We compute daily cross-correlation functions (CCFs) for all possible pairs of stations. First, we divided one-day-long records into 60-s-long records with an overlap of 30 s. Then, after correcting the instrument response and discarding earthquake as described below, we computed the normalized cross spectra for all segments and then averaged them as follows:

$$\Phi_{\alpha}^{obs}(f) = \left\langle \frac{F_i^*}{|F_i|} \cdot \frac{F_j}{|F_j|} \right\rangle, \tag{3.1}$$

where Φ_{α}^{obs} is the daily averaged cross spectra of α th station pair between *i*th and *j*th stations, and F_i and F_j are the Fourier spectra at *i*th and *j*th stations, respectively. Here, * denotes complex conjugate and $\langle\ \rangle$ means the ensemble average over all segments. Applying the inverse Fourier transform to the cross spectra of equation (3.1), we obtained the daily cross-correlation functions.

A huge number of small earthquakes occurred after the Tohoku-Oki earthquake, which may contaminate ambient noise record especially in high frequency range. In order to ensure the temporal stability of ambient noise field, earthquakes should be removed from continuous record. Figure 3.2(a) shows the 10-minute record on 20 March 2011 at TU.KGL. In low frequencies of 0.25-0.5 Hz and 0.5-1.0 Hz, earthquake signals are below the ambient noise level. On the other hand, in high frequency range of 1-2 Hz, some earthquake contaminate ambient noise signal. That is because the frequency range of 1.0-2.0 Hz is out of the typical frequency band of secondary microseisms and the ambient noise power of 1.0-2.0 Hz is lower than those of low frequencies. Therefore, we detected earthquakes using the frequency band of 1.0-2.0 Hz. In order to remove the contamination by earthquakes, we discarded the segment of which root-mean-square (RMS) amplitude exceeded a threshold. The threshold is set to the three times of the median of the RMS amplitudes in March 2010. We also excluded the segment in which absolute amplitude exceeded the fifth times of the median. Figure 3.2(b) shows the RMS amplitude in March 2010, 2011, and 2012. A lot of segments are discarded just after the Tohoku-Oki earthquake.

Figure 3.3 shows the daily CCFs from 2010 to 2012. CCFs are filtered by Butterworth filter with a bandpass of 1-2 Hz. Clear signals are continuously extracted and stable in time even after the Tohoku-Oki earthquake for the station pair of TU.KGL-TU.KTH. For the station pair of KKJ-SMT, we recognize obvious phase changes that do not coincide with the Tohoku-Oki earthquake. Since the phase changes were found in CCFs including KKJ and SMT, we concluded that the phase changes were caused by instrumental error at KKJ and SMT in the time periods. Therefore, we did not use SMT in all time period and did not use KKJ in the corresponding time period for detecting temporal velocity change.

Figure 3.4 shows the line up of the cross-correlation functions averaged over one year in 2010. We can recognize a clear propagation of the fundamental-mode Rayleigh waves with a propagation velocity of approximately 3 km/s. The asymmetry of the cross-correlation functions suggests the non-isotropic

distribution of noise source. Since we rearranged CCFs so that the positive time lag corresponds to waves propagating east to west in Figure 3.4, most of the ambient noise energy is incident from east.

3.3. Measurement of Phase Velocity and Noise Source Distribution

Aki [1957] proposed a method to measure the dispersion curve of Rayleigh wave from the cross spectra of random and stochastic wavefields, which is known as the spatial autocorrelation (SPAC) method. The SPAC method deals with cross spectra in frequency domain, i.e., the Fourier transform of cross-correlation functions. Assuming the isotropic wave incidence, the theoretical cross spectrum between vertical-component records at two stations is represented by

$$\Phi_\alpha^{cal}(f) = a_0 J_0(kr_\alpha) = a_0 J_0\left(\frac{2\pi f}{c} r_\alpha\right), \tag{3.2}$$

where $\Phi_\alpha^{cal}(f)$ is the theoretical cross spectrum between α th station pair, a_0 is the power spectrum, J_0 is the 0th order Bessel function of the 1st kind, $k = 2\pi f/c$ is the wavenumber of Rayleigh wave, c is the phase velocity of Rayleigh wave, and r_α is the separation distance of α th station pair. By fitting the Bessel function to the observed cross spectra Φ_α^{obs}, we can estimate the dispersion curve of the phase velocity of Rayleigh wave. Figure 3.5 shows the cross spectra against geometry of station pair (separation distance and azimuth) and against separation distance. The real part of the cross spectra show concentric patterns explained by the Bessel function $J_0(kr)$.

In real case, however, the distribution of noise source is generally not isotropic as shown by the asymmetric cross-correlation functions in Figure 3.4. The imaginary part of cross spectra and the variation from the 0th order Bessel function in the real part in Figure 3.5 also reflect the anisotropic wave incidence. The anisotropic noise distribution causes a bias of velocity estimation, which becomes a critical problem for detecting a subtle change in seismic velocity of the order of 0.1% or smaller [Weaver et al., 2009; Froment et al., 2010]. Therefore, for the phase velocity measurement, the anisotropy of noise source distribution should be considered. In the case of anisotropic incidence of ambient noise, Cox [1973] derived the theoretical expression of cross spectrum by expanding the source distribution by a Fourier series as follows:

$$\Phi_\alpha^{cal}(f) = a_0 J_0(kr_\alpha) + 2\sum_{m=1}^{\infty} i^m J_m(kr_\alpha)\left[a_m \cos m\xi_\alpha + b_m \sin m\xi_\alpha\right], \tag{3.3}$$

$$A(\theta) = a_0 + 2\sum_{m=1}^{\infty}\left[a_m \cos m\theta + b_m \sin m\theta\right], \tag{3.4}$$

where i^m is the mth power of the imaginary unit, J_m is the mth order Bessel function of the 1st kind, and ξ_α is the azimuth between α th station pair. $A(\theta)$ is the incident wave power as a function of azimuth θ, representing the noise source distribution. a_m and b_m are the Fourier coefficients. In equation (3.3), the theoretical cross spectra is represented by a superposition of the contributions from the

isotropic term and high order terms. Note that equation (3.3) is identical to equation (3.2) in the isotropic case, $A(\theta) = a_0$.

Harmon et al. [2010] used the same equation as equation (3.3) to estimate noise source distribution. In the present study, using equation (3.3), we determined the phase velocity and the noise source distribution simultaneously by minimizing the following misfit function S between the observed and theoretical cross spectra,

$$S(c, a_0, a_m, b_m; f) = \sum_{\alpha}^{N} \left| \Phi_{\alpha}^{obs}(f) - \Phi_{\alpha}^{cal}(c, a_0, a_m, b_m; f, r_{\alpha}, \xi_{\alpha}) \right|^2 , \tag{3.5}$$

where N is the number of station pair. Here, we used the phase velocity $c = 2\pi f / k$ instead of k as the unknown parameter. For each frequency, we applied a grid search for the phase velocity c and the linear least squares for the Fourier coefficient of noise source a_m and b_m. For each phase velocity grid, we write the observation equation by the following matrix form,

$$\begin{bmatrix} \Phi_1^{obs}(f) \\ \vdots \\ \Phi_N^{obs}(f) \end{bmatrix} = \begin{bmatrix} J_0(kr_1) & \cdots & 2i^M J_M(kr_1)\cos M\xi_1 & 2i^M J_M(kr_1)\sin M\xi_1 \\ \vdots & \ddots & \vdots & \vdots \\ J_0(kr_N) & \cdots & 2i^M J_M(kr_N)\cos M\xi_N & 2i^M J_M(kr_1)\sin M\xi_N \end{bmatrix} \begin{bmatrix} a_0 \\ \vdots \\ a_M \\ b_M \end{bmatrix}, \tag{3.6}$$

where N is the number of station pair, M is the order of Fourier series expansion. The number of model parameter is $2M+1$. We selected $M = 4$ for all frequencies, considering the variation of the misfit with respect to the modeling order M as shown in Figure 3.6(b) and the stability of the phase velocity measurement. The least squares solution is given by

$$\mathbf{m} = \left[\mathbf{G}^T \mathbf{G} \right]^{-1} \mathbf{G}^T \mathbf{d} , \tag{3.7}$$

where $\mathbf{m}$ is the model vector of the Fourier coefficient a_m and b_m, and $\mathbf{d}$ is the data vector of the cross spectra Φ_{α}^{obs}, $\mathbf{G}$ is the forward matrix computed using the separation distance r_{α}, the azimuth ξ_{α}, and the Bessel functions. After that, the grid search for c gives the optimal value of c minimizing equation (3.5). Finally, in order to stabilize the phase velocity measurement, we smoothed the dispersion curve of phase velocity using a 15-frequency-points moving average of 0.18 Hz bandwidth.

Since the phase velocity is estimated by the grid search, we chose the constant chi-square boundaries as the confidence limits of the phase velocity measurement [Press et al., 1986]. The chi-square value is defined for each phase velocity grid as

$$\chi^2(c; f) = \sum_{\alpha}^{N} \frac{\left| \Phi_{\alpha}^{obs}(f) - \Phi_{\alpha}^{cal}(c, a_0, a_m, b_m; f) \right|^2}{\sigma^2} , \tag{3.8}$$

where σ^2 is the unbiased estimation of variance and given by

$$\sigma^2 = \frac{S_{\min}}{2N - (2M+1)} , \tag{3.9}$$

where $S_{\min}$ is the minimized misfit function of equation (3.5) for the optimal value of the phase velocity c. In equation (3.6), the Fourier coefficients a_0, a_m, and b_m are optimized for each phase velocity grid using equation (3.7). The boundaries of χ^2 that satisfy

$$\Delta\chi^2(c;f) = \chi^2(c;f) - \chi^2_{\min} = 1, \tag{3.10}$$

give the 1σ (68.3%) confidence limits of the phase velocity measurement, where $\chi^2_{\min}$ is the minimum value of χ^2 and is equal to $2N-(2M+1)$.

3.4. Annual Average of Phase Velocity and Noise Source Distribution

First, we estimated the annual average of phase velocity and noise source distribution from the averaged cross spectra in 2010. Figure 3.6(a) depicts the variance reduction of the fitting with respect to frequency and phase velocity, showing the dispersion curve of Rayleigh wave. The variance reduction $VR(f)$ is defined as

$$VR(f) = 1 - S(c,a_0,a_m,b_m;f) \Big/ \sum_{\alpha}^{N} \left|\Phi_{\alpha}^{obs}(f)\right|^2, \tag{3.11}$$

where a_0, a_m, and b_m are optimized by equation (3.7) to minimize S at a given phase velocity. The 4th order modeling ($M=4$) shows better variance reductions than the 0th order modeling ($M=0$), which suggests the effectiveness of the simultaneous modeling. The estimated phase velocity is consistent with the phase velocity of fundamental-mode Rayleigh wave calculated using the velocity structure by Nishida et al. [2008a]. The small difference may be from the difference in frequency range between the present study and Nishida et al. [2008a] who estimated the velocity structure from dispersion curves of Rayleigh and Love waves in a frequency range of 0.05-0.2 Hz.

The simultaneous measurement also gives a frequency dependence of noise source distribution. Figure 3.6(c) shows the noise source distribution in 2010. The characteristics of the noise source distribution changes around 0.6 Hz. Below 0.6 Hz, the maximum peak is in 150-180º, and the second peak is about 45º. Since the back azimuth is measured clockwise from the north, the maximum and second peaks correspond to incident waves from SSE-S and NE, respectively. The noise source distribution is consistent with the frequency-wavenumber spectra estimated from the beamforming method [Rost and Thomas, 2002]. Above 0.6 Hz, the maximum peak is in 90-120º. The noise source distribution dominates in east, suggesting that Rayleigh waves are generated in the Pacific Ocean.

3.5. Temporal Change in Phase Velocity and Noise Source Distribution

We measured the temporal variation of phase velocity by estimating the phase velocity from 60-day averaged cross spectra every 30 days. We examined the 0th order (isotropic noise source) and the 4th order Fourier expansion to fit the theoretical cross spectra (equation (3.3)) to the observed cross spectra (equation (3.1)). Figure 3.7 shows the temporal variations in phase velocity at several frequencies. For all

frequencies, we can recognize clear offsets of phase velocity at the time of the Tohoku-Oki earthquake on 11 March 2011. The phase velocity suddenly dropped after the earthquake and the offset remained after 21 months.

In addition to the coseismic offset, annual variations in phase velocity are observed. Without the modeling of the noise source distribution ($M = 0$), the estimated phase velocity shows a large annual variation at the low frequency of 0.4 Hz. Figure 3.8 shows the temporal variations in noise source distribution estimated from the 4th order modeling ($M = 4$). At 0.4 Hz, the noise source distribution exhibits a clear seasonal variation: the maximum peak is in SSE-S in summer and in NE in winter. The temporal changes in the noise source distribution cause a bias of the phase velocity measurement unless the noise source distribution is taken into account for the phase velocity measurement. Therefore, the large annual variation of the 0th order modeling at 0.4 Hz is probably an apparent change due to the change in noise source distribution and is suppressed by the simultaneous modeling of the phase velocity and the noise source distribution with the 4th order Fourier series. At the other frequencies, the difference between the 0th and 4th order modeling is less remarkable. There may be two reasons. One is the stability of the noise source distribution at high frequencies as compared to 0.4 Hz. In contrast to the clear seasonal change in the maximum peak at 0.4 Hz, the peak direction depends little on time at high frequencies of 0.8, 1.2, and 1.6 Hz as shown in Figure 3.8. The other is that the use of all data in various azimuths plays a roll of azimuthal average somewhat. Therefore, the 0th order modeling even gives a good estimation of the phase velocity.

In order to estimate the frequency dependence of the cosesimic velocity change, we fitted the following curve $f(t)$ to the temporal variation of the phase velocity,

$$f(t) = C + DH(t - t_0) + A\sin\left(2\pi(t - \alpha)/365\right), \tag{3.12}$$

where C is the phase velocity before the earthquake and D is the coseismic drop of phase velocity, H is the Heaviside step function, t_0 is the occurrence time of the Tohoku-Oki earthquake, and A and α represent the amplitude and phase of the annual variation, respectively. Figure 3.9 depicts the frequency dependence of the phase velocity change estimated from the temporal variation by the 4th order fitting. The magnitude of the coseismic velocity decrease shows clear frequency dependence. From 0.3 to 1.1 Hz, the magnitude of the phase velocity decrease linearly increases from 0.1% to 0.5% as frequency increases. However, in the higher frequency range from 1.2 Hz, the frequency dependence is more complicated. The phase velocity decrease at 1.5 Hz is 0.3% and smaller than that at 1.0 Hz.

3.6. Discussion

First, we discuss the advantage of array observations for monitoring subsurface structure. We detected the temporal variation of the phase velocity of Rayleigh wave in the wide frequency range of 0.3-1.9 Hz with the high frequency resolution of about 0.18 Hz. The wide band and the high frequency

resolution are the advantages of the present study as compared to previous studies. The advantages are the result of the frequency domain measurement based on the SPAC method for the array observation. Besides, array observations also enable us to investigate noise source distribution using the azimuthal coverage of array observations. We show that the simultaneous measurement of phase velocity and noise source distribution has a potential to suppress the apparent velocity change due to change in noise source distribution.

Next, we discuss the frequency dependence of the coseismic velocity change. The previous studies using the KiK-net vertical array have revealed the shear velocity decrease by 5-10% within near-surface layer up to a few hundred meters [Nakata and Snieder, 2011; Takagi and Okada, 2012; Sawazaki and Snieder, 2013]. Figure 3.10 shows the sensitivity kernels of the phase velocity of Rayleigh wave calculated by the method of Saito [1988]. The structure model by Nishida et al. [2008a] at the center of Tono array is used to calculate the sensitivity kernels. Figure 3.10 indicates that higher frequency has more sensitivity to structures at shallower depth. Therefore, the larger decreases of phase velocity at higher frequencies in 0.3-1.1 Hz are consistent with the near-surface shear velocity reduction estimated from KiK-net vertical array. For the 2008 Iwate-Miyagi Nairiku earthquake, Takagi et al. [2012] has also discussed the effect of near-surface velocity change by integrating the ambient noise method and the vertical array method, concluding that the 5% shear velocity change in a few hundred meters from surface almost explain the 0.5% phase velocity change of Rayleigh wave estimated by the noise correlation method. The frequency dependence of phase velocity change allows us to estimate the depth extent of shear velocity change [Hobiger et al., 2012]. However, the characteristics of the phase velocity change above 1.2 Hz cannot be explained by the near-surface shear velocity reduction. In order to explain the characteristics, a more complex vertical distribution of velocity change is necessary. Consequently, this is still a question to be solved.

Figure 3.10 also shows that Rayleigh wave has considerable sensitivities to compressional velocity and density in shallow depth. Therefore, only from Rayleigh wave, it is difficult to resolve both of shear and compressional velocity changes. However, since Love wave do not have sensitivity to compressional velocity, the investigation of Love wave velocity change may be useful to reveal the shear and compressional velocity changes. Therefore, three-component analysis is a key to extract Love wave and may help to answer to the question about the strange behavior of the phase velocity change in high frequencies.

3.7. Conclusions

We detected a temporal change in phase velocity of Rayleigh wave in a wide frequency range of 0.3-1.9 Hz with a high frequency resolution of 0.18 Hz by analyzing ambient noise record observed at Tono array. Clear decreases in phase velocity of 0.1-0.5% after the Tohoku-Oki earthquake are observed

at all frequencies. In the low frequency range of 0.3-1.1 Hz, the magnitude of the phase velocity decrease is simply proportional to frequency. Since Rayleigh wave at higher frequency has larger sensitivity at shallow depth, the large velocity decrease in high frequency is consistent with the near-surface shear velocity reduction demonstrated by previous studies. However, the high frequency range above 1.2 Hz shows more complicated frequency dependence, which is still a question to be solved. In the present study, we also demonstrated a way to address the apparent velocity change due to temporal change in noise source distribution. Our method is based on the theoretical expression of the cross spectra for anisotropic wave incidence and allow us to estimate the phase velocity and the noise source distribution simultaneously. Using the method, we show the suppression of the apparent seasonal variation due to significant change in noise source distribution at 0.4 Hz. The phase velocity measurement in wide frequency band, with high frequency resolution, and with simultaneous measurement of noise source distribution is the result of array observation. Array observations of ambient noise are useful for monitoring dynamic subsurface structure, not only estimating static subsurface structure.

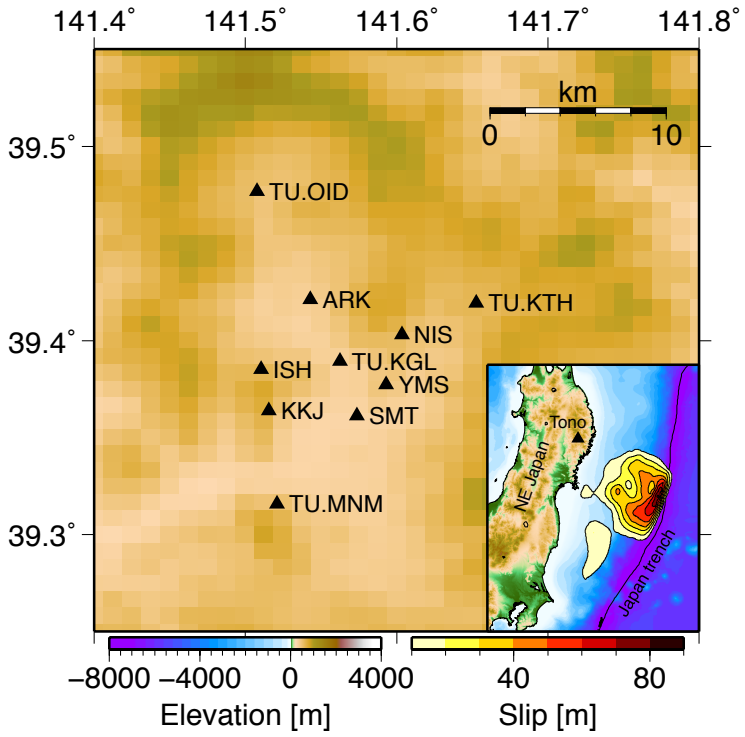

Figure 3.1. Map of Tono array. Tono array consists of 10 broadband seismic stations (black triangles). Contours show the coseismic slip estimated by Iinuma et al. [2012] by intervals of 10 m. The minimum of the contour is 10 m.

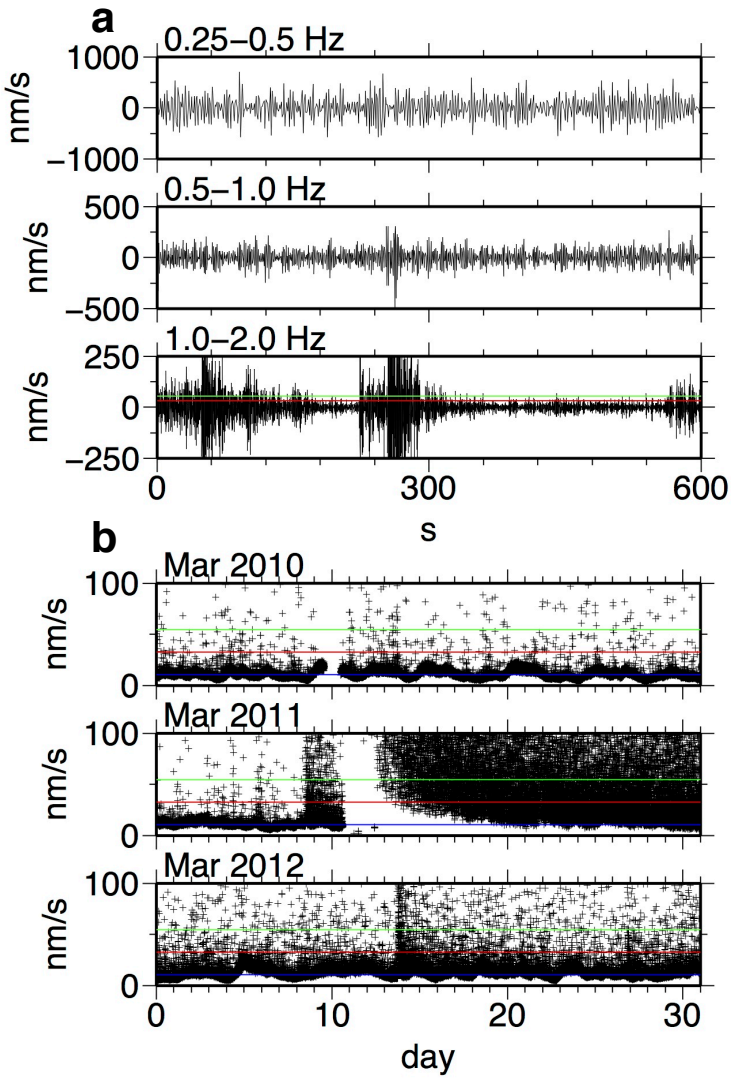

Figure 3.2. (a) Band-pass-filtered vertical-component records of TU.KGL from 00:00:00 to 00:10:00 on 20 March 2011 with the pass bands of 0.25-0.5 Hz (top), 0.5-1.0 Hz (middle), and 1.0-2.0 Hz (bottom). Red and green lines are three times and five times of the median of the RMS amplitude in May 2010 and used as threshold values for discarding earthquakes. (b) RMS amplitude of vertical component of TU.KGL in the frequency range of 1-2 Hz in March 2010 (top), March 2011 (middle) and March 2012 (bottom). Blue line is the median of the RMS amplitude in March 2010. Red and green lines are the same with (a).

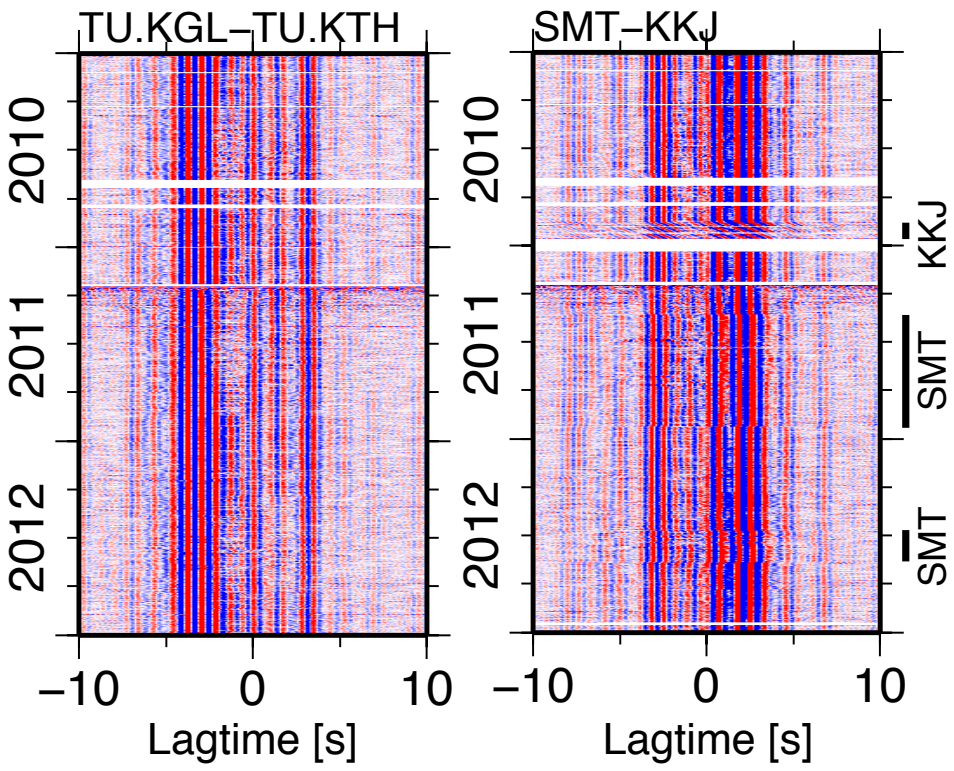

Figure 3.3. Daily CCFs for the station pairs of TU.KGL-TU.KTH and SMT-KKJ from 2010 to 2012. Black lines specify the time periods of distinct phase change due to instrumental problem of KKJ and SMT.

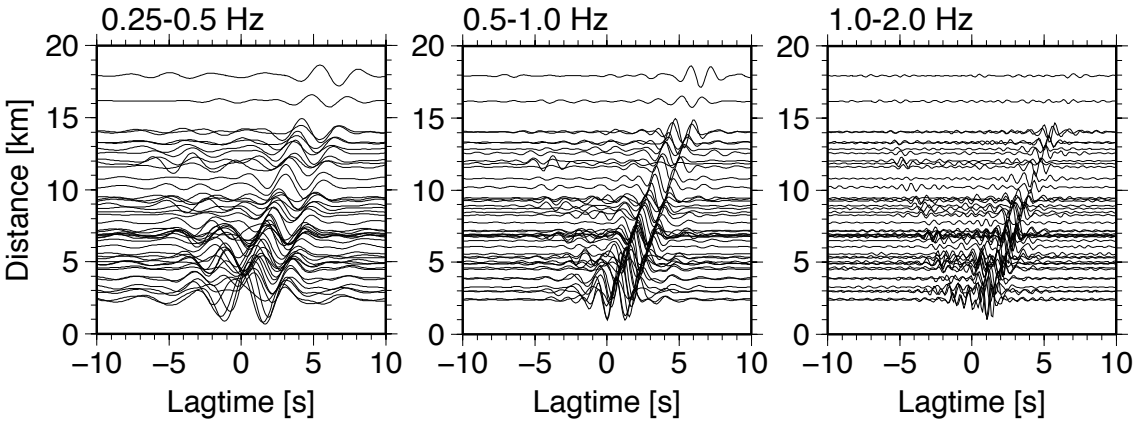

Figure 3.4. Lineup of the averaged CCFs in 2010 in three frequency ranges of 0.25-0.5 Hz, 0.5-1.0 Hz and 1.0-2.0 Hz. Positive lag corresponds to wave propagating from east to west.

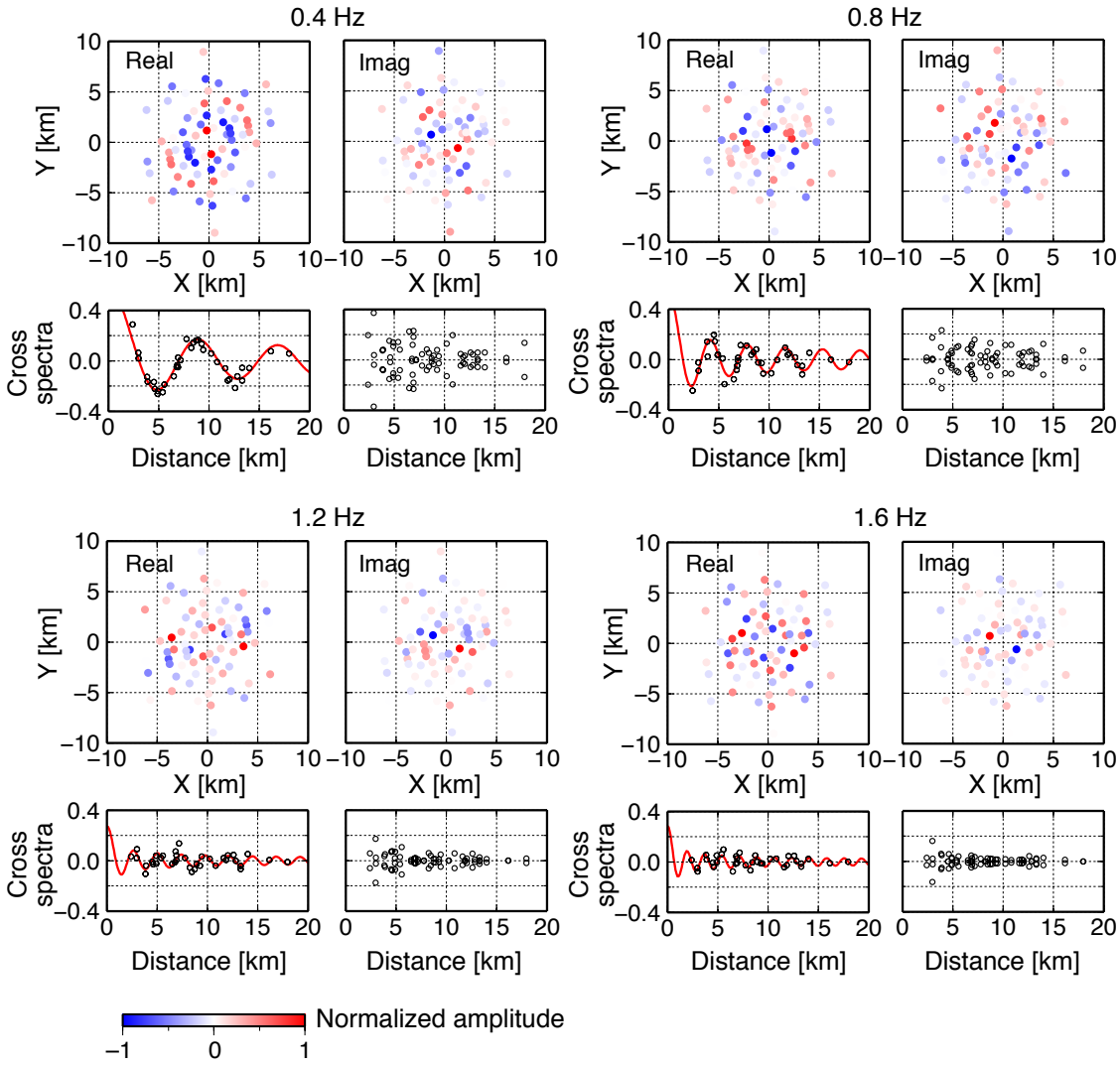

Figure 3.5. Real part (left) and imaginary part (right) of cross spectra with respect to geometry of station pair (upper panels) and separation distance (lower panels) for four frequencies of 0.4, 0.8, 1.2, and 1.6 Hz. The horizontal axis X is EW distance, and the vertical axis Y is NS distance. Red and blue dots show the normalized amplitude of cross spectra. Red lines show the best fit of the Bessel function $J_0(kr)$ estimated by the 0th order modeling.

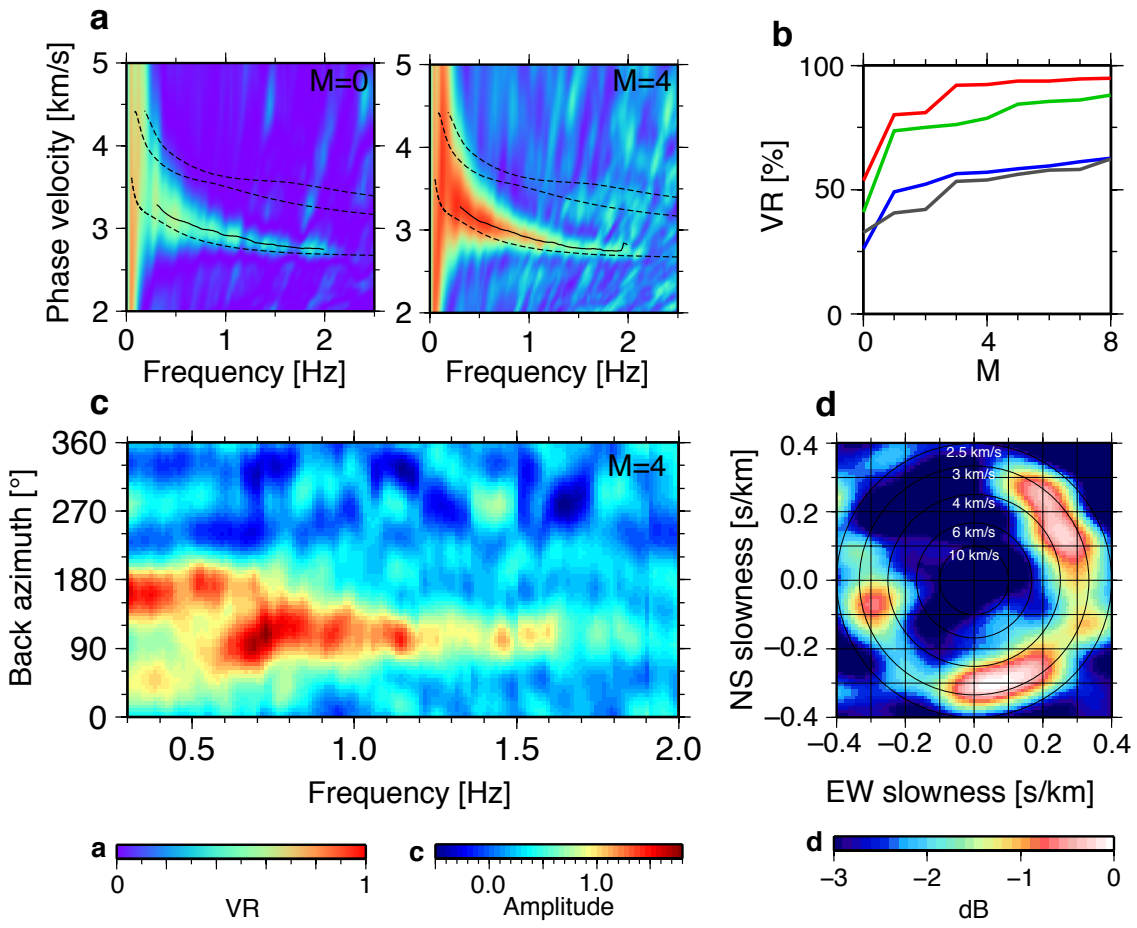

Figure 3.6. (a) Variance reductions of the least square fit with the 0th and 4th order Fourier series. Dashed lines are Rayleigh wave phase velocities of fundamental mode (slowest) and first (intermediate) and second (fastest) overtones for the velocity structure by Nishida et al. [2008a]. (b) Variance reductions with respect to the model order at four frequencies of 0.4 Hz (red), 0.8 Hz (green), 1.2 Hz (blue), and 1.6 Hz (gray). (c) Frequency dependence of the noise source distribution estimated by the 4th order modeling. (d) Frequency-wavenumber (FK) spectra at 0.4 Hz in slowness plane. FK spectra is estimated by the conventional beamforming method.

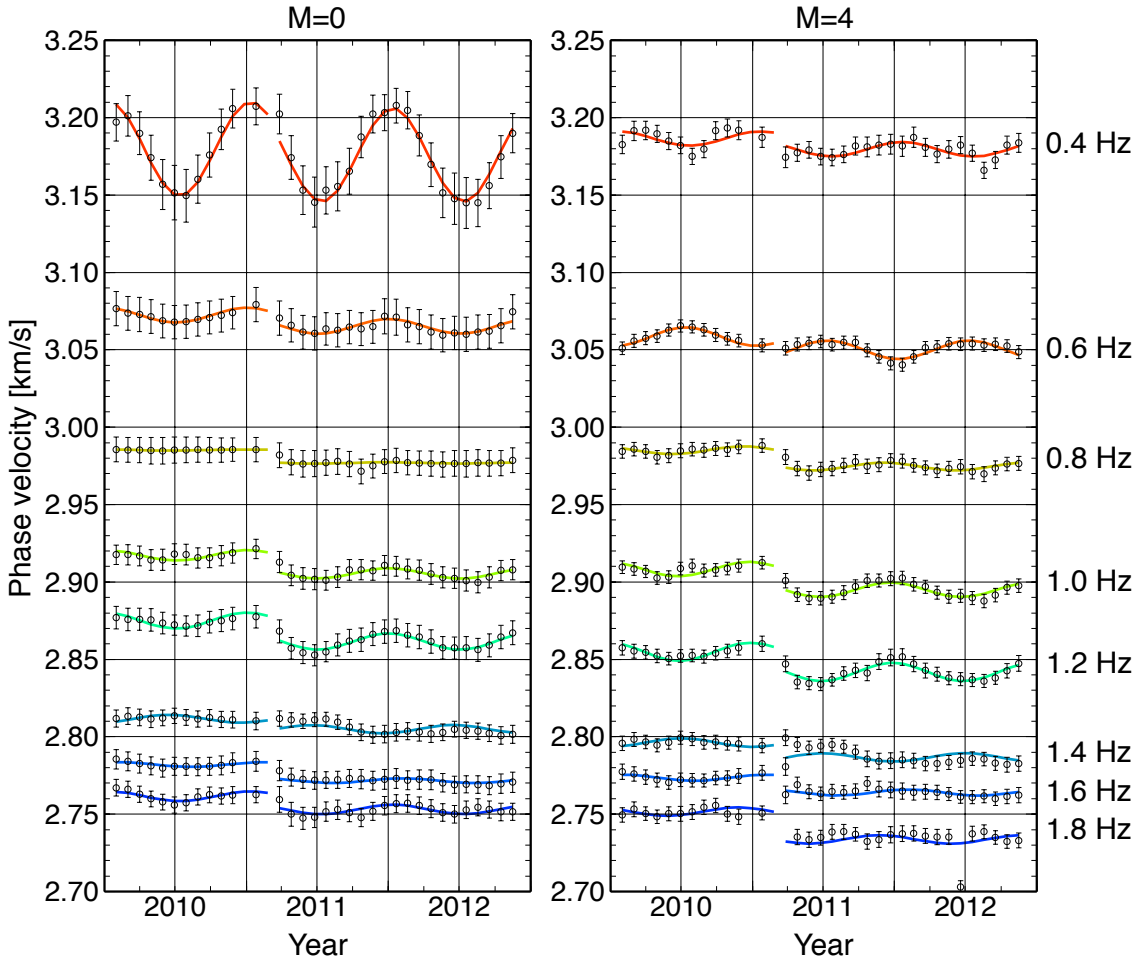

Figure 3.7. Temporal variations in phase velocity of Rayleigh wave for eight frequencies from 0.4 to 1.8 Hz. The left panel is the result of the 0th order modeling and the right panel is the result of the 4th order modeling. Error bars show the 1σ confidence intervals. Color solid lines are the best fitting curve representing a coseismic offset and an annual variation.

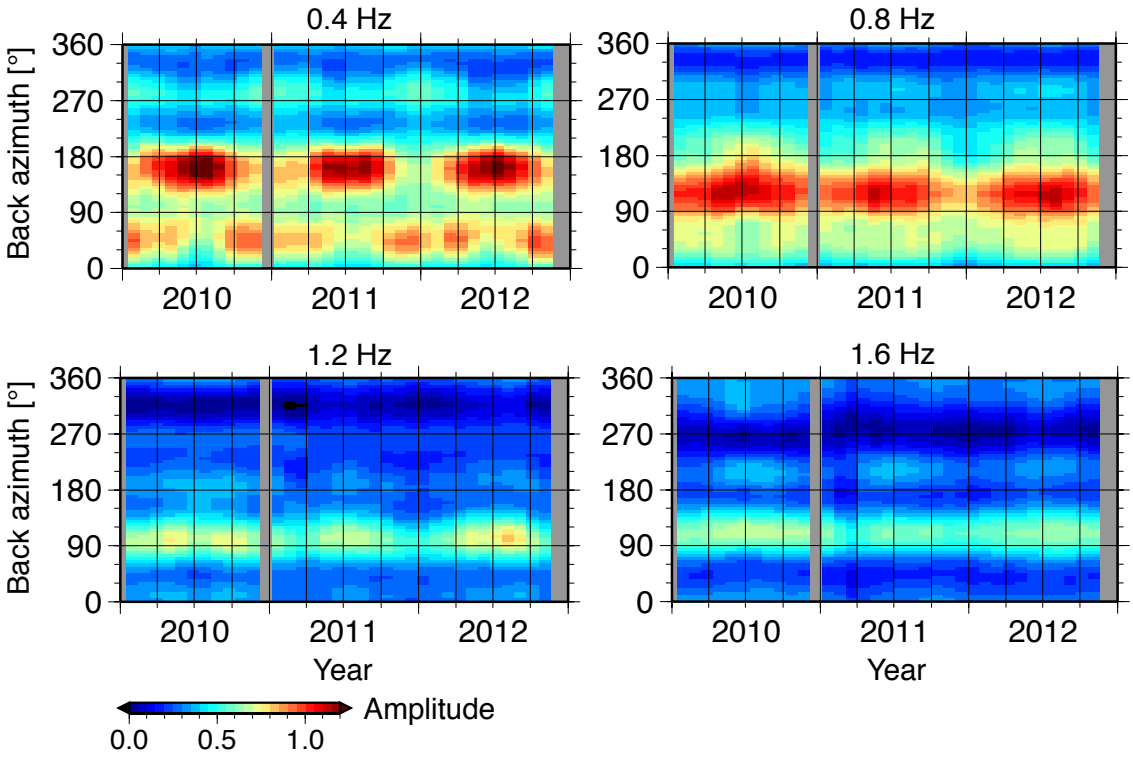

Figure 3.8. Temporal change in noise source distribution at four frequencies of 0.4, 0.8, 1.2, and 1.6 Hz. The back azimuth are taken clockwise from the north.

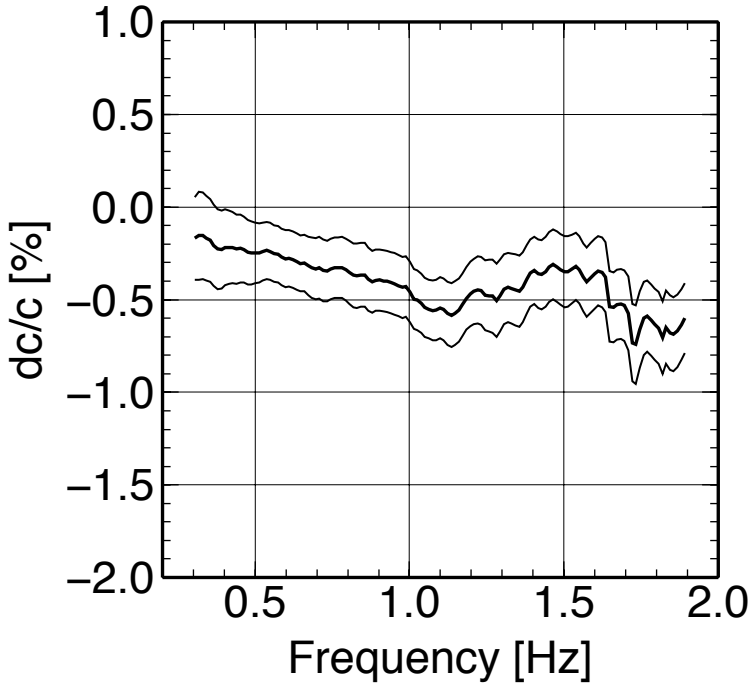

Figure 3.9. Frequency dependence of coseismic phase velocity change of Rayleigh wave. Thick and thin lines indicate the estimated value and its 3σ confidence intervals.

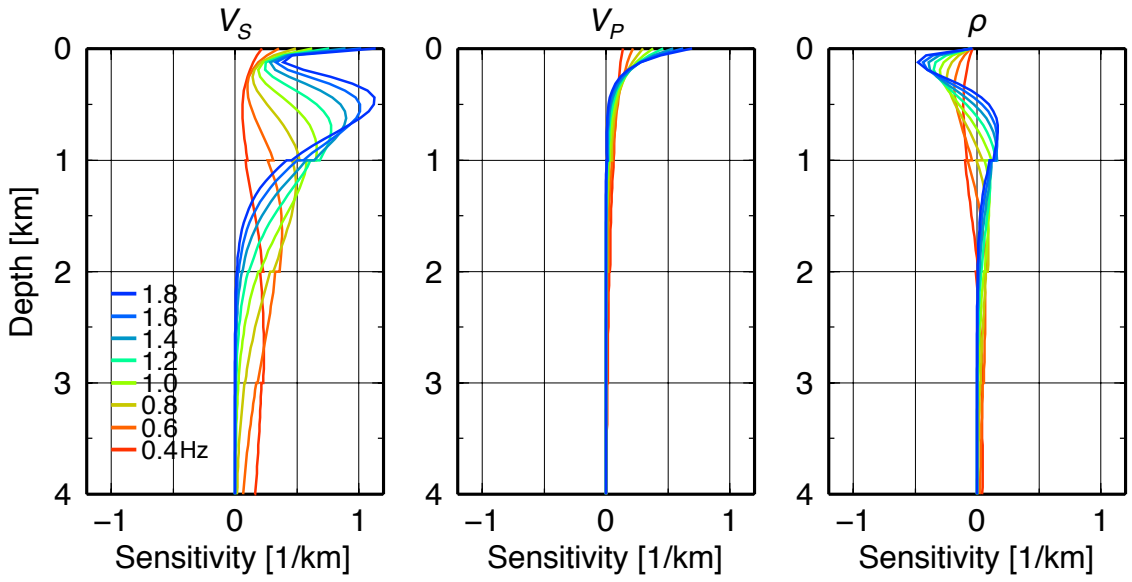

Figure 3.10. Sensitivity kernels of phase velocity of Rayleigh wave with respect to shear velocity (V_S), compressional velocity (V_P), and density (ρ). The sensitivity kernels are calculated by the method of Saito [1988] using the velocity structure of Nishida et al. [2008a].

4. Separating body and Rayleigh waves with cross terms of the cross-correlation tensor of ambient noise

Ryota Takagi,[1] Hisashi Nakahara,[2] Toshio Kono,[1] and Tomomi Okada[1]

[1]Research Center for Prediction of Earthquakes and Volcanic Eruptions, Graduate School of Science, Tohoku University, Sendai, Japan.

[2]Department of Geophysics, Graduate School of Science, Tohoku University, Sendai, Japan.

Summary

We develop a novel method to separate body and Rayleigh waves with the vertical-radial (ZR) and radial-vertical (RZ) components of the cross-correlation tensor of ambient noise. Furthermore, analyzing ambient noise records observed at a seismic array, we validate the method. For the separation, we utilize the difference in polarizations between the rectilinear P and the elliptic Rayleigh waves. Assuming that the two-dimensional surface and three-dimensional body waves are the superposition of random uncorrelated plane waves, we derive two fundamental characteristics of ZR and RZ correlations. One is that, between ZR and RZ correlations, Rayleigh wave contributions have the opposite signs and P waves have the same signs. The other is that, for both ZR and RZ correlations, Rayleigh wave contributions are time-symmetric and P waves are time-antisymmetric for the case of isotropic incidence. Accordingly, we can separate P and Rayleigh waves by just taking summation and difference between ZR and RZ correlations and by just taking time-symmetric and time-antisymmetric components. This method can be performed (1) without any knowledge of velocity structure, (2) using only two stations with three component sensors on a ground surface, (3) even in the case of anisotropic wave incidence, and (4) with the quite simple procedure. We consider that the developed method can make better use of three-component observation of ambient noise for evaluating the cross-correlation tensor accurately, for improving deep velocity structure using both of extracted body and surface waves and, more fundamentally, for understanding the composition of ambient noise.

4.1. Introduction

Seismic interferometry can reconstruct the impulse response including body and surface waves between two stations by cross-correlating random wavefield such as ambient noise and coda wave. Surface waves extracted from ambient noise provide sufficient data for travel-time tomography [e.g., Sabra et al., 2005; Shapiro et al., 2005]. Such ambient noise surface wave tomography has become a common tool and has been widely used to investigate subsurface structure. In this method, vertical component of Rayleigh wave extracted from vertical-vertical (ZZ) correlation is most commonly used because of the simplicity of analysis and/or observation.

Body wave propagation has also been detected in cross-correlation functions of ambient noise [e.g., Roux et al., 2005] or coda wave [Tonegawa et al., 2009]. Roux et al. [2005] extracted direct P waves in 10 km scale. Zhan et al. [2010] and Poli et al. [2012] showed Moho reflection phases in noise correlations in 100–500 km scale. Nishida [2013b], Boué et al. [2013], and Lin et al. [2013] also extracted body wave propagations on global scale. Since body wave can propagate downwards, body wave exploration may offer higher resolution for deep velocity structure and its discontinuities at depth than surface wave exploration.

However, the body wave retrieval is still scarce as compared with the surface wave retrieval from ambient noise. One reason of the difficulty is the dominance of surface wave in ambient noise at frequencies lower than 1 Hz. In particular to noise correlations in short separation distance, body wave arrivals may be masked by the large amplitude of surface wave because the body wave is not separated from surface wave arrivals. On the other hand, in terms of surface wave study, if ambient noise contains body waves with comparable amplitude to surface waves, surface wave portion may be contaminated by the body wave arrivals. The body wave contamination may be critical for the spatial auto-correlation (SPAC) method [Aki, 1957] because the SPAC method assumes the dominance of one wave mode of surface wave. Therefore, the separation of body and surface waves is an important issue to investigate subsurface structure using ambient noise correlations.

In general, three characteristics of waves are commonly used for separating wavefield: dominant frequency, apparent velocity, and polarization. The band-pass frequency filter often separates high-frequency body waves and low-frequency surface waves from a single-component seismogram of a single sensor. However, the frequency filter is not effective for waves with similar frequency characteristics. The separation using a difference in apparent velocity between different wave modes is called velocity filter, which is a common procedure in reflection seismic survey [e.g., Yilmaz, 1987]. Since the velocity filter is mainly performed in frequency-wavenumber domain, a single-component but multichannel observation is necessary for the Fourier space transformation. In contrast, three-component data enable us to analyze the polarization of waves. The knowledge of the polarization of waves helps with identification of different seismic phases and with design of the polarization filter for signal

enhancement [e.g., Shimshoni and Smith, 1964; Flinn, 1965; Montalbetti and Kanasewich, 1970; Vidale et al., 1986]. In addition, using the polarizations of body waves on a free surface, Kennett [1991] decomposed three-component seismograms of a single station into incident P, SV, and SH waves. This procedure was applied for receiver function analysis [Bostock, 1998].

In recently studies related to seismic interferometry, usefulness of three-component analysis and the cross-correlation tensor has also been demonstrated. Nishida et al. [2008a] extracted P and fundamental Rayleigh waves in radial-radial (RR) correlations and fundamental Love waves and its overtones in transverse-transverse (TT) correlations. In addition to the diagonal components of the cross-correlation tensor (ZZ, RR, TT), the cross terms (ZR, ZT, RZ, RT, TZ, TR) are also informative and useful. van Wijk et al. [2011] observationally showed that vertical-radial (ZR) and radial-vertical (RZ) correlations are more robust than ZZ correlations for the Rayleigh wave extraction in the case of anisotropic wave incidence. Haney et al., [2012] theoretically demonstrated the robustness of the ZR correlations and pointed out that the polarization of the waves acts as a spatial filter that weakens the out-of-plane ghost arrivals. The cross terms are also used to draw the particle motion of cross-correlation function, which helps with identification of the wave modes in the extracted wavefield.

In the present study, taking advantage of a difference in polarization between body and Rayleigh waves, we develop a novel method to separate body and Rayleigh waves using the cross terms of the cross-correlation tensor. This method is based on fundamental characteristics of ZR and RZ correlations for differently polarized waves, so that the separating procedure is quite simple and the polarization does not appear explicitly. Moreover, we validate this method using seismic array data at Tono, northeast Japan.

4.2. Characteristic Cross-Correlation Tensor

The original motivation of the present study arose from the observed cross-correlation tensor at Tono array. Figure 4.1 and Figure 4.2 shows the time-symmetric and time-antisymmetric components of the full-component cross-correlation tensor observed at Tono array. The time-symmetric component is computed from a half of sum between the cross-correlations in positive time lag and that in negative time lag, and the time-antisymmetirc components is computed from a half of difference between the positive-lag cross-correlation and the negative-lag cross-correlation. We take the directions of the components Z, R, and T as Figure 4.3. The used data and computational method are described in Section 4.7. As shown in previous studies, Rayleigh waves are extracted in the time-symmetric ZZ, ZR, RZ, and RR components, and Love waves are extracted in the time-symmetric TT components. In addition, we found four interesting points in the observed cross-correlation tensor: (1) P waves dominates in RR component as compared to ZZ component, (2) Rayleigh waves in ZR and RZ components have the opposite signs each other, (3) P waves are clearly extracted in the time-antisymmetric ZR and RZ

components, and (4) P waves in ZR and RZ components have the same signs each other.

The point (1), the dominance of P wave in RR component, is explained by the single-force radiation pattern of P wave. Since seismic interferometry retrieves a complete Green's tensor in ideal case, the ZZ correlation between two stations at x_1 and x_2 can be considered as the vertical displacement at one station x_1 of elastic wave excited by the vertical single force at the other station x_2, termed $G_{ZZ}(x_1,x_2)$. The RR correlation can also be considered as $G_{RR}(x_1,x_2)$: the radial displacement of elastic wave excited by the radial single force. For a point single force in the direction *j* at a source within an infinite homogeneous isotropic medium, the far field displacement of P wave in the direction *i* is proportional to $\gamma_i\gamma_j$, where γ_i and γ_j are *i* and *j* components of the unit vector $\boldsymbol{\gamma}$ from the source to receiver (i.e, direction cosines), respectively [Aki and Richards, 2002]. Therefore, where the source and receiver are on a horizontal plane, the P wave term of Green's tensor $G^P_{ZZ}(x_1,x_2)$ is equal to 0 in far field because of $\gamma_i=\gamma_j=0$. On the other hand, $G^P_{RR}(x_1,x_2)$ has the maximum amplitude because of $\gamma_i=\gamma_j=1$. This is the explanation of the point (1). The vertical heterogeneity turns the P waves vertical and yields ZZ component of P wave. However, the small separation and the hard rock characteristics at Tono array [e.g., Iwasaki et al., 1994] seem to keep the P wave predominance in RR component.

The effect of free surface also yields P wave in ZZ component [Lamb, 1904]. The free surface effect plays a more important role to consider the P wave in ZR and RZ components. That is because the cross terms, $G^P_{ZR}(x_1,x_2)$ and $G^P_{RZ}(x_1,x_2)$, vanish even in near field while $G^P_{ZZ}(x_1,x_2)$ has the near field term [Aki and Richards, 2002; Sánchez-Sesma and Campillo, 2006]. Therefore, the effect of free surface should be considered to explain P waves in ZR and RZ components and points (3) and (4).

The point (2), the relation between the signs of Rayleigh waves in ZR and RZ components, has also been picked up by van Wijk et al. [2010, 2011]. For a vertically heterogeneous medium, the Green's tensor of Rayleigh wave has an antisymmetry as $G^R_{ZR}(x_1,x_2)=-G^R_{RZ}(x_1,x_2)$ because of the reciprocity of Green's tensor and the horizontal symmetry of the vertically heterogeneous medium [Aki and Richards, 2002; van Wijk et al., 2010]. However, the point (3), the sign property of P wave in ZR and RZ component, has not been clarified.

These explanations are based on Green's tensor. However, seismic interferometry guarantees the retrieval of the complete Green's tensor only for the ideal case of isotropic wave incidence [Nakahara, 2006]. In the case of anisotropic wave incidence, the cross-correlation tenor cannot be considered as the Green's tensor. Therefore, taking account of the anisotropic wave incidence, we deal with the cross-correlation tensor as the cross-correlation tensor, not as the Green's tensor, in order to explain the points (2), (3), and (4). Previous theoretical studies on seismic interferometry also treated the anisotropic incidence for scalar wave [Cox, 1973] and for vector surface waves [Haney et al., 2012]. For isotropic incidence of vector body waves, Sánchez-Sesma and Campillo [2006] derived theoretical cross-correlation tensor in infinite homogeneous medium. In the present study, we treat both of the

anisotropic incidence and the effect of free surface for both vector surface and vector body waves.

4.3. Cross Spectra of Uncorrelated Plane Waves

First, we describe the problem setting and the cross spectra of uncorrelated plane waves. Figure 4.3 depicts the setting of our formulation. Two stations are located on the free surface of a homogeneous half space. Without loss of generality, we set one station at the origin. The vertical (Z) axis is positive upward. For the Fourier time transform, we take the same sign convention as Aki and Richards [2002]. We take account of Rayleigh, Love, P, SV, and SH waves as the incident plane waves. We include Love waves for generality although Love waves do not propagate in a homogeneous half space. The vertical displacement $U_Z(r,\xi)$ and the radial displacement $U_R(r,\xi)$ at the station of which radial distance r and azimuth ξ in frequency domain are represented by the superposition of the plane waves as follows:

$$\begin{aligned} U_Z(r,\xi) = & \int_{-\pi}^{\pi} d\varphi A^R(\varphi) w^R e^{ik^R r\cos(\varphi-\xi)} \\ & + \int_0^{\pi/2} d\theta \sin\theta \int_{-\pi}^{\pi} d\varphi A^P(\theta,\varphi) w^P(\theta) e^{ik^P r\sin\theta\cos(\varphi-\xi)} \\ & + \int_0^{\pi/2} d\theta \sin\theta \int_{-\pi}^{\pi} d\varphi A^{SV}(\theta,\varphi) w^{SV}(\theta) e^{ik^{SV} r\sin\theta\cos(\varphi-\xi)} \end{aligned}, \tag{4.1}$$

$$\begin{aligned} U_R(r,\xi) = & \int_{-\pi}^{\pi} d\varphi A^R(\varphi) u^R \cos(\varphi-\xi) e^{ik^R r\cos(\varphi-\xi)} \\ & - \int_{-\pi}^{\pi} d\varphi A^L(\varphi) v^L \sin(\varphi-\xi) e^{ik^L r\cos(\varphi-\xi)} \\ & + \int_0^{\pi/2} d\theta \sin\theta \int_{-\pi}^{\pi} d\varphi A^P(\theta,\varphi) u^P(\theta) \cos(\varphi-\xi) e^{ik^P r\sin\theta\cos(\varphi-\xi)} \\ & + \int_0^{\pi/2} d\theta \sin\theta \int_{-\pi}^{\pi} d\varphi A^{SV}(\theta,\varphi) u^{SV}(\theta) \cos(\varphi-\xi) e^{ik^{SV} r\sin\theta\cos(\varphi-\xi)} \\ & - \int_0^{\pi/2} d\theta \sin\theta \int_{-\pi}^{\pi} d\varphi A^{SH}(\theta,\varphi) v^{SH}(\theta) \sin(\varphi-\xi) e^{ik^{SH} r\sin\theta\cos(\varphi-\xi)} \end{aligned}. \tag{4.2}$$

where φ is the propagation azimuth, θ is the incident angle, A^R, A^L, A^P, A^{SV}, and A^{SH} are the incident wave amplitudes, k^R, k^L, k^P, k^{SV}, and k^{SH} are the wavenumbers, w^R, w^P, and w^{SV} are the vertical component of the free-surface response functions, u^R, u^P, and u^{SV} are the radial component of the response functions, v^L and v^{SH} are the transverse component of the response functions, and the superscripts *R*, *L*, *P*, *SV* and *SH* represent Rayleigh, Love, P, SV and SH waves, respectively. The response functions are the displacement at the free surface with respect to the unit-amplitude incident plane waves. The subscript *Z* and *R* represent the vertical and vertical components, respectively. While the direction of the displacement U_R is taken with respect to the station pair, the direction of the response functions u and v are taken with respect to the propagation direction of plane waves. The exponential parts are from the phase difference between the origin and the station (r,ξ). The cosine and sine terms in U_R are from the polarization of the waves.

Using equations (4.1) and (4.2), we can represent the cross spectra between the two stations by double, triple, and quadruple integrals for the azimuth and the incident angle as follows:

$$
\begin{aligned}
U_Z^*(0,\xi)U_Z(r,\xi) = &\int_{-\pi}^{\pi} d\varphi \int_{-\pi}^{\pi} d\varphi' \left[A^{R*}(\varphi)A^R(\varphi')\right]\left[w^{R*}w^R\right] e^{ik^R r\cos(\varphi'-\xi)} \\
&+\int_0^{\pi/2} d\theta' \sin\theta' \int_{-\pi}^{\pi} d\varphi \int_{-\pi}^{\pi} d\varphi' \left[A^{R*}(\varphi)A^P(\theta',\varphi')\right]\left[w^{R*}w^P(\theta')\right] e^{ik^P r\sin\theta'\cos(\varphi'-\xi)} \\
&+\cdots
\end{aligned}, \tag{4.3}
$$

$$
\begin{aligned}
U_Z^*(0,\xi)U_R(r,\xi) = &\int_{-\pi}^{\pi} d\varphi \int_{-\pi}^{\pi} d\varphi' \left[A^{R*}(\varphi)A^R(\varphi')\right]\left[w^{R*}u^R\right]\cos(\varphi'-\xi) e^{ik^R r\cos(\varphi'-\xi)} \\
&-\int_{-\pi}^{\pi} d\varphi \int_{-\pi}^{\pi} d\varphi' \left[A^{R*}(\varphi)A^L(\varphi')\right]\left[w^{R*}v^L\right]\sin(\varphi'-\xi) e^{ik^L r\cos(\varphi'-\xi)} \\
&+\int_0^{\pi/2} d\theta' \sin\theta' \int_{-\pi}^{\pi} d\varphi \int_{-\pi}^{\pi} d\varphi' \left[A^{R*}(\varphi)A^P(\theta',\varphi')\right]\left[w^{R*}u^P(\theta')\right]\cos(\varphi'-\xi) e^{ik^P r\sin\theta'\cos(\varphi'-\xi)} \\
&+\cdots
\end{aligned}, \tag{4.4}
$$

$$
\begin{aligned}
U_R^*(0,\xi)U_Z(r,\xi) = &\int_{-\pi}^{\pi} d\varphi \int_{-\pi}^{\pi} d\varphi' \left[A^{R*}(\varphi)A^R(\varphi')\right]\left[u^{R*}w^R\right]\cos(\varphi-\xi) e^{ik^R r\cos(\varphi'-\xi)} \\
&-\int_{-\pi}^{\pi} d\varphi \int_{-\pi}^{\pi} d\varphi' \left[A^{L*}(\varphi)A^R(\varphi')\right]\left[v^{L*}w^R\right]\sin(\varphi-\xi) e^{ik^R r\cos(\varphi'-\xi)} \\
&+\int_0^{\pi/2} d\theta \sin\theta \int_{-\pi}^{\pi} d\varphi \int_{-\pi}^{\pi} d\varphi' \left[A^{P*}(\theta,\varphi)A^R(\varphi')\right]\left[u^{P*}(\theta)w^R\right]\cos(\varphi-\xi) e^{ik^R r\cos(\varphi'-\xi)} \\
&+\cdots
\end{aligned}, \tag{4.5}
$$

where * denotes complex conjugate. The first term in equation (4.3) is the cross spectrum between the vertical Rayleigh waves, and the second term is between the vertical Rayleigh and vertical P waves. The first, second, and third terms in equations (4.4) and (4.5) are the cross spectra between the vertical Rayleigh and horizontal Rayleigh waves, between the vertical Rayleigh and horizontal Love waves, and between the vertical Rayleigh and horizontal P waves, respectively. Equations (4.3-4.5) contain the contributions from waves propagating in different directions and from different wave modes.

Here, we make an assumption that the incident waves are in random phase and uncorrelated. Assuming the incident waves that propagate in different directions are uncorrelated, we may write the ensemble averages of the incident waves as

$$
\left\langle A^{R*}(\varphi)A^R(\varphi')\right\rangle = \frac{\left\langle \left|A^R(\varphi)\right|^2 \right\rangle}{2\pi}\delta(\varphi-\varphi'), \tag{4.6}
$$

$$
\left\langle A^{P*}(\theta,\varphi)A^P(\theta',\varphi')\right\rangle = \frac{\left\langle \left|A^P(\theta,\varphi)\right|^2 \right\rangle}{2\pi\sin\theta}\delta(\theta-\theta')\delta(\varphi-\varphi'), \tag{4.7}
$$

where $\langle\ \rangle$ represents the ensemble average, δ is the delta function, $\left\langle \left|A^R(\varphi)\right|^2 \right\rangle$ is the power spectrum of the incident Rayleigh wave propagating in the direction φ, referred to as the angular power spectrum, and $\left\langle \left|A^P(\theta,\varphi)\right|^2 \right\rangle$ is the angular power spectrum of P wave. Love wave also satisfies the same equation as equation (4.6), and SV and SH waves also satisfy equation (4.7). We also assume that different wave modes are uncorrelated such that, for example, between Rayleigh and the other wave modes,

$$
\left\langle A^{R*}(\varphi)A^L(\varphi')\right\rangle = 0, \tag{4.8}
$$

$$\left\langle A^{R*}(\varphi)A^{P}(\theta',\varphi')\right\rangle = \left\langle A^{R*}(\varphi)A^{SV}(\theta',\varphi')\right\rangle = \left\langle A^{R*}(\varphi)A^{SH}(\theta,\varphi')\right\rangle = 0\,. \tag{4.9}$$

Therefore, by taking the ensemble averages and using the assumption of the uncorrelated waves, we can separately evaluate the contributions of Rayleigh, P and SV waves for ZZ, ZR and RZ components of the cross spectra as follows:

$$\phi_{ZZ}(r,\xi) = \left\langle U_Z^*(0,\xi)U_Z(r,\xi)\right\rangle = \phi_{ZZ}^R(r,\xi) + \phi_{ZZ}^P(r,\xi) + \phi_{ZZ}^{SV}(r,\xi)\,, \tag{4.10}$$

$$\phi_{ZR}(r,\xi) = \left\langle U_Z^*(0,\xi)U_R(r,\xi)\right\rangle = \phi_{ZR}^R(r,\xi) + \phi_{ZR}^P(r,\xi) + \phi_{ZR}^{SV}(r,\xi)\,, \tag{4.11}$$

$$\phi_{RZ}(r,\xi) = \left\langle U_R^*(0,\xi)U_Z(r,\xi)\right\rangle = \phi_{RZ}^R(r,\xi) + \phi_{RZ}^P(r,\xi) + \phi_{RZ}^{SV}(r,\xi)\,, \tag{4.12}$$

where the subscripts *ZZ*, *ZR*, and *RZ* represent the ZZ, ZR, and RZ components, respectively, $\phi_{ZZ}(r,\xi)$, $\phi_{ZR}(r,\xi)$, and $\phi_{RZ}(r,\xi)$ are the observed cross-spectral tensor for a station pair with the separation r and the azimuth ξ, ϕ_{ZZ}^R, ϕ_{ZR}^R, and ϕ_{RZ}^R are the cross spectra of Rayleigh wave, ϕ_{ZZ}^P, ϕ_{ZR}^P, and ϕ_{RZ}^P are the cross spectra of P wave, and ϕ_{ZZ}^{SV}, ϕ_{ZR}^{SV}, and ϕ_{RZ}^{SV} are the cross spectra of SV wave. Since Love and SH waves do not have a vertical component, the ZZ, ZR and RZ components of the cross spectra do not have the contributions of Love and SH waves.

4.4. Relationship between ZR and RZ Cross Spectra

Here, we show fundamental relationships between the ZR and RZ components of the cross-spectral tensor. According to equation (4.3-4.6) and previous studies [Aki, 1957; Cox, 1973; Haney et al., 2012], the cross spectra for Rayleigh wave can be represented by the following integrals,

$$\phi_{ZZ}^R(r,\xi) = \frac{1}{2\pi}\int_{-\pi}^{\pi} d\varphi I^R(\varphi)\left[w^{R*}w^R\right]e^{ik^R r\cos(\varphi-\xi)}\,, \tag{4.13}$$

$$\phi_{ZR}^R(r,\xi) = \frac{1}{2\pi}\int_{-\pi}^{\pi} d\varphi I^R(\varphi)\left[w^{R*}u^R\right]\cos(\varphi-\xi)e^{ik^R r\cos(\varphi-\xi)}\,, \tag{4.14}$$

$$\phi_{RZ}^R(r,\xi) = \frac{1}{2\pi}\int_{-\pi}^{\pi} d\varphi I^R(\varphi)\left[u^{R*}w^R\right]\cos(\varphi-\xi)e^{ik^R r\cos(\varphi-\xi)}\,. \tag{4.15}$$

Here, we rewrite the angular power spectrum as $\left\langle\left|A^R(\varphi)\right|^2\right\rangle = I^R(\varphi)$. Important terms in the present study are the cross spectra between the response functions, w^R and u^R. In general, $w^{R*}w^R$ is real, and $w^{R*}u^R$ and $u^{R*}w^R$ are a complex conjugate pair. In the case of Rayleigh wave incidence, since Rayleigh wave has an elliptic particle motion, the response functions satisfy the following relationship as,

$$w^R = 1\,, \tag{4.16}$$

$$u^R = iHw^R\,, \tag{4.17}$$

where i is the imaginary unit, and H is the horizontal over vertical ratio of Rayleigh wave. We defined the

incident amplitude of Rayleigh wave as equation (4.16). A positive value of *H* gives a prograde particle motion. Here, for simplicity, we only consider positive frequencies, otherwise the sign function with respect to angular frequency ω, $\mathrm{sgn}(\omega)$, is necessary in equation (4.17). According to equations (4.16) and (4.17), $w^{R*}u^{R}$ and $u^{R*}w^{R}$ are pure imaginary number and have the opposite signs each other. Therefore, the following relationship holds for Rayleigh wave as [van Wijk et al., 2011; Haney et al., 2012],

$$\phi_{ZR}^{R} = -\phi_{RZ}^{R} . \tag{4.18}$$

Similarly, for P wave incidence, the cross spectra can be represented by the following integrals as,

$$\phi_{ZZ}^{P}(r,\xi) = \frac{1}{2\pi}\int_{0}^{\pi/2} d\theta \sin\theta \int_{-\pi}^{\pi} d\varphi I^{P}(\theta,\varphi)\left[w^{P*}(\theta)w^{P}(\theta)\right] e^{ik^{P}r\sin\theta\cos(\varphi-\xi)} , \tag{4.19}$$

$$\phi_{ZR}^{P}(r,\xi) = \frac{1}{2\pi}\int_{0}^{\pi/2} d\theta \sin\theta \int_{-\pi}^{\pi} d\varphi I^{P}(\theta,\varphi)\left[w^{P*}(\theta)u^{P}(\theta)\right]\cos(\varphi-\xi) e^{ik^{P}r\sin\theta\cos(\varphi-\xi)} , \tag{4.20}$$

$$\phi_{RZ}^{P}(r,\xi) = \frac{1}{2\pi}\int_{0}^{\pi/2} d\theta \sin\theta \int_{-\pi}^{\pi} d\varphi I^{P}(\theta,\varphi)\left[u^{P*}(\theta)w^{P}(\theta)\right]\cos(\varphi-\xi) e^{ik^{P}r\sin\theta\cos(\varphi-\xi)} , \tag{4.21}$$

where $I^{P}(\theta,\varphi) = \left\langle \left| A^{P}(\theta,\varphi) \right|^{2} \right\rangle$. In contrast to the elliptic particle motion of Rayleigh wave, P wave has a rectilinear particle motion. Since $u^{P}(\theta)$ and $w^{P}(\theta)$ are always real for P wave incidence (Appendix 4.A), $w^{P*}u^{P}$ is identical to $u^{P*}w^{P}$. Therefore, the ZR and RZ components satisfy the relationship that is different from equation (4.18) as,

$$\phi_{ZR}^{P} = \phi_{RZ}^{P} . \tag{4.22}$$

For SV wave incidence, the integral expressions of the cross spectra are similar to equations (4.19-4.21) for the P wave incidence. However, $u^{SV}(\theta)$ and $w^{SV}(\theta)$ become complex numbers where the incident angle θ exceeds the critical angle (Appendix 4.A). Consequently, for SV wave, the ZR and RZ components do not have a simple relationship in general case. In order to consider the SV wave contribution in more detail, we divide the incident SV waves into nearly vertical and nearly horizontal incidences with respect to the critical angle θ_{c} as,

$$\phi_{ZR}^{SVv}(r,\xi) = \frac{1}{2\pi}\int_{0}^{\theta_{c}} d\theta \sin\theta \int_{-\pi}^{\pi} d\varphi I^{SV}(\theta,\varphi)\left[w^{SV*}(\theta)u^{SV}(\theta)\right]\cos(\varphi-\xi) e^{ik^{SV}r\sin\theta\cos(\varphi-\xi)} , \tag{4.23}$$

$$\phi_{ZR}^{SVh}(r,\xi) = \frac{1}{2\pi}\int_{\theta_{c}}^{\pi/2} d\theta \sin\theta \int_{-\pi}^{\pi} d\varphi I^{SV}(\theta,\varphi)\left[w^{SV*}(\theta)u^{SV}(\theta)\right]\cos(\varphi-\xi) e^{ik^{SV}r\sin\theta\cos(\varphi-\xi)} , \tag{4.24}$$

where ϕ_{ZR}^{SVv} and ϕ_{ZR}^{SVh} are the cross spectra of the nearly vertical and nearly horizontal SV waves, respectively, and $I^{SV}(\theta,\varphi) = \left\langle \left| A^{SV}(\theta,\varphi) \right|^{2} \right\rangle$. As shown in Appendix 4.A, the nearly vertical and nearly horizontal SV wave incidences result in rectilinear and elliptic particle motions, respectively, on a free surface. Accordingly, the following equations hold for SV wave as,

$$\phi_{ZR}^{SVv} = \phi_{RZ}^{SVv} , \tag{4.25}$$

$$\phi_{ZR}^{SVh} = -\phi_{RZ}^{SVh} . \tag{4.26}$$

Therefore, generally speaking, waves that have an elliptic motion on the free surface satisfy equation (4.18) and waves that have a rectilinear motion on the free surface satisfy equation (4.22).

Equations (4.18) and (4.22) are the key for the separation of Rayleigh and P waves. These relationships imply that the summation between ZR and RZ correlations cancels out the Rayleigh wave contribution and retains the P wave contribution. In contrast, the difference between ZR and RZ correlations cancels out the P wave contribution and retains the Rayleigh wave contribution. Therefore, by taking the sum and difference of ZR and RZ correlations, we can separate P and Rayleigh waves.

Here, we discuss the validity condition. Equation (4.18) and (4.22) are derived for a fundamental-mode Rayleigh wave and a direct P wave within a homogeneous half space. A vertically heterogeneous medium yields higher-mode Rayleigh waves, fundamental- and higher-mode Love waves, and reflected and refracted P, SV, and SH waves. For Love and SH waves, the ZR and RZ correlations do not have the contributions of Love and SH waves because of non-vertical particle motions of Love and SH waves and the assumption of the uncorrelated waves. For higher-mode Rayleigh waves, equation (4.18) still holds because the particle motions of the higher-mode Rayleigh waves are also elliptic. For P and SV waves, the incidence on a high-velocity layer may shift the phase between the vertical and radial response functions, so that the cross spectra of the vertical and radial response functions, $w^* u$, become a complex number. However, what is important is that the real part of $w^* u$ contributes the sum of ZR and RZ correlations and the imaginary part contributes the difference of ZR and RZ correlations. This is also said for diffracted and scattered waves within more complex structures. Consequently, the use of the sum and difference of ZR and RZ correlations may efficiently separate body and Rayleigh waves even in more realistic structures compared to a homogeneous half space.

4.5. Representation of Cross Spectra for Isotropic Incidence

Integrating the equations (4.13-4.15) and (4.19-4.21), we show concrete expressions of the cross spectra. At first, we start from isotropic wave incidences as

$$I^R(\varphi) = a_0^R, \tag{4.27}$$

$$I^P(\theta,\varphi) = a_0^P. \tag{4.28}$$

The following integral representation of Bessel function [Abramowitz and Stegun, 1972],

$$2\pi i^m J_m(z) = \int_{-\pi}^{\pi} d\varphi \cos(m\varphi) e^{iz\cos\varphi}, \tag{4.29}$$

is helpful to perform the integrals over azimuth φ analytically, where m is an integer number, z is generally a complex number, i^m is the mth power of the imaginary unit, and J_m is the mth order Bessel function. According to equations (4.13-4.17), (4.27) and (4.29), the ZZ, ZR and RZ components of the cross spectra for the isotropic Rayleigh wave incidence are given by

$$\phi_{ZZ}^{R}(r) = a_0^R J_0\left(k^R r\right), \tag{4.30}$$

$$\phi_{ZR}^{R}(r) = -Ha_0^R J_1\left(k^R r\right), \tag{4.31}$$

$$\phi_{RZ}^{R}(r) = Ha_0^R J_1\left(k^R r\right). \tag{4.32}$$

Here, J_0 and J_1 are the 0th and 1st order Bessel functions of the 1st kind. Haney et al. [2012] have also derived the same expressions. According to equations (4.30-4.32), the ZZ, ZR and RZ components of the cross-spectral tensor are real and do not have imaginary part.

For P wave incidence, the integrals over azimuth can be performed in the same way as the case of Rayleigh wave. Additionally, the integrals over incident angle are evaluated numerically as,

$$\phi_{ZZ}^{P}(r) = a_0^P \int_0^{\pi/2} d\theta \sin\theta \left[w^{P*}(\theta) w^{P}(\theta)\right] J_0\left(k^P r \sin\theta\right), \tag{4.33}$$

$$\phi_{ZR}^{P}(r) = ia_0^P \int_0^{\pi/2} d\theta \sin\theta \left[w^{P*}(\theta) u^{P}(\theta)\right] J_1\left(k^P r \sin\theta\right), \tag{4.34}$$

$$\phi_{RZ}^{P}(r) = ia_0^P \int_0^{\pi/2} d\theta \sin\theta \left[u^{P*}(\theta) w^{P}(\theta)\right] J_1\left(k^P r \sin\theta\right). \tag{4.35}$$

In contrast to Rayleigh wave, the ZZ component is real, and the ZR and RZ components are pure imaginary because w^P and u^P are always real. For SV wave incidence, the cross spectra also satisfy equations (4.33-4.35). Since $w^{SV*}(\theta)u^{SV}(\theta)$ and $u^{SV*}(\theta)w^{SV}(\theta)$ are pure real from 0º to the critical angle and are pure imaginary from the critical angle to 90º (Appendix 4.A), ϕ_{ZR}^{SV} and ϕ_{RZ}^{SV} are complex values. Considering $w^{SV*}(\theta)u^{SV}(\theta)$ and $u^{SV*}(\theta)w^{SV}(\theta)$ are complex conjugate each other, we can find the following relationship for isotropic SV wave incidence as

$$\phi_{ZR}^{SV} = -\phi_{RZ}^{SV*}. \tag{4.36}$$

The key is the pure real ϕ_{ZR}^{R} and the pure imaginary ϕ_{ZR}^{P}. The fact means that the ZR and RZ components of cross-correlation function are time-symmetric for Rayleigh wave and time-antisymmetric for P wave. Therefore, the time-symmetric part of cross-correlation ϕ_{ZR}^{R} is related to Rayleigh and SV waves without P wave, and the time-antisymmetric part is related to P and SV waves without Rayleigh wave. Accordingly, in the case of isotropic incidence, we can separate Rayleigh and P waves by just taking the time-symmetric and time-antisymmetric parts of ZR correlations without using sum and difference of ZR and RZ correlations.

We numerically check the cross spectra for Rayleigh, P, and SV wave incidences. We assume a homogeneous half space with $V_P = 6.0$ km/s, $V_P/V_S = \sqrt{3}$, $V_R = 3.18$ km/s, and $H = -0.68$, where V_P is P wave velocity, V_S is S wave velocity, and V_R is Rayleigh wave phase velocity. The incident wave power of Rayleigh wave a_0^R is set to 1.0, and the incidence wave powers of P and SV waves, a_0^P

and a_0^{SV}, are set to 0.5. Figure 4.4(a) depicts the cross spectra at 1.0 Hz. Decays of P and SV wave contributions are faster than that of Rayleigh wave because of the difference in geometrical spreading between two-dimensional ($1/\sqrt{r}$) and three-dimensional ($1/r$) waves. For the ZZ component, all contributions of Rayleigh, P, and SV waves are real. However, for the ZR and RZ components, the Rayleigh wave contributions are real and the P wave contributions are pure imaginary. Accordingly, if the ambient noise is isotropic, Rayleigh and P waves can be separated by the time-symmetric and time-antisymmetric components of the cross-correlation functions. In addition, comparing the ZR and RZ components, we show the opposite signs of Rayleigh waves and the same signs of P waves, which enable the separation of Rayleigh and P waves in the difference and summation of the ZR and RZ correlations.

Figure 4.4(b) shows time domain cross-correlation functions for the case of the isotropic incidence of Rayleigh, P, and SV waves. The time domain cross-correlation functions are computed by applying the inverse Fourier transform to the cross spectra in a frequency range of 1.0-2.0 Hz. The geometrical spreading factors are corrected by multiplying $\sqrt{r}$ for both Rayleigh and body waves, so that P and SV waves decay with separation distance. In time domain, we can easily recognize (1) the opposite signs of Rayleigh wave and the same signs of P waves between the ZR and RZ correlations and (2) the time-symmetric Rayleigh waves and the time-antisymmetric P waves in the ZR and RZ correlations. Note that P wave propagation is retrieved from not only the P wave incidence but also the SV wave incidence. That is because the incident SV waves are converted to P waves at the free surface. According to equations (4.25) and (4.26), nearly horizontal and nearly vertical SV waves contribute to the summation and difference of ZR and RZ correlations, respectively.

4.6. Representation of Cross Spectra for Anisotropic Incidence

Although isotropic wave incidence is necessary for the Green's function retrieval by seismic interferometry [Nakahara, 2006], incidence of ambient noise is generally not isotropic in real data [e.g., van Wijk et al., 2011; Harmon et al., 2010]. Therefore, we show the cross spectra in the case of anisotropic wave incidence. In order to consider anisotropic wave incidence, we expand the angular power spectra by a Fourier series for Rayleigh wave and by a spherical harmonics for P and SV waves [Cox, 1973] as,

$$I^R(\varphi) = a_0^R + 2\sum_{m=1}^{\infty}\left(a_m^R \cos m\varphi + b_m^R \sin m\varphi\right), \tag{4.37}$$

$$I^P(\theta,\varphi) = a_0^P + \sum_{n=1}^{\infty}\sum_{m=0}^{n}\left(a_{nm}^P \cos m\varphi + b_{nm}^P \sin m\varphi\right)P_n^m(\cos\theta), \tag{4.38}$$

where a_m and b_m are the coefficients of the Fourier series, a_{nm} and b_{nm} are the coefficients of the spherical harmonics, a_0^P is identical to a_{00}^P, and P_n^m is the associated Legendre polynomial of the nth degree and mth order. After substituting equation (4.37) to (4.13, 4.14) and (4.38) to (4.19, 4.20), we

performed the integrals over azimuth φ analytically using the integral representation of Bessel function (equation (4.29)) and the addition theorem of trigonometric functions as follows (Appendix 4.B):

$$\phi_{ZZ}^{R}(r,\xi) = a_0^R J_0(kr) + 2\sum_{m=1}^{\infty} i^m c_m^R(\xi) J_m(k^R r), \tag{4.39}$$

$$\phi_{ZR}^{R}(r,\xi) = -Ha_0^R J_1(kr) - 2H\sum_{m=1}^{\infty} i^m c_m^R(\xi) \frac{J_{m+1}(k^R r) - J_{m-1}(k^R r)}{2}, \tag{4.40}$$

$$\phi_{ZZ}^{P}(r,\xi) = \sum_{n=0}^{\infty}\sum_{m=0}^{n} i^m c_{nm}^P(\xi) \int_0^{\pi/2} d\theta \sin\theta \left[w^{P*}(\theta) w^P(\theta)\right] P_n^m(\cos\theta) J_m(k^P r\sin\theta), \tag{4.41}$$

$$\phi_{ZR}^{P}(r,\xi) = i\sum_{n=0}^{\infty}\sum_{m=0}^{n} i^m c_{nm}^P(\xi) \int_0^{\pi/2} d\theta \sin\theta \left[w^{P*}(\theta) u^P(\theta)\right] P_n^m(\cos\theta) \frac{J_{m+1}(k^P r\sin\theta) - J_{m-1}(k^P r\sin\theta)}{2}. \tag{4.42}$$

Azimuthal dependences are represented by $c_m^R(\xi)$ and $c_{nm}^P(\xi)$ as,

$$c_m^R(\xi) = a_m^R \cos m\xi + b_m^R \sin m\xi, \tag{4.43}$$

$$c_{nm}^R(\xi) = a_{nm}^R \cos m\xi + b_{nm}^R \sin m\xi. \tag{4.44}$$

According to equations (4.39-4.41), the odd order terms (m=1, 3, 5, ...) of the Fourier series and spherical harmonics result in the imaginary part of the cross spectra, ϕ_{ZZ}^R, ϕ_{ZR}^R, and ϕ_{ZZ}^P, which means that the cross-correlation functions have the time-antisymmetric component [Harmon et al., 2010; Haney et al., 2012]. Similarly, from equation (4.42), the odd order terms of the spherical harmonics contribute to the real part of the ZR component cross spectra of P wave ϕ_{ZR}^P. Therefore, in the case of anisotropic incidence, we cannot separate Rayleigh and P wave contributions by just taking the time-symmetric and time-antisymmetric parts of the cross-correlation functions. However, equations (4.18) and (4.22) still hold even in the case of anisotropic incidence. By taking the sum and difference of the ZR and RZ correlations, we can separate Rayleigh and P wave contributions to the cross-correlation functions.

Note that the procedure that takes the time-symmetric and time-antisymmetric parts of the cross-correlation functions is meaningful for diminishing the effect of anisotropic wave incidence. For measurements of phase or group velocity of Rayleigh wave, the time-symmetric parts of ZZ correlations are often used [e.g., Bensen et al., 2007]. As shown in equation (4.39) and by previous studies [Weaver et al., 2009; Harmon et al., 2010], the time-symmetric ZZ correlations remove the contributions of the odd order terms of the Fourier series representing Rayleigh wave source distribution (equation (4.37)). Similarly, by using the time-antisymmetric parts of the ZR and RZ components of cross-correlation functions, we can remove the odd order terms of the P wave source distribution.

As a summary, we point out that we can separate Rayleigh and P wave contributions to the ZR and RZ components of the cross-correlation tensor by taking the time-symmetric part of the difference between the ZR and RZ components and by taking the time-antisymmetric part of the summation between the ZR and RZ components. The time-symmetric part of the difference is only related to Rayleigh and SV waves without P wave. The time-antisymmetric part of the summation is only related to

P and SV waves without Rayleigh wave.

4.7. Application to Tono Array Data

In order to validate our method, we analyzed ambient noise records observed at Tono array in northeastern Japan that is managed by Tohoku University. Figure 4.5 shows a map of Tono array. Tono array is located in the Kitakami mountain region characterized by granite hard rock [e.g., Iwasaki et al., 1994]. Tono array consists of 10 high sensitivity broadband sensors (STS-1 or STS-2). The minimum and maximum separations of the stations are 2.4 km and 18 km, respectively. We used three-component records during one year in 2010.

We computed ZZ, ZR and RZ cross spectra for all possible pairs of stations. First, we divided the continuous records into 60-s-long records with an overlap of 30 s. Then, after removing offsets, discarding segments that include earthquake, and correcting the instrumental response, we computed averaged cross spectra of all segments as follows:

$$\phi_{ij,\alpha\beta} = \frac{\left\langle F^{*}_{i,\alpha} \cdot F_{j,\beta} \right\rangle}{\left\langle |F_i| \right\rangle \left\langle |F_j| \right\rangle}, \tag{4.45}$$

$$\left\langle |F_i| \right\rangle = \sqrt{\left(\left\langle |F_{i,Z}|^2 \right\rangle + \left\langle |F_{i,N}|^2 \right\rangle + \left\langle |F_{i,E}|^2 \right\rangle \right) / 3}\,. \tag{4.46}$$

$F_{i,\alpha}$ denotes the Fourier spectra of α th component of *i*th station, where *i* and *j* indicate station number and α and β indicate Z or R components. $\langle\ \rangle$ represents the ensemble average over all segments. The cross spectra are normalized by the averaged power spectra of three-component data as shown by equation (4.46), so that the relative amplitude between different components are preserved. We obtained the time-symmetric cross-correlation functions from the inverse Fourier transform of the real part of equation (4.45) with zero imaginary part, which corresponds to the average of cross-correlation functions at positive time lags and that at negative time lags in time domain. We also obtained the time-antisymmetric cross-correlations from the imaginary part of equation (4.45), which corresponds to the difference between the positive-lag correlation and the negative-lag correlation.

Figure 4.6 shows the observed cross-correlation functions in a frequency range of 0.5-2.0 Hz. The cross-correlation functions are averaged in every 1 km bin of separation distance. In the time-symmetric parts of the ZZ components, Rayleigh wave propagation is obvious with a propagation velocity of about 3 km/s. The large amplitude in the antisymmetric parts of the ZZ correlations implies strong anisotropy of the incident Rayleigh wave. Although the bin average plays a role of azimuthal average partially, we cannot eliminate the contribution of anisotropic incidence completely because of the small number of seismic stations and the irregular shape of Tono array. In addition to Rayleigh wave, we can recognize P wave with small amplitude in the time-symmetric ZZ correlations around 1 second from 5 to 10 km range. In the ZR and RZ correlations, we can see clear P waves with the contribution of anisotropic Rayleigh

wave in the antisymmetric parts. These P wave signals are separated from the anisotropic Rayleigh waves by taking the summation of the ZR and RZ correlations. Although vertical heterogeneity turns body waves vertical, the hard rock property and short separation distance at Tono array appear to keep the dominance of P waves in horizontal component. We were also able to sharpen up the Rayleigh wave parts by taking the difference of the ZR and RZ correlations without the contributions of the anisotropic P wave. As shown here, the developed method is validated by the analysis of Tono array data.

What is surprising about our observation is large amplitude of P waves that is comparable to Rayleigh waves. That might be because the frequency range of this study is much higher than that of microseisms. Ambient noise may be composed of surface and body waves in high frequencies. The ratio of surface and body waves in ambient noise can be estimated by fitting the theoretical cross spectra presented by this study to the observed cross spectra. That will be a subject of our future study.

4.8. Discussion and Conclusions

We have developed a novel method to separate body and Rayleigh waves using the cross-correlation tensor of random wavefield. The method is based on two fundamental characteristics obtained by the present study: (1) the opposite signs between ZR and RZ correlations for Rayleigh wave and the same signs between ZR and RZ correlations for P wave, and (2) the time-symmetric correlations in the case of isotropic Rayleigh wave incidence and the time-antisymmetric correlations in the case of isotropic P wave incidence.

According to these characteristics of the ZR and RZ correlations, we have succeeded in separating Rayleigh and P waves in ambient noise correlations at Tono array. From the time-symmetric parts of the difference between ZR and RZ correlations, Rayleigh wave propagation is extracted. On the other hand, from the time-antisymmetric parts of the summation between ZR and RZ correlations, P wave propagation is clearly retrieved without Rayleigh wave propagation. This analysis has validated the method.

Here, we discuss four advantages of the method. The first one is the needlessness of any knowledge of velocity structure. The fact means that we can investigate velocity structure and/or wavefield with less assumption. The second one is the compactness of the required observation. The separation requires only two stations with three-component sensor on a free surface, which is obviously advantageous as compared with the commonly used velocity filter that requires a dense and regularly separated multichannel observation. In practice, of course, array observations are better for identifying the propagations of separated P and Rayleigh waves. The third one is the breadth of applicable condition for noise source distribution. The sign properties between ZR and RZ correlations hold even in the case of anisotropic wave incidence, which is more realistic for actual observations. The last one is the simplicity of the separating procedure. Since the method is based on the fundamental characteristics of ZR and RZ

correlations, any complex computation is not required such as matrix operations and the least squares. That might be important for actual applications.

Next, we would like to point out advantages of the cross terms of the cross-correlation tensor. We consider that the ZR and RZ correlations have three advantages compared with ZZ and RR correlations. First, in the ZR and RZ correlations, the contributions of P and Rayleigh waves are independent each other as presented by this study. Secondly, the ZR and RZ correlations have resiliency for anisotropic incidence as compared with the ZZ correlation, which was demonstrated by previous studies [van Wijk et al., 2011; Haney et al., 2012]. Thirdly, the ZR and RZ correlations are simpler than the RR correlations because the ZR and RZ correlations do not have contributions from Love and SH waves.

Furthermore, we point out that the method reflects an advantage of seismic interferometry that can reconstract the full-component cross-correlation tensor or Green's tensor. From explosion or earthquake data, however, we observe the superposition of the different components of Green's tensor. Only after computing cross-correlations, we can obtain the ZR and RZ components of Green's tensor. In that sense, we consider that the method is based on the advantage of seismic interferometry.

Finally, we discuss three potential applications of the method. The first application is microtremor survey for near surface structure. Applying the method for three-component arrays, we can obtain more robust estimation of the spatial auto-correlation even where body wave energy is not negligible as shown in Tono array. The robust estimation gives accurate shallow velocity structure, which is important for the prediction of strong ground motions. The second application is the investigation of deep structure. Using both of body and Rayleigh waves extracted by the method, we will be able to explore deep structure with higher depth resolution. The last application is related to a more fundamental question about the nature of ambient noise. The composition of ambient noise can be quantitatively estimated by applying this method to array observations. Recently, three-component and continuous observation has become commonplace. As described above, this study has provided a way to make effective use of the three-component observations of ambient noise.

Appendix 4.A: Response Functions for P and SV Wave Incidences

We show the response functions on a free surface for the case of P wave incidence and SV wave incidence [Aki and Richards, 2002]. Note that the vertical axis is positive upward in the present study and is different from positive downward z-axis by Aki and Richards [2002]. For P wave incidence,

$$w^{P}(\theta) = \frac{2\xi\left(\eta^2 - p^2\right)\left(\eta^2 + p^2\right)}{\left(\eta^2 - p^2\right)^2 + 4p^2\xi\eta} V_P \,, \tag{4.A1}$$

$$u^P(\theta) = \frac{4p\xi\eta\left(\eta^2 + p^2\right)}{\left(\eta^2 - p^2\right)^2 + 4p^2\xi\eta} V_P \,, \tag{4.A2}$$

where p is the horizontal slowness, ξ is the vertical slowness of P wave, and η is the vertical slowness of SV wave. The slownesses are real functions of the incident angle θ as follows:

$$p = \sin\theta / V_P \,, \quad \xi = \sqrt{1/V_P^2 - p^2} \,, \quad \eta = \sqrt{1/V_S^2 - p^2} \,. \tag{4.A3}$$

For SV wave incidence,

$$w^{SV}(\theta) = -\frac{4p\xi\eta\left(\eta^2 + p^2\right)}{\left(\eta^2 - p^2\right)^2 + 4p^2\xi\eta} V_S \,, \tag{4.A4}$$

$$u^{SV}(\theta) = \frac{2\eta\left(\eta^2 - p^2\right)\left(\eta^2 + p^2\right)}{\left(\eta^2 - p^2\right)^2 + 4p^2\xi\eta} V_S \,, \tag{4.A5}$$

where ξ becomes imaginary number above the critical angle. The slownesses are represented by

$$p = \sin\theta / V_S \,, \quad \xi = \begin{cases} \sqrt{1/V_P^2 - p^2} & \left(1/V_P^2 \geq p^2\right) \\ i\sqrt{p^2 - 1/V_P^2} & \left(1/V_P^2 < p^2\right) \end{cases} \,, \quad \eta = \sqrt{1/V_S^2 - p} \,. \tag{4.A6}$$

Above the critical angle, the ratio between the radial and vertical displacements is

$$\frac{u^{SV}}{w^{SV}} = -\frac{\eta^2 - p^2}{2p\xi} = i\frac{\eta^2 - p^2}{2p\sqrt{p^2 - 1/V_S^2}} \,, \tag{4.A7}$$

where p and η are always real. Therefore, the phase difference between the vertical and radial components is $\pi/2$, which means that the particle motion is elliptic.

Figure 4.A1 shows the cross spectra between the response functions. For P wave, the cross spectra of $w^{P*}w^P$, $w^{P*}u^P$ and $w^{SV*}w^{SV}$ are always real. $w^{SV*}u^{SV}$ is real from 0º (vertical) to the critical angle (approximately 35º) and is pure imaginary from the critical angle to 90º (horizontal).

Appendix 4.B: Derivation of Cross Spectra for Anisotropic Wave Incidence

We derive equations (4.39) and (4.40) by integrating equations (4.13) and (4.14). We followed the derivation by Cox [1973] for ZZ component and newly derived similar expression for ZR component. The following transformation of valuables in the Fourier series expansion of equation (4.37) is helpful for the integration as,

$$I^R(\varphi) = \sum_{m=1}^{\infty} \varepsilon_m \left[c_m^R(\zeta)\cos m(\varphi - \zeta) + d_m^R(\zeta)\sin m(\varphi - \zeta) \right], \tag{4.B1}$$

$$c_m^R(\zeta) = a_m^R \cos m\zeta + b_m^R \sin m\zeta \,, \tag{4.B2}$$

$$d_m^R(\zeta) = -a_m^R \sin m\zeta + b_m^R \cos m\zeta \,. \tag{4.B3}$$

where ε_m is 1 for $m = 1$ otherwise 2. Substituting equations (4.B1) and (4.16) into equation (4.13), we obtain

$$\begin{aligned}\phi_{ZZ}^R(r,\zeta) &= \frac{1}{2\pi}\sum_{m=0}^{\infty}\varepsilon_m \int_{-\pi}^{\pi} d\varphi \left[c_m^R(\zeta)\cos m(\varphi-\zeta) + d_m^R(\zeta)\sin m(\varphi-\zeta)\right] e^{ik^R r\cos(\varphi-\zeta)} \\ &= \frac{1}{2\pi}\sum_{m=0}^{\infty}\varepsilon_m c_m^R(\zeta)\int_{-\pi}^{\pi} d\varphi \cos m(\varphi-\zeta) e^{ik^R r\cos(\varphi-\zeta)} \\ &= \sum_{m=0}^{\infty}\varepsilon_m i^m c_m^R(\zeta) J_m\left(k^R r\right)\end{aligned}, \tag{4.B4}$$

where the $\sin m(\varphi-\zeta)$ terms in the first equation integrate to zero because of the odd function with respect to $\varphi-\zeta$. We used the integral representation of Bessel function (equation (4.29)) for the last equation in equation (4.B4). Finally, Since $c_0^R(\zeta) = a_0^R$, we obtain equation (4.39). Similarly, for ZR component of the cross spectral tensor,

$$\begin{aligned}\phi_{ZR}^R(r,\zeta) &= \frac{1}{2\pi} iH\sum_{m=0}^{\infty}\varepsilon_m \int_{-\pi}^{\pi} d\varphi \left[c_m^R(\zeta)\cos m(\varphi-\zeta) + d_m^R(\zeta)\sin m(\varphi-\zeta)\right]\cos(\varphi-\zeta) e^{ik^R r\cos(\varphi-\zeta)} \\ &= \frac{1}{2\pi} iH\sum_{m=0}^{\infty}\varepsilon_m c_m^R(\zeta)\int_{-\pi}^{\pi} d\varphi \cos m(\varphi-\zeta)\cos(\varphi-\zeta) e^{ik^R r\cos(\varphi-\zeta)}\end{aligned}. \tag{4.B5}$$

Using the addition theorem of trigonometric function, we obtain

$$\begin{aligned}\phi_{ZR}^R(r,\zeta) &= \frac{1}{2\pi} iH\sum_{m=0}^{\infty}\varepsilon_m c_m^R(\zeta)\int_{-\pi}^{\pi} d\varphi \frac{\cos(m+1)(\varphi-\zeta) + \cos(m-1)(\varphi-\zeta)}{2} e^{ik^R r\cos(\varphi-\zeta)} \\ &= iH\sum_{m=0}^{\infty}\varepsilon_m c_m^R(\zeta)\frac{i^{m+1}J_{m+1}\left(k^R r\right) + i^{m-1}J_{m-1}\left(k^R r\right)}{2} \\ &= -H\sum_{m=0}^{\infty}\varepsilon_m i^m c_m^R(\zeta)\frac{J_{m+1}\left(k^R r\right) - J_{m-1}\left(k^R r\right)}{2}\end{aligned}. \tag{4.B6}$$

For P and SV waves, the integrals over azimuth can be performed by the same way.

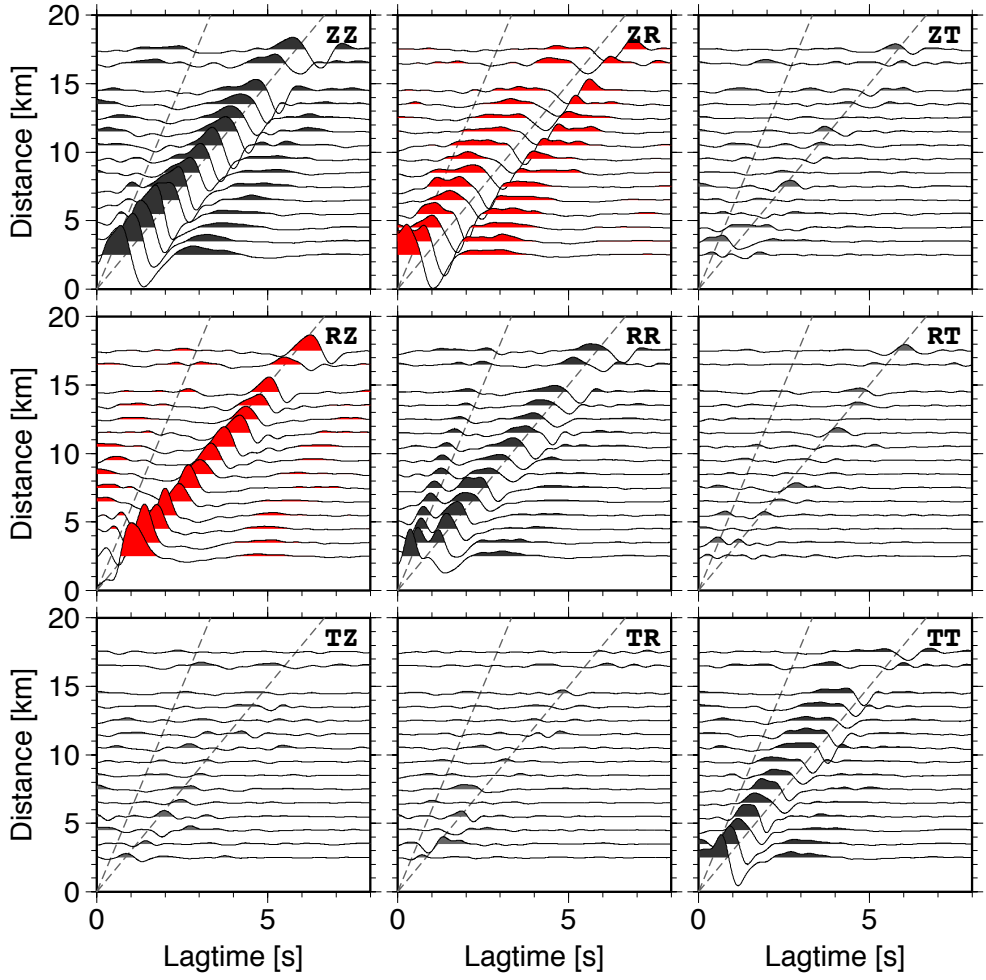

Figure 4.1. Time-symmetric component of cross-correlation tensor observed at Tono array. Cross-correlation functions are averaged over bins of every 1 km separation distance. Gray broken lines indicate the travel times of waves with propagation velocities of 6.0 km/s and 3.0 km/s.

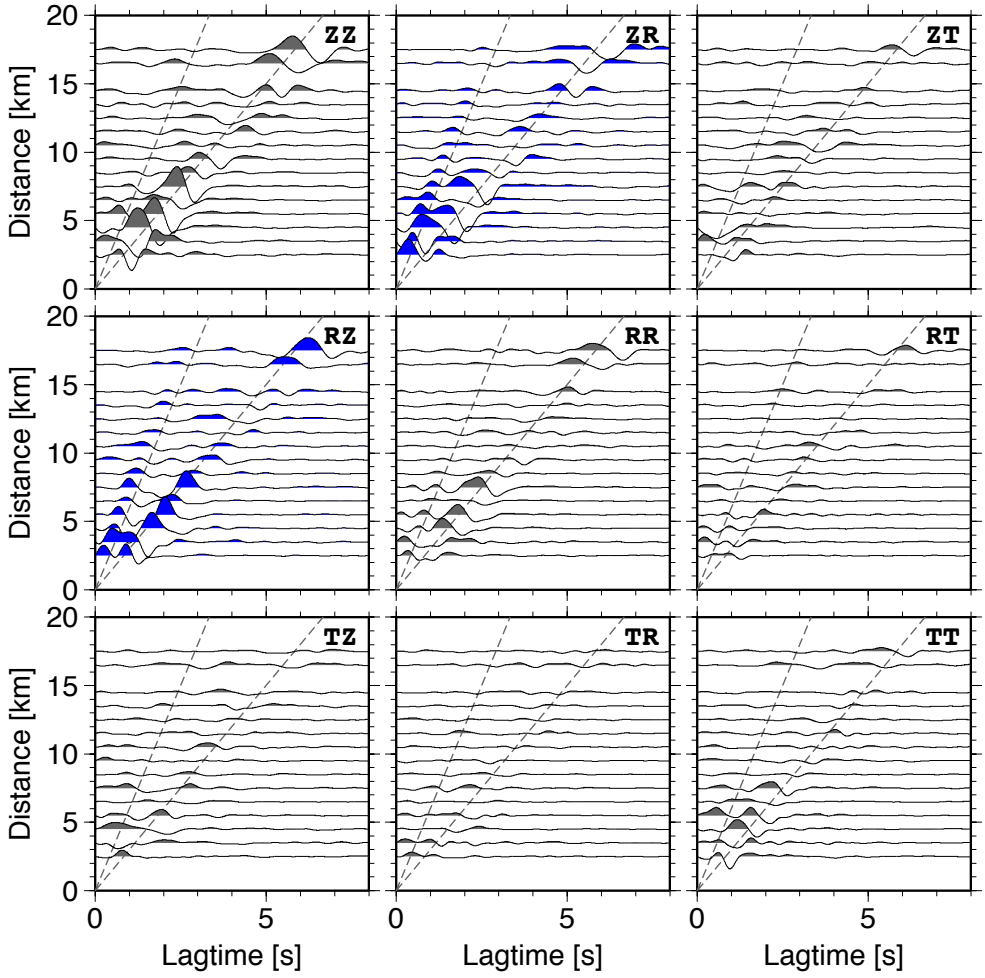

Figure 4.2. Time-antisymmetric component of cross-correlation tensor observed at Tono array. Cross-correlation functions are averaged over bins of every 1 km separation distance. Gray broken lines indicate the travel times of waves with propagation velocities of 6.0 km/s and 3.0 km/s.

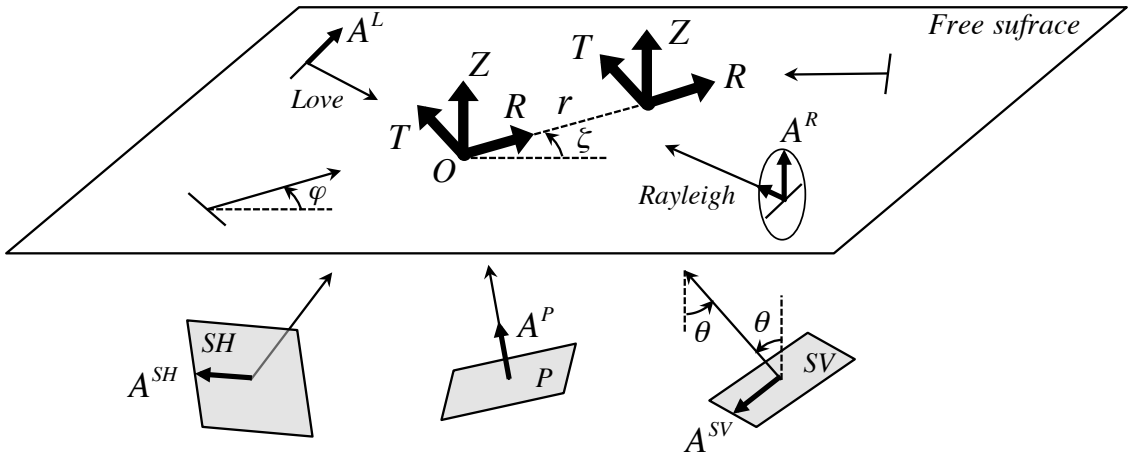

Figure 4.3. Schematic of the problem setting of formulation. Incident Rayleigh, Love, P, SV and SH waves propagate in various directions as random uncorrelated plane waves. The direction of propagation is denoted by azimuth φ and incident angle θ. Long and short arrows on plane waves show the directions of propagation and of particle motion, respectively. Vertical (Z), radial (R) and transverse (T) components for calculating cross spectra are taken as thick arrows at two stations on the free surface.

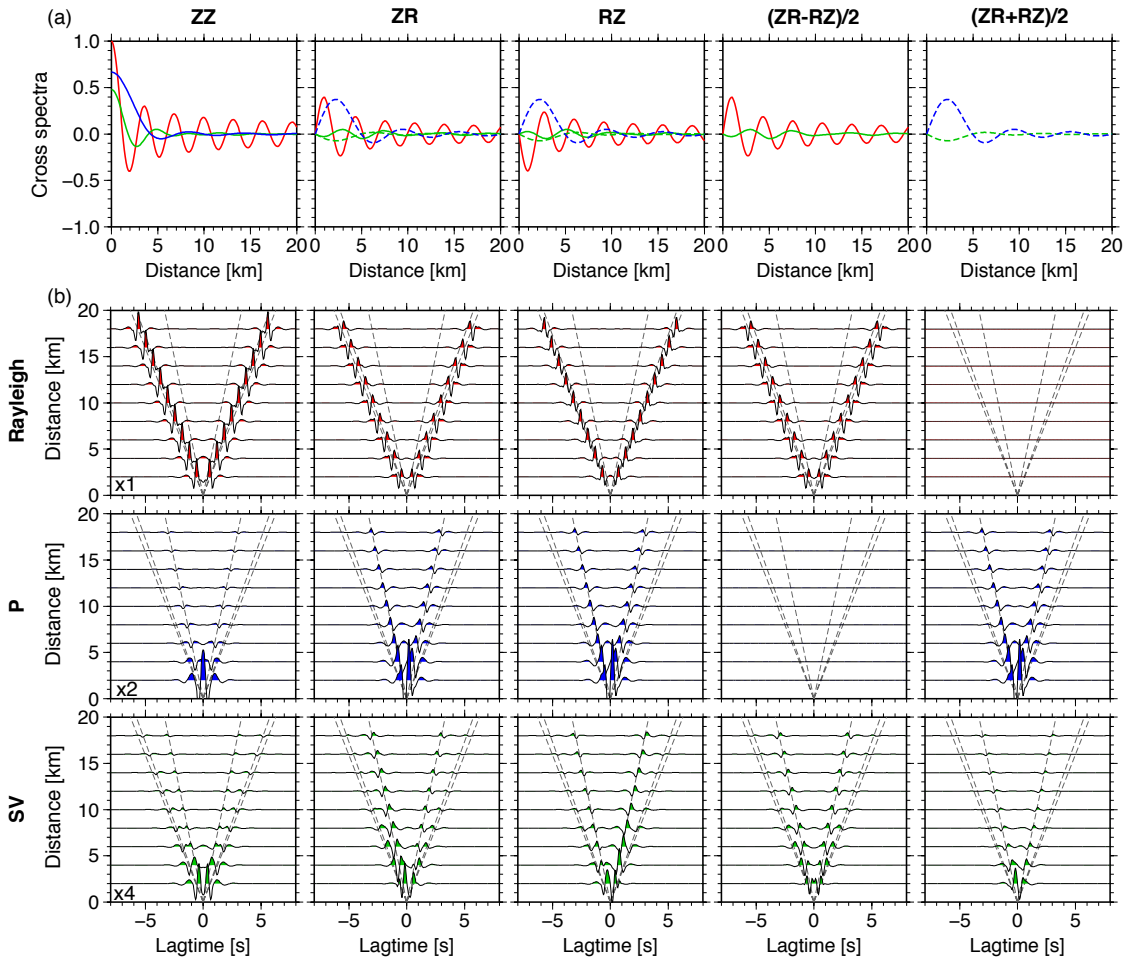

Figure 4.4. (a) Cross spectra for isotropic incidence at 1.0 Hz as a function of separation distance. From left to right, ZZ, ZR, RZ, (ZR–RZ)/2 and (ZR+RZ)/2 components are shown. Rayleigh, P and SV wave contributions are indicated by red, blue and green lines, respectively. Solid and broken lines represent real and imaginary parts of cross spectra, respectively. (b) Time domain cross-correlation functions for each components (same as (a)) aligned by separation distance. From top to bottom, Rayleigh, P and SV contributions are shown. The amplitudes of all components are corrected by multiplying *r*. In addition, the amplitude of P and SV wave contributions are exaggerated by factors of 2 and 4 as compared with the Rayleigh wave contribution. Frequency range is 1.0-2.0 Hz. Gray broken lines indicate the travel times of P (6.0 km/s), S (3.46 km/s) and Rayleigh (3.18 km/s) waves.

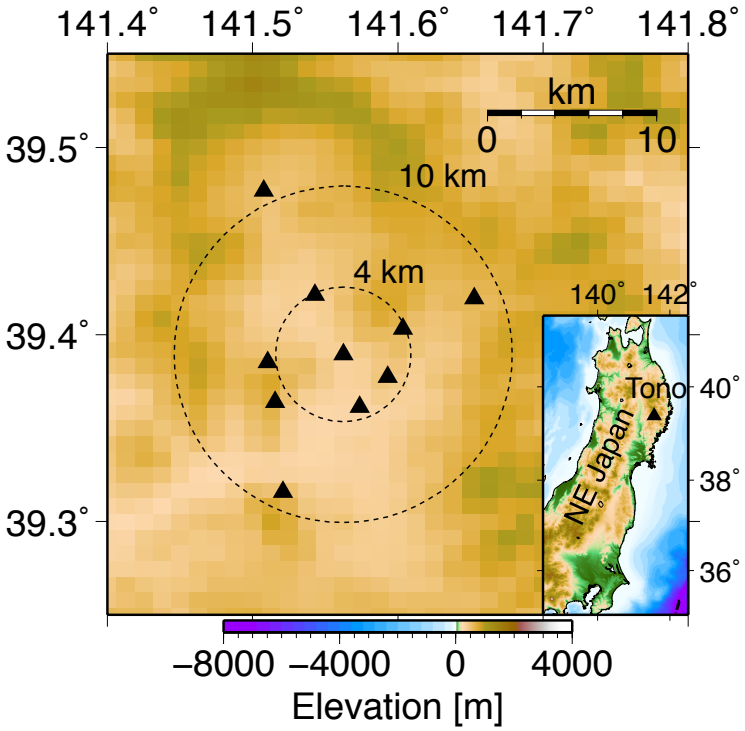

Figure 4.5. Map of Tono array. Tono array consists of 10 broadband sensors with three components (black triangles). Six stations are on a circle of about 4 km radius and three stations are on a circle of about 10 km radius around the center of the array.

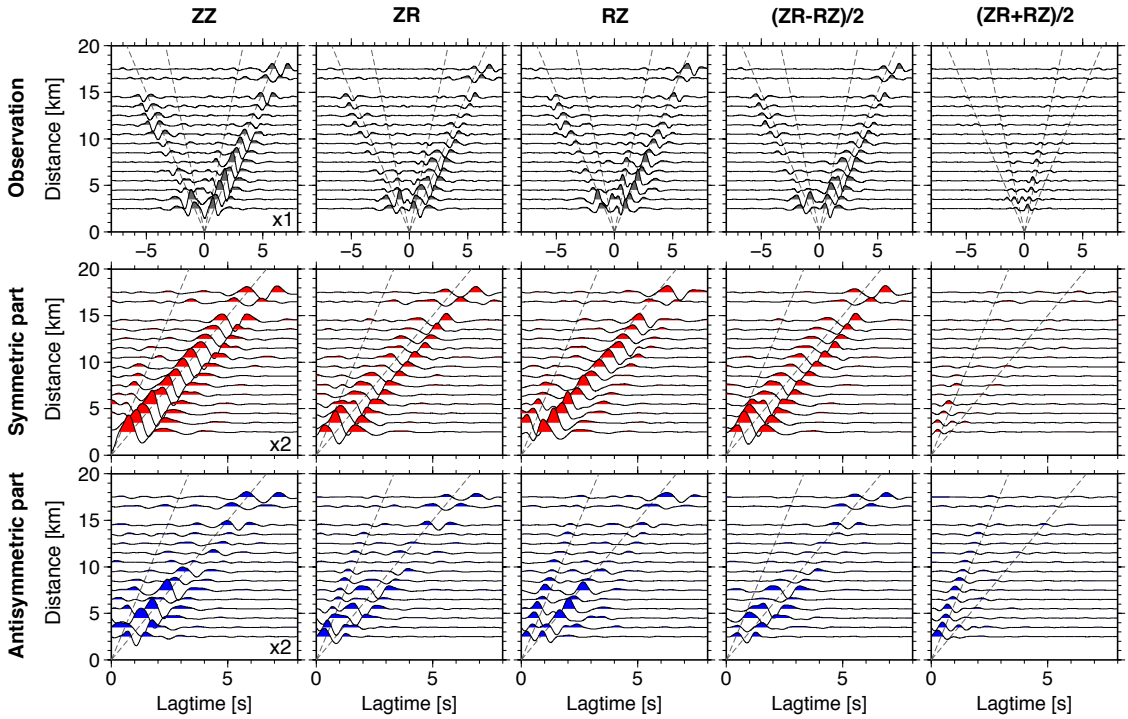

Figure 4.6. Observed cross-correlation functions at Tono array. Cross-correlation functions are averaged over every 1 km separation distance. Gray (top) shows two side cross-correlations. Red (middle) and blue (bottom) show the time-symmetric and time-antisymmetric parts of the two side correlations (gray). The amplitude of the time-symmetric and time-antisymmetric components are enlarged by a factor of 2 as compared to that of the two side correlations. Gray broken lines indicate the travel times of waves with 6.0 km/s and 3.0 km/s.

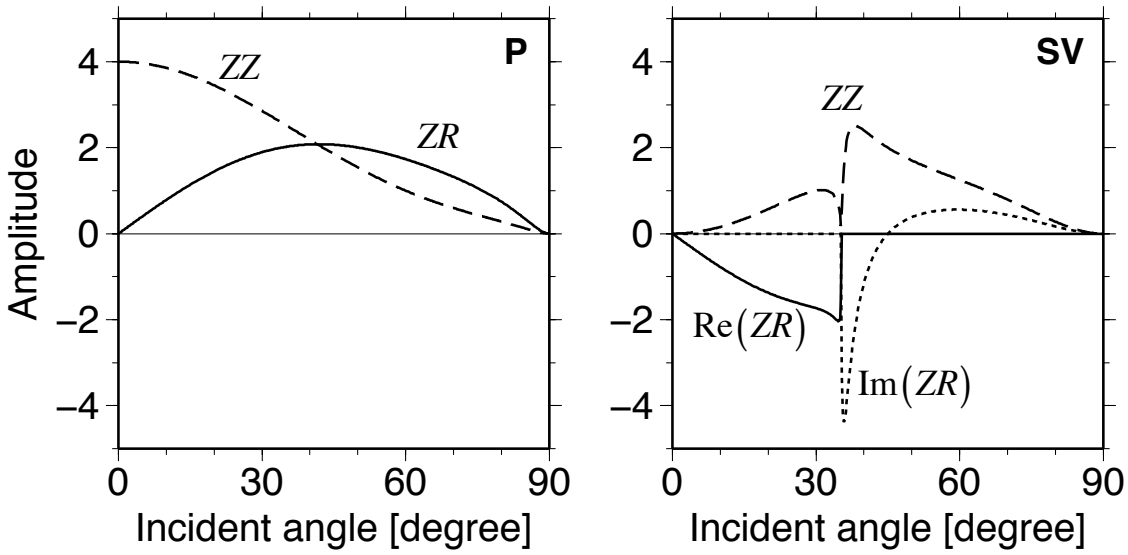

Figure 4.A1. Cross spectra between response functions with respect to incident angle. *ZZ* and *ZR* represent w^*w and w^*u, respectively. V_P/V_S is set to $\sqrt{3}$. The critical angle is approximately 35º.

5. Composition of ambient noise at Tono array

Ryota Takagi,[1] Hisashi Nakahara,[2] Toshio Kono,[1] and Tomomi Okada[1]

[1]Research Center for Prediction of Earthquakes and Volcanic Eruptions, Graduate School of Science, Tohoku University, Sendai, Japan.

[2]Department of Geophysics, Graduate School of Science, Tohoku University, Sendai, Japan.

Summary

Ambient noise methods have become common tools to explore and monitor subsurface structure. However, the effective use of ambient noise should stand on the knowledge of the nature of ambient noise. In order to reveal the composition of ambient noise quantitatively, we extend the SPAC method to the body wave incidence. Applying the extended SPAC method to the observation at Tono array, northeast Japan, we shows a good agreement between the theoretical cross spectra and the observed cross spectra. By fitting the theoretical cross spectra to the observed cross spectra, we estimated the composition ratio of Rayleigh, Love, and P waves. The characteristics of the composition ratio show a significant change at 1 Hz. While the P wave composition in total power is 5-15% and the lowest one below 1 Hz, the P wave composition suddenly increases above 1 Hz and reaches 50% and the highest one in those of three wave modes. The change at 1 Hz is attributed to attenuation of high-frequency surface waves because the decay rate of the absolute value of power spectra of surface waves gets steeper around 1 Hz as compared with the constant decay of P wave. We also examine the temporal variation of the composition of ambient noise. Whereas power spectrum of each mode shows temporal variation coincident with the offshore significant wave height, the ratio between power spectra varies little with time. The stable composition ratio suggests that all of Rayleigh, Love, and P waves have the same source and the source-receiver distance does not vary with time. Accordingly, near coastal region is possible location of the dominant source of observed ambient noise. For the application of ambient noise, we should take account of the composition of ambient noise.

5.1. Introduction

Seismometers always record background earth's vibration even when earthquakes do not occur, which is referred to as ambient noise. Ambient noise spectra have three prominent peaks at 0.002-0.02 Hz, 0.05-0.1 Hz, and 0.1-0.3 Hz, termed Earth's hum, primary microseisms, and secondary microseisms, respectively. Earth's hum and microseisms are mainly generated by ocean waves. Since ambient noise is composed of seismic waves propagating within the earth, we can investigate subsurface structure using ambient noise without earthquakes and explosions. Besides, ambient noise observed anytime and anywhere is useful to monitor subsurface structure. However, some special techniques are necessary to make use of ambient noise because ambient noise records do not have deterministic phase arrivals such as P and S arrivals in earthquake records.

Classic ambient-noise-based methods are developed for near-surface structural survey for seismic hazard assessment and for site response. The ambient noise methods are classified into multi-station array methods and single-station methods. The array methods such as the spatial auto-correlation (SPAC) method [Aki, 1957; Okada, 2003] and the frequency-wavenumber (FK) method [Capon et al., 1967; Capon, 1969; Lacoss et al., 1969; Rost and Thomas, 2002] mainly determine the dispersion curve of surface wave incident on the array coherently. As a single-station method, the horizontal-over-vertical (H/V) spectral ratio provides reliable information about site response [Nogoshi and Igarashi, 1971; Nakamura, 1989]. Recent seismic interferometry allows us to explore more deep structure [Shapiro and Campillo, 2004; Shapiro et al., 2005] and to monitor subsurface structure [e.g., Brenguier et al., 2008; Takagi et al., 2012; Hobiger et al., 2012] by cross-correlating ambient noise at two stations. In addition to the cross-correlation functions, the auto-correlation function at a single station has been applied for subsurface imaging [Ito et al., 2012; Ito and Shiomi, 2012] and monitoring [e.g., Wegler and Sens-Schönfelder, 2007; Maeda et al., 2010; Ueno et al., 2012].

These methods have a great potential to investigate subsurface structure using ambient noise. However, the effective use of ambient noise should stand on the knowledge of a nature of ambient noise. That is because we frequently make assumptions of ambient noise wavefiled to apply these methods to real data and to interpret the results obtained by these methods. For example, the SPAC method assumes predominance of one wave mode of surface waves to measure dispersion curve. There are two ways to interpret the H/V spectral ratio: body wave interpretation and Rayleigh wave interpretation. The body wave interpretation attributes the H/V spectral ratio to the resonance of S wave [Nakamura, 1989]. On the other hand, the Rayleigh wave interpretation attributes the H/V ratio to the ellipticity of Rayleigh wave [e.g., Tokimatsu et al., 1998]. Based on the theory of seismic interferometry, ambient noise wavefield must be isotropic and equilibrated to retrieve a complete Green's function [Lobkis and Weaver, 2001; Sánchez-Sesma and Campillo, 2006]. Otherwise, the cross-correlation function of ambient noise emerges as a part of Green's function such as the surface wave term of Green's function. For the auto-correlation

interferometry, the knowledge of the composition of ambient noise is more important because the auto-correlation function of ambient noise hardly discriminates extracted wavefield by itself. This is a weak point of single station methods and is also said for the H/V spectral ratio. Accordingly, for the application of ambient noise, understating of the composition of ambient noise is an important issue.

Previous studies on the composition of ambient noise mainly treat the surface-wave energy ratio between Rayleigh and Love waves. That is because the possible sources of ambient noise are ocean waves, winds, and human activity and are located on the ground surface, which suggests that seismic ambient noise consists primarily of surface waves. Based on the FK method, Friedrich et al. [1998] and Nishida et al. [2008b] reported that both Rayleigh and Love waves compose ambient noise in microseismic bands, where the energy ratio of Love to Rayleigh waves is much higher for the primary than for the secondary microseisms. At higher frequencies of 3-8 Hz, Yamamoto [2000] applied the SPAC method to horizontal-component records, showing that the relative portion of Love wave in horizontal-component ambient noise is more than 50%.

More comprehensive reviews of the composition of ambient noise have been carried out by previous studies. Nishida [2013a] focused on low-frequency ambient noise in 2-20 mHz and pointed out that the amplitudes of the toroidal modes (Love waves) are larger than those of the spheroidal modes (Rayleigh waves). Bonnefoy-Claudet et al. [2006] summarized a number of studies on the composition of ambient noise in 0.1-10 Hz, concluding that vertical-component ambient noise consists mainly of the fundamental-mode Rayleigh wave below 1.0 Hz and of a mix of body waves and fundamental and higher modes of surface waves above 1 Hz. They also mentioned that three-component array measurement, especially the SPAC method, is a key element in characterizing the seismic noise wavefield and estimating the relative proportion of each wave type and propagation mode.

Modern seismic arrays have also detected significant amount of body waves in high-frequency ambient noise in and above the frequency band of microseisms. Gerstoft et al. [2006, 2008] detected microseismic P waves in ambient noise at 0.1-0.3 Hz, which originated from distant storms. The teleseismic P waves in microseisms show seasonal variations correlating with the seasonal sea state [Koper and de Foy, 2008; Koper et al., 2009; Landès et al., 2010]. Zhang et al. [2009] also identified the regional P wave in 0.6-2.0 Hz strongly correlated with offshore local ocean wind. Koper et al. [2010] conducted a systematic analysis of the high-frequency seismic noise in 0.4-4 Hz at globally distributed 18 seismic arrays, showing a predominance of body wave components.

Accordingly, both of body and surface waves seem to compose ambient noise especially at higher frequencies in and above the microseisms. However, there remains a question how much the body and surface wave energy contribute to the ambient noise energy. The quantitative composition ratio between body and surface waves has not been clarified completely. The purpose of the present study is to revel the quantitative composition of ambient noise in a frequency range in 0.3-2.0 Hz using an array observation

at Tono, northeast Japan. In order to estimate the wave composition, we first apply the SPAC method extended to the P wave incidence [Takagi et al., 2014]. We also reveal the frequency dependence of the composition of ambient noise.

5.2. Tono Array Data

We analyzed three-component records at Tono array during one year in 2010. Figure 5.1 shows a map of Tono array. Tono array is located in the Kitakami mountain region that is characterized by granite hard rock [e.g., Iwasaki et al., 1994] and consists of 10 high sensitivity broadband sensors (STS-1 or STS-2) with the minimum and maximum separations of 2.4 km and 18 km, respectively. The sampling frequency is 100 Hz. Such small-aperture, three-component, and broadband array is useful to investigate a nature of high-frequency ambient noise.

5.2.1. Ambient Noise at Tono Array

Figure 5.2 shows the probability of vertical-component power spectra in 2010 at the central station, TU.KGL. The largest peak around 0.2 Hz corresponds to secondary microseisms generated by seafloor pressure change due to wave-wave interaction of ocean waves [Longuet-Higgins, 1950]. Here, we also show two power spectra on 17 May and on 26 September as a typical quiet day and a typical loud day, respectively. The ambient noise power of the loud day is larger than that of the quiet day by two orders of magnitude at the maximum. The strong ambient noise power is due to a typhoon on the Pacific Ocean on 26 September 2010 (http://www.jma.go.jp). In contrast, in higher frequency range above 2 Hz, the ambient noise power on the loud day is comparable as that on the quiet day. Accordingly, the dominant origin of ambient noise above 2 Hz may be not natural but cultural activity.

The difference between natural- and cultural-origin ambient noise appears in temporal variation in ambient noise. Figure 5.3 shows the temporal variations of the root-mean-square (RMS) amplitude of seismic ambient noise and the significant wave height of ocean waves in May 2010. The ocean wave data are from Nationwide Ocean Wave Information Network for Ports and Harbours (NOWPHAS, http://nowphas.mlit.go.jp). The RMS amplitude of seismic ambient noise correlates with the significant wave height of ocean waves of which periods are 6-7 s. The correlation suggests that the interaction between ocean and solid earth is the main origin of ambient noise below 2 Hz. In contrast, in a higher frequency range of 2-4 Hz, the RMS noise amplitude shows a daily variation. Therefore, the origin of ambient noise above 2 Hz is human activity. In the present study, we focus on the frequency band of 0.3-2.0 Hz.

5.2.2. Observed Cross-Correlation Tensor

The cross-correlation functions or cross spectra between two stations are useful to reveal the composition of ambient noise. We computed the cross spectra between all possible pairs of stations. First, we divided continuous records into 60-s-long records with an overlap of 30 s. Then, after removing offset, discarding segments that include earthquakes, and correcting the instrumental responses, we computed averaged cross spectra of all segments as follows:

$$\phi_{ij,\alpha\beta}(f) = \left\langle F^{*}_{i,\alpha}(f) \cdot F_{j,\beta}(f) \right\rangle. \tag{5.1}$$

Here, $F_{i,\alpha}$ denotes the Fourier spectra of αth component at *i*th station, $\langle\ \rangle$ represents the ensemble average over all segments, and * represents the complex conjugate. Note that we did not apply any normalization in both time and frequency domains. We computed cross spectra for all possible pairs of three-component records between two stations, so that we obtained the nine-component cross-spectral tensor.

Time-domain cross-correlation tensor is more intuitive to recognize retrieved wavefield. Since the power of ambient noise has significant frequency dependence as shown in Figure 5.2, the inverse Fourier transform of equation (5.1) tends to be monochromatic. Therefore, we normalized the cross-spectral tensor by the averaged power spectra of three-component records as follows:

$$\phi_{ij,\alpha\beta}(f) = \frac{\left\langle F^{*}_{i,\alpha}(f) \cdot F_{j,\beta}(f) \right\rangle}{\left\langle \left| F_i(f) \right| \right\rangle \left\langle \left| F_j(f) \right| \right\rangle}, \tag{5.2}$$

$$\left\langle \left| F_i(f) \right| \right\rangle = \sqrt{\left(\left\langle \left| F_{i,Z}(f) \right|^2 \right\rangle + \left\langle \left| F_{i,N}(f) \right|^2 \right\rangle + \left\langle \left| F_{i,E}(f) \right|^2 \right\rangle \right) / 3}. \tag{5.3}$$

where $\left\langle \left| F_{i,Z} \right|^2 \right\rangle$, $\left\langle \left| F_{i,N} \right|^2 \right\rangle$, and $\left\langle \left| F_{i,E} \right|^2 \right\rangle$ are power spectra of vertical, north-south, and east-west component at *i*th station. We obtained the time-domain cross-correlation functions by applying the inverse Fourier transform to equation (5.2).

Figure 5.4 shows the observed time-domain cross-correlation tensor in a frequency range of 0.25-2.0 Hz. Here, we averaged the cross-correlation functions within bins of 1 km separation distance. In the diagonal terms (ZZ, RR, TT) of the cross-correlation tensor, we can recognize the propagations of three wave modes: Rayleigh wave in vertical-vertical component (ZZ); Rayleigh and P waves in radial-radial component (RR); Love wave in transverse-transverse (TT) component. The apparent velocities of Rayleigh and P waves are approximately 3 km/s and 6 km/s, respectively. Love wave is a little faster than Rayleigh wave. For the cross terms ZR and RZ, Takagi et al. [2014] theoretically and observationally demonstrated that the sum and difference between ZR and RZ components separate the elliptic Rayleigh and the rectilinear P waves. Accordingly, we use ZR–RZ and ZR+RZ components instead of ZR and RZ. The observed cross-correlation tensor reveals that ambient noise mainly consists of Rayleigh, Love, and P waves.

5.3. SPAC Method Extended to Body Wave Incidence

The next step is to estimate the power of each wave mode retrieved by the cross-correlation tensor by fitting theoretical cross-spectral tensor to the observed cross-spectral tensor in frequency domain. The concept is similar to the three-component SPAC method that allows us to determine the energy partition of Rayleigh and Love waves [Chout et al., 1998; Yamamoto, 2000; Okada 2003]. However, the present study has two differences from previous studies. One is the treatment of the P wave contribution in the cross-spectral tensor. We extend the SPAC method to the case of incident P wave. The other is the use of the cross terms of cross-spectral tensor for phase velocity measurement.

5.3.1. Theoretical Cross-Spectral Tensor

First, we describe the characteristics of the theoretical cross-spectral tensor. Assuming incident Rayleigh, Love and P waves are uncorrelated [Takagi et al., 2014], we represent the cross-spectral tensor between two stations on the free surface as a superposition of the contributions from the three wave modes,

$$\Phi^{the}\left(f,r,\xi\right)=\begin{bmatrix}\phi_{ZZ}^{the} & \phi_{ZR}^{the} & \phi_{ZT}^{the}\\ \phi_{RZ}^{the} & \phi_{RR}^{the} & \phi_{RT}^{the}\\ \phi_{TZ}^{the} & \phi_{TR}^{the} & \phi_{TT}^{the}\end{bmatrix}=\Phi^{R}\left(f,r,\xi\right)+\Phi^{L}\left(f,r,\xi\right)+\Phi^{P}\left(f,r,\xi\right), \tag{5.4}$$

where $\Phi^{the}\left(f,r,\xi\right)$ is the theoretical cross-spectral tensor between two stations with a separation distance r and an azimuth ξ, and ϕ_{XY}^{the} is XY component of the cross-spectral tensor. The last three terms, $\Phi^{R}\left(f,r,\xi\right)$, $\Phi^{L}\left(f,r,\xi\right)$, and $\Phi^{P}\left(f,r,\xi\right)$, are the contributions from Rayleigh, Love, and P waves, respectively. From here, the superscripts *R*, *L* and *P* represent Rayleigh, Love and P waves, respectively. The subscripts (ZZ, ZR, ZT, ...) represent the component of the cross-spectral tensor.

In the case of isotropic wave incidence, the theoretical cross-spectral tensor are represented by relatively simple forms as follows [Haney et al., 2012; Takagi et al., 2014]:

$$\Phi^{R}\left(f,r\right)=\begin{bmatrix}a_0^R J_0\left(k^R r\right) & -Ha_0^R J_1\left(k^R r\right) & 0\\ Ha_0^R J_1\left(k^R r\right) & H^2 a_0^R\left[J_0\left(k^R r\right)-J_2\left(k^R r\right)\right]/2 & 0\\ 0 & 0 & H^2 a_0^R\left[J_0\left(k^R r\right)+J_2\left(k^R r\right)\right]/2\end{bmatrix}, \tag{5.5}$$

$$\Phi^{L}\left(f,r\right)=\begin{bmatrix}0 & 0 & 0\\ 0 & a_0^L\left[J_0\left(k^L r\right)+J_2\left(k^L r\right)\right]/2 & 0\\ 0 & 0 & a_0^L\left[J_0\left(k^L r\right)-J_2\left(k^L r\right)\right]/2\end{bmatrix}, \tag{5.6}$$

$$\Phi^P(f,r)=\begin{bmatrix} a_0^P j_{ZZ}^P\left(k^P r\right) & ia_0^P j_{ZR}^P\left(k^P r\right) & 0 \\ ia_0^P j_{ZR}^P\left(k^P r\right) & a_0^P j_{RR}^P\left(k^P r\right) & 0 \\ 0 & 0 & a_0^P j_{TT}^P\left(k^P r\right) \end{bmatrix}, \tag{5.7}$$

where a_0^R, a_0^L, and a_0^P are the incident wave power of Rayleigh, Love, and P waves, H is the horizontal-over-vertical ratio of Rayleigh wave, i is the imaginary unit, and k^R, k^L, and k^P are the wavenumbers of Rayleigh, Love, and P waves. The wavenumbers have relations as $k^R = 2\pi f/c^R$, $k^L = 2\pi f/c^L$, $k^P = 2\pi f/c^P$, where c^R, c^L, and c^P are the phase velocities of Rayleigh, Love, and P waves. J_0, J_1, and J_2 are the 0th, 1st, and 2nd order Bessel function of the 1st kind, respectively. The cross-spectral tensor of P wave (equation (5.7)) is evaluated by integrating the following equations numerically,

$$j_{ZZ}^P\left(k^P r\right)=\int_0^{\pi/2} d\theta \sin\theta\left[w^{P*}(\theta)w^P(\theta)\right]J_0\left(k^P r\sin\theta\right), \tag{5.8}$$

$$j_{ZR}^P\left(k^P r\right)=\int_0^{\pi/2} d\theta \sin\theta\left[w^{P*}(\theta)u^P(\theta)\right]J_1\left(k^P r\sin\theta\right), \tag{5.9}$$

$$j_{RR}^P\left(k^P r\right)=\int_0^{\pi/2} d\theta \sin\theta\left[u^{P*}(\theta)u^P(\theta)\right]\left[J_0\left(k^P r\sin\theta\right)-J_2\left(k^P r\sin\theta\right)\right]/2, \tag{5.10}$$

$$j_{TT}^P\left(k^P r\right)=\int_0^{\pi/2} d\theta \sin\theta\left[u^{P*}(\theta)u^P(\theta)\right]\left[J_0\left(k^P r\sin\theta\right)+J_2\left(k^P r\sin\theta\right)\right]/2, \tag{5.11}$$

where θ is the incident angle, u and w are the response functions of radial and vertical components at the free surface, respectively, which include the effect of the free surface [Takagi et al., 2014]. Note that ZR and RZ components of P wave are pure imaginary while the other components are real in equations (5.5-5.7).

Figure 5.5 shows the theoretical cross-spectral tensor at 1.0 Hz. Here, we numerically evaluated equation (5.8-5.11) according to the trapezoidal rule by intervals of 1º. The diagonal terms contain two or three wave modes. In far field where $kr >> 1$, Rayleigh wave dominates in ZZ and RR component, P wave dominates in RR component, and Love wave dominates in TT component. The dominance of P wave in RR component of the theoretical cross-spectral tensor is consistent with the dominant P waves in RR component of the observed cross-correlation tensor. Meanwhile, in near field where $kr << 1$, the amplitude of Rayleigh wave in TT component, Love wave in RR component, and P wave in ZZ and TT components are comparable to those in the other dominated components. In particular to $r = 0$, Rayleigh and Love waves have the same amplitude, a half of the incident wave power, in RR and TT components. That is reasonable because the direction of radial and transverse cannot be defined at $r = 0$. In contrast to the diagonal terms, the cross terms have only one wave modes. The simplicity makes the cross terms useful to measure the phase velocities of Rayleigh and P waves.

5.3.2. Fitting the Theoretical Cross-Spectral Tensor to the Observed Cross-Spectral Tensor

Next, we describe the procedure to fit the theoretical cross-spectral tensor to the observed cross-spectral tensor. Here, we have seven unknown parameters in equations (5.5-5.7); three of the phase velocity (c^R , c^L , c^P), three of the incident wave power (a_0^R , a_0^L , a_0^P), and one of the horizontal-over-vertical ratio of Rayleigh wave (H). Table 1 summarizes the unknown parameters to be solved. Here, for simplicity of measurement procedure, we determine a_0^R , Ha_0^R , and $H^2 a_0^R$ independently instead of a_0^R and H . In order to estimate these unknown parameters, we developed a three-step inversion. The first and second step mainly focus on the phase velocity measurement using the cross terms of the cross-spectral tensor, and the third step mainly focuses on the incident power measurement using the diagonal terms of the cross-spectral tensor. In each step, we applied a similar approach to previous studies [Nishida et al., 2008a; Takeo et al., 2013]. Note that we used the cross spectra of equation (5.1) instead of the normalized cross spectra of equation (5.2) because we discuss the absolute power of each wave mode, not only their relative ratio.

First, using the real part of the ZR–RZ component, $\phi_{ZR-RZ} = \left(\phi_{ZR} - \phi_{RZ}\right)/2$, we estimate the phase velocity of Rayleigh wave c^R and the incident power Ha_0^R . We defined the normalized misfit functions,

$$S_{ZR-RZ}\left(Ha_0^R, c^R; f\right) = \frac{\sum_{\alpha}^{N_{pair}} \left| \mathrm{Re}\left[\phi_{\alpha,ZR-RZ}^{obs}(f)\right] - \mathrm{Re}\left[\phi_{ZR-RZ}^{the}\left(Ha_0^R, c^R; f, r_\alpha\right)\right] \right|^2}{\sum_{\alpha}^{N_{pair}} \left| \mathrm{Re}\left[\phi_{\alpha,ZR-RZ}^{obs}(f)\right] \right|^2}, \tag{5.12}$$

$$\phi_{ZR-RZ}^{the}\left(Ha_0^R, c^R; f, r_\alpha\right) = Ha_0^R J_1\left(\frac{2\pi f}{c^R} r_\alpha\right), \tag{5.13}$$

where $\phi_{\alpha,ZR-RZ}^{obs}$ is the observed cross spectra of ZR–RZ component of α th station pair and ϕ_{ZR-RZ}^{the} is the theoretical cross spectra with known parameters, f and r_α , and unknown parameters, Ha_0^R and c^R . Here, Re means real part, r_α is the separation distance of α th station pair, and N_{pair} is the number of station pairs. In order to minimize equation (5.12), we performed a grid search for the phase velocity c^R and the linear least squares for the incident wave power Ha_0^R . Figure 5.6(a) shows that the theoretical cross spectra well explain the observed cross spectra. Figure 5.6(c) depicts the normalized misfit function (5.12) with respect to frequency and the phase velocity. By tracking the minimum value at each frequency point, we obtain the dispersion curve of phase velocity. However, in order to stabilize the phase velocity measurement of Rayleigh wave, we determined a smoothed dispersion curve by minimizing

$$\overline{S}_{ZR-RZ}\left(c^R;f\right)=\sum_{\Delta f}S_{ZR-RZ}\left(Ha_0^R,c^R;f+\Delta f\right), \tag{5.14}$$

where $S_{ZR-RZ}\left(Ha_0^R,c^R;f\right)$ is minimized at each grid point of phase velocity. In equation (5.14), Δf indicates the frequency band of the smoothing and satisfies $-0.12\le\Delta f\le 0.12$, where the bandwidth is 0.256 Hz and 21 frequency points. After determining the phase velocity from equation (5.14), we again estimated the incident wave power by minimizing equation (5.12) using the determined phase velocity. We estimated the measurement errors of the phase velocity and the incident wave power by a jackknife method. We performed the above procedure for N_{pair} data set of which one station pair is deleted and calculated the average and the jackknife variance of the phase velocities and the incident wave powers. For the incident power, we finally applied an additional smoothing of five-frequency-point (0.06 Hz) moving average.

Second, using the imaginary part of the ZR+RZ components, $\phi_{ZR+RZ}=\left(\phi_{ZR}+\phi_{RZ}\right)/2$, we estimate the phase velocity of P wave c^P and the incident power a_0^P. We again defined the normalized misfit function as follows:

$$S_{ZR+RZ}\left(a_0^P,c^P;f\right)=\frac{\sum_{\alpha}^{N_{pair}}\left|\mathrm{Im}\left[\phi_{\alpha,ZR+RZ}^{obs}\left(f\right)\right]-\mathrm{Im}\left[\phi_{ZR+RZ}^{the}\left(a_0^P,c^P;f,r_\alpha\right)\right]\right|^2}{\sum_{\alpha}^{N_{pair}}\left|\mathrm{Im}\left[\phi_{\alpha,ZR+RZ}^{obs}\left(f\right)\right]\right|^2}, \tag{5.15}$$

$$\phi_{ZR+RZ}^{the}\left(a_0^P,c^P;f,r_\alpha\right)=ia_0^Pj_{ZR}^P\left(\frac{2\pi f}{c^P}r_\alpha\right), \tag{5.16}$$

where Im means imaginary part, i is the imaginary unit. For computing j_{ZR}^P, we assumed the P-to-S velocity ratio as $V_P/V_P=\sqrt{3}$. Figure 5.6(b) and 5.6(d) show an example of the fitting and the normalized misfit function. The theoretical cross spectra explain the observed cross spectra well and a clear P wave signal around 5.5 km/s can be identified at 1-2 Hz. In low frequencies below 0.8 Hz, the phase velocity is not well resolved. However, since P wave velocity dose not show a dispersion feature generally, we determined P wave velocity to be 5.5 km/s for all frequencies.

Third, using the real part of the diagonal terms (ϕ_{ZZ}, ϕ_{RR}, and ϕ_{TT}) and the determined phase velocities (c^R and c^P) in the first and second steps, we estimate the incident wave power, a_0^R, $H^2a_0^R$, a_0^L, and a_0^P, and the phase velocity, c^L. Here, we again performed the same approach as the first step for the ZR–RZ component. We estimated the incident wave powers by minimizing the following misfit function,

$$S_{diag}\left(a_0^R, H^2 a_0^R, a_0^P, a_0^L, c^L; f\right) = \frac{1}{L(f)}\left\{\sum_j^{N_{pair}}\left[\left|\mathrm{Re}\left[\phi_{j,ZZ}^{obs}(f)\right] - \mathrm{Re}\left[\phi_{ZZ}^{the}\left(a_0^R, a_0^P; f, r_j, c^R, c^P\right)\right]\right|^2\right]\right.$$
$$+\sum_j^{N_{pair}}\left[\left|\mathrm{Re}\left[\phi_{j,RR}^{obs}(f)\right] - \mathrm{Re}\left[\phi_{RR}^{the}\left(H^2 a_0^R, a_0^P, a_0^L, c^L; f, r_j, c^R, c^P\right)\right]\right|^2\right], \quad (5.17)$$
$$\left.+\sum_j^{N_{pair}}\left[\left|\mathrm{Re}\left[\phi_{j,TT}^{obs}(f)\right] - \mathrm{Re}\left[\phi_{TT}^{the}\left(H^2 a_0^R, a_0^P, a_0^L, c^L; f, r_j, c^R, c^P\right)\right]\right|^2\right]\right\}$$

$$L(f) = \sum_j^{N_{pair}}\left[\left|\mathrm{Re}\left[\phi_{j,ZZ}^{obs}(f)\right]\right|^2 + \left|\mathrm{Re}\left[\phi_{j,RR}^{obs}(f)\right]\right|^2 + \left|\mathrm{Re}\left[\phi_{j,TT}^{obs}(f)\right]\right|^2\right], \quad (5.18)$$

where the theoretical cross spectra are represented by a superposition of Rayleigh, Love, and P waves as

$$\phi_{ZZ}^{the}(f, r_\alpha) = a_0^R J_0\left(\frac{2\pi f}{c^R} r_\alpha\right) + a_0^P j_{ZZ}^P\left(\frac{2\pi f}{c^P} r_\alpha\right), \quad (5.19)$$

$$\phi_{RR}^{the}(f, r_\alpha) = \frac{H^2 a_0^R}{2}\left[J_0\left(\frac{2\pi f}{c^R} r_\alpha\right) - J_2\left(\frac{2\pi f}{c^R} r_\alpha\right)\right] + \frac{a_0^L}{2}\left[J_0\left(\frac{2\pi f}{c^L} r_\alpha\right) + J_2\left(\frac{2\pi f}{c^L} r_\alpha\right)\right] + a_0^P j_{RR}^P\left(\frac{2\pi f}{c^P} r_\alpha\right), \quad (5.20)$$

$$\phi_{TT}^{the}(f, r_\alpha) = \frac{H^2 a_0^R}{2}\left[J_0\left(\frac{2\pi f}{c^R} r_\alpha\right) + J_2\left(\frac{2\pi f}{c^R} r_\alpha\right)\right] + \frac{a_0^L}{2}\left[J_0\left(\frac{2\pi f}{c^L} r_\alpha\right) - J_2\left(\frac{2\pi f}{c^L} r_\alpha\right)\right] + a_0^P j_{TT}^P\left(\frac{2\pi f}{c^P} r_\alpha\right). \quad (5.21)$$

The smoothed dispersion curve of phase velocity of Love wave c^L is determined by minimizing

$$\overline{S}_{diag}\left(c^L; f\right) = \sum_{\Delta f} S_{diag}\left(a_0^R, H^2 a_0^R, a_0^P, a_0^L, c^L; f + \Delta f\right), \quad (5.22)$$

where the band width is the same as Rayleigh wave and 0.256 Hz. The measurement errors are estimated by the jackknife method. Figure 5.7 shows examples of the fitting between the observed and theoretical cross spectra at 0.7 Hz, 1.0 Hz, and 1.4 Hz. At 0.7 Hz, one wave mode of surface wave almost explains the observed cross spectra in each component: Rayleigh wave in ZZ and RR components; Love wave in TT components. In contrast, at higher frequency of 1.0 Hz and 1.4 Hz, the contributions of other wave modes get obvious. In particular to RR component, the long-wavelength P wave strongly contributes to the cross spectra in addition to the short-wavelength Rayleigh wave. As shown in Figure 5.7, the extended SPAC method shows a good agreement between the theoretical and observed cross-spectral tensor.

In the present study, we assumed isotropic wave incidences of Rayleigh, Love, and P waves. This assumption may be critical if we use only one station pair. However, since we used all station pairs in various azimuths simultaneously, the bias of anisotropic incidence may be averaged and reduced. In addition, we used only real part of ZR–RZ, ZZ, RR, and TT components and used only imaginary part of ZR+RZ component, which corresponds to the time-symmetric part and the time-antisymmetric part of cross-correlation functions, respectively. The use of the time-symmetric or time-antisymmetric parts results in the removal of odd order terms of the Fourier series and spherical harmonics representing the distributions of anisotropic wave incidence [Weaver et al., 2009; Takagi et al., 2014]. Although the bias

due to the anisotropy in azimuthal direction is relieved by the above reason, the bias due to anisotropy in incident angle still remains. That is because seismic stations are on a plane of the free surface regardless of the three-dimensional body wave. As an analogy of a circular array in the ordinary SPAC method [Aki 1957], a spherical or hemi-spherical array is necessary to cancel out anisotropy of incident body wave. However, the fitting shows a good agreement between the theoretical and observed cross spectra. Therefore, in this case, we consider that the assumption will not give a critical bias for measurement of incident wave power. Otherwise, Harmon et al. [2010] took account of the anisotropic wave incidence of scalar wave using a spherical harmonics expansion [Cox, 1973]. In the case of vector wave, the similar approach is possible using the theoretical cross spectra for anisotropic incidence [Takagi et al., 2014]. These procedures will also allow us to investigate noise source distribution and may be a subject of our future study.

5.4. Composition of Ambient Noise

5.4.1. Annual Average in 2010

Once we obtain the incident wave power of each mode, we can compute the power spectrum of each wave mode using equation (5.5-5.7) by setting $r = 0$ as follows:

$$\begin{cases} p_V^R(f) = \phi_{ZZ}^R(f,0) = a_0^R \\ p_V^P(f) = \phi_{ZZ}^P(f,0) = a_0^P j_{ZZ}^P(0) \end{cases}, \tag{5.23}$$

$$\begin{cases} p_H^R(f) = \phi_{RR}^R(f,0) = \phi_{TT}^R(f,0) = H^2 a_0^R/2 \\ p_H^L(f) = \phi_{RR}^L(f,0) = \phi_{TT}^L(f,0) = a_0^L/2 \\ p_H^P(f) = \phi_{RR}^P(f,0) = \phi_{TT}^P(f,0) = a_0^P j_{RR}^P(0) \end{cases}, \tag{5.24}$$

where p_V^R and p_V^P are the vertical-component power spectra of Rayleigh and P waves, and p_H^R, p_H^L and p_H^P are the horizontal-component power spectra of Rayleigh, Love, and P waves. The constant $j_{ZZ}^P(0)$ and $j_{RR}^P(0)$ are related to the reflection coefficient at the free surface and satisfy $j_{ZZ}^P(0) = 1.33$ and $j_{RR}^P(0) = 1.00$ for $V_P/V_S = \sqrt{3}$.

Figure 5.8 shows the ratio of the power spectra estimated from annually averaged cross spectra in 2010. The most important result of the present study is the significant change of the P-to-Rayleigh ratio at 1.0 Hz. At low frequencies below 1.0 Hz, the P-to-Rayleigh ratios are in low level: 0.05-0.15 in vertical component and 0.16-0.46 in horizontal component. In contrast, above 1 Hz, the P-to-Rayleigh ratios suddenly increase and have the maximum value at 1.5 Hz. The maximum value is 0.87 in vertical component and 2.77 in horizontal component. In contrast, the change in Love-to-Rayleigh ratio at 1.0 Hz is less significant. The Love-to-Rayleigh ratio in horizontal component is in a range of 0.74-1.98 in 0.3-2.0 Hz.

The difference between vertical and horizontal components is from the horizontal-over-vertical ratio of Rayleigh wave, H. Using Ha_0^R estimated from the ZR–RZ component and a_0^R and $H^2a_0^R$ estimated from the diagonal terms, we shows the horizontal-over-vertical ratio including its sign in Figure 5.8(b). The three estimates of $H^2a_0^R/a_0^R$, Ha_0^R/a_0^R, and $H^2a_0^R/Ha_0^R$ are roughly consistent with each other. H is negative and approximately –0.7 at all frequencies. Since a negative value of H indicates a retrograde particle motion [Takagi et al., 2014], the extracted Rayleigh wave can be identified as the fundamental mode. In addition, –0.7 is a reasonable value of H of the fundamental-mode Rayleigh wave in a homogeneous half space with $V_P/V_S=\sqrt{3}$, which is –0.68. As usual particle motion plots using ZZ and ZR components in time domain, the present SPAC analysis in frequency domain also gives the information of the ellipticity and the direction of the particle motion.

Another representation of our results is the composition ratio of ambient noise. Here, the composition ratios are defined by the normalized power spectra as follows:

$$q_V^R=\frac{p_V^R}{p_V^P+p_V^R},\quad q_V^P=\frac{p_V^P}{p_V^P+p_V^R}, \tag{5.25}$$

$$q_H^R=\frac{p_H^R}{p_H^P+p_H^R+p_H^L},\quad q_H^L=\frac{p_H^P}{p_H^P+p_H^R+p_H^P},\quad q_H^P=\frac{p_H^P}{p_H^P+p_H^R+p_H^P}, \tag{5.26}$$

where q_V^R and q_V^P are the composition ratio of Rayleigh and P waves in vertical component, and q_H^R, q_H^L and q_H^P are the composition ratio of Rayleigh, Love, and P waves in horizontal component. Since Rayleigh and P waves have horizontal component while Love wave have only horizontal component, we also estimate the composition ratio of the three-component total power as follows:

$$p_T^P=p_V^P+2p_H^P,\quad p_T^R=p_V^R+2p_H^R,\quad p_T^L=2p_H^L, \tag{5.27}$$

$$q_T^P=\frac{p_T^P}{p_T^P+p_T^R+p_T^P},\quad q_T^R=\frac{p_T^R}{p_T^P+p_T^R+p_T^L},\quad q_T^L=\frac{p_T^P}{p_T^P+p_T^R+p_T^P}, \tag{5.28}$$

where p_T^R, p_T^L and p_T^P are the total power spectra of Rayleigh, Love, and P waves, and q_T^R, q_T^L and q_T^P are the composition ratio of the total powers of Rayleigh, Love, and P waves. Figure 5.9 shows the composition ratio in each component. Again, the most obvious feature is the increases of P wave composition above 1 Hz. In total power, while the P wave composition is 5-15% and the lowest one in the three wave modes blew 1 Hz, the increase leads the P wave to the highest one with the composition up to 50%. In horizontal component, Love wave composition is comparable or a little larger than Rayleigh wave composition, which is consistent with previous studies [Bonnefoy-Claudet et al., 2006].

5.4.2. Temporal Variation in 2010

Temporal variation of the composition is a next interest because the temporal variation helps to consider noise source and is an important issue for subsurface monitoring using ambient noise. Figure 5.10(a) shows the long-term temporal variations in the horizontal-component power spectra of Rayleigh,

Love, and P waves at 0.3, 0.7, and 1.4 Hz. We estimated the power spectra from the 30-day-averaged cross spectra with an overlap of 15 days. The power spectrum of each wave mode shows clear seasonal variations at all frequencies: low amplitude in summer from the beginning of June to the end of August and high amplitude in winter. The similar seasonal variation is also shown in the significant wave height of ocean wave of which period is 6-7 s (Figure 5.10(c) and 5.10(d)), where the 20-minite-sampled significant wave height is averaged within the same time windows as seismic data. Figure 5.10(b) shows the relationship between the P and Love wave power and the Rayleigh wave power in horizontal component. The P and Love wave power distribute on slopes indicating the annually averaged power spectral ratio shown in Figure 5.8. Therefore, in contrast to the clear variations in power spectra, the ratio between other wave modes is stable in time.

Figure 5.11 shows the short-term variations in the power spectra and in the significant wave height in May 2010, which are estimated from daily-averaged cross spectra and from daily-averaged significant wave height, respectively. The temporal variations in the power spectra coincide with that in the significant wave height. Figure 5.11(d) shows a clear correlation between the vertical-component power spectra of Rayleigh wave and the significant wave height, suggesting that the power spectrum of Rayleigh wave is proportional to the 4th power of the wave height. As the long-term variation, the composition ratios depend little on time. Such temporally stable composition ratio has been reported in lower frequencies of 0.01-0.25 Hz [Nishida et al., 2008b] although the previous study focused on the ratio only between Rayleigh and Love waves.

5.5. Discussion

We revealed the composition ratio of ambient noise in a frequency range of 0.3-2.0 Hz quantitatively. Our results shows that the composition significantly changes at 1.0 Hz: the relative composition of P wave suddenly increase above 1 Hz. Nishida et al. [2008b] investigated the energy ratio between Rayleigh and Love waves in lower-frequency ambient noise in 0.01-0.25 Hz using Hi-net tiltmeter records in Japan. Nishida et al. [2008b] concluded that 0.1 Hz is a boundary of the energy ratio between Rayleigh and Love waves: the relative compositions of Love wave suddenly increase below 0.1 Hz. From the results of the present study and of Nishida et al. [2008b], we summarized the dominant wave mode of ambient noise in Table 2. As shown in Table2, we reached a conclusion that 0.1 and 1 Hz are the boundary frequencies of the composition of ambient noise at Tono array.

There are two factors changing the composition of ambient noise: source mechanism and path effect. The boundary frequency of 0.1 Hz is attributed to the difference in source mechanisms of primary microseisms and secondary microseisms [Friedrich et al., 1998; Nishida et al., 2008b]. Primary microseisms have the same frequency (0.05-0.1 Hz) as the ocean wave and thus are also termed single-frequency microseisms. The coincidence of the typical frequency of seismic and ocean waves

suggests a linear coupling between ocean wave and solid earth. The interaction between ocean wave and the sea-bottom topography produces the horizontal shear traction, which excites both of Rayleigh and Love waves [Fukao et al., 2010; Saito, 2010].

On the other hand, secondary microseisms are observed at twice the frequency of the ocean waves and thus are also termed double-frequency microseisms. The double-frequency microseisms have been explained by the theory of Longuet-Higgins [1950]. The interaction of oppositely propagating ocean waves generates a pressure oscillation at twice the wave frequency. The pressure oscillation produces the normal traction on seafloor, which excites Rayleigh wave without Love wave. Because of the nonlinearity, the amplitude of the pressure oscillation is proportional to the product of the amplitudes of the oppositely propagating waves. Accordingly, the power spectrum of seismic wave is expected to be proportional to the 4th power of the ocean wave height. Figure 5.11(d) shows that the power spectrum of Rayleigh wave is proportional to the 4th power of the significant wave height, supporting the seismic wave excitation due to the nonlinear wave-wave interaction.

The other boundary frequency of 1 Hz, which is observed by the present study, can be attributed to the path effect. Figure 5.12 shows the absolute power spectra of Rayleigh, Love, and P waves. Whereas P waves decays with an almost constant rate as frequency increases, the decay rates of Rayleigh and Love waves get steeper around 1 Hz. The change in the decay rates of surface waves results in the increase of the relative composition of P wave. The steeper decay of high-frequency surface waves may be caused by attenuation within the propagation from the noise sources to the seismic array. That is because high-frequency surface waves have a large sensitivity in shallow subsurface layer characterized by high attenuation. In addition, the less significant change of the composition ratio between Love and Rayleigh waves at 1 Hz suggests that the excitation mechanism does change at 1 Hz. The variation in Love-to-Rayleigh composition may be due to difference of the characteristics of the attenuation between Rayleigh and Love waves.

Such path effect should depend on the source-receiver distance and site condition. Using an array at Parkfield in California, Zhan et al. [2009] also showed the predominance of P wave in high-frequency ambient noise above 0.6 Hz. The difference between 0.6 Hz of Zhan et al. [2009] and 1 Hz of the present study is possibly due to both of the source-receiver distance and site condition. Tono array is located on granite hard rock in Kitakami mountain region and is only 30 km away from the Pacific coast. Consequently, the high-frequency surface waves propagate from source to Tono array efficiently, increasing the boundary frequency.

Temporal variation of the composition helps to consider the possible source region. Whereas the power spectra of each wave modes shows temporal variations coincident with ocean wave activity, the ratio of power spectra is stable in time. The time independent composition ratio suggests that the all of Rayleigh, Love, and P waves have the same origin and the source-station distance depends little on time.

Near coastal regions are feasible to satisfy such situation. The correlation between the power spectra and the significant wave height of 20 km off the Pacific coast supports the near coastal origin of ambient noise. While many modern seismic arrays have detected teleseismic P wave generaged by distant storms [e.g., Gerstoft et al., 2008], Zhang et al. [2009] has identified the P wave propagation in a regional scale at Parkfield. Koper et al. [2010] also identified the local or regional P wave phase termed Pn and Pg waves at two seismic array at Finnmark, Norway, and at Petropavlovsky-Kamchatskiy, Kamchatka. The common point of the seismic arrays that detect the local or regional P waves is the near coastal location: Tono is 30 km, Parkfield is 70 km, Finnmark is 100 km, Petropavlovsky-Kamchatskiy is 70 km away from the nearest coast approximately. Therefore, the near coastal ocean activity generate the regional and local P waves, which are commonly detected by nearby seismic array.

The present study did not detect S wave propagation. There might be two reasons of the absence of S waves. One is due to the limitation of horizontally separated small array. Because of the slow propagation velocity of S wave close to those of surface waves, S waves do not separate from surface waves in short separation distance, which may limit the identification of S waves. The other is due to the source mechanism because the pressure source due to the nonlinear wave-wave interaction primarily generates Rayleigh and P waves. However, the pressure source cannot explain the observed Love waves with composition comparable to Rayleigh wave in horizontal component. Further studies are needed to address the issue.

The present study shows the significant amount of body wave in ambient noise and its significant frequency dependence. Therefore, unless considering the body wave components, we may fail in correct interpretation of the H/V spectral ratio and the auto-correlation functions and in robust measurement of phase velocity of surface wave by the SPAC method. For subsurface monitoring, the temporal stability of the ambient noise composition is good news. However, we should pay attention to the composition to interpret the obtained temporal variation correctly.

5.6. Conclusions

We revealed the composition ratio of ambient noise quantitatively in a frequency range of 0.3-2.0 Hz by applying the extended SPAC method to Tono array data. The extended the SPAC method involves the P wave incidence in addition to two surface waves, Rayleigh and Love waves, showing a good agreement between the theoretical cross spectra and the observed cross spectra. The characteristics of the obtained composition of ambient noise significantly change at 1 Hz. Below 1 Hz, P wave has the smallest composition of 5-15% in total energy. In contrast, above 1 Hz, the composition of P wave suddenly increases and becomes the largest one with the composition ratio of 50%. Aggregating the previous study on ambient noise composition conducted with Japanese data [Nishida et al., 2008b], we can summarize that 0.1 Hz and 1 Hz are the boundary frequencies of the composition of ambient noise at Tono array.

While the 0.1 Hz boundary is attributed to change in source mechanism between primary and secondary microseisms, the 1 Hz boundary is due to path effect. Attenuation of high-frequency surface waves results in the increase of P wave composition. We also examined the temporal change in the composition of ambient noise. Whereas the power spectrum of each wave mode shows long-term and short-term variations coincident with the significant wave height of offshore ocean waves, the ratio of the power spectra depends little on time. The fact suggests that all of Rayleigh, Love, and P waves have the same origin and the source-station distance varies little with time. Accordingly, near coastal region is the possible source area. The local or regional P waves generated by near coastal ocean waves are a common feature of high-frequency ambient noise at land seismic stations near coasts. Background seismic noise has emerged into the foreground owing to developments of various ambient-noise-base methods to explore subsurface structure. In order to make effective uses of ambient noise, we also should understand the nature of ambient noise.

Table 1. Unknown Parameters to Be Solved

Component	Unknown parameters		
	Rayleigh	Love	P
ZZ	a_0^R, c^R		a_0^P, c^P
RR	$H^2 a_0^R$, c^R	a_0^L, c^L	a_0^P, c^P
TT	$H^2 a_0^R$, c^R	a_0^L, c^L	a_0^P, c^P
ZR–RZ	Ha_0^R, c^R		
ZR+RZ			a_0^P, c^P

Table 2. Dominant Wave Mode in Ambient Noise at Tono Array[a]

Frequency	Dominant wave mode			Mechanisms (ocean wave)
	Vertical	Horizontal	Total	
< 0.1 Hz	Rayleigh	Love	Rayleigh ~ Love	Shear traction (topographic coupling)[b]
0.1-1 Hz	Rayleigh	Rayleigh ~ Love	Rayleigh	Pressure source (wave-wave interaction) [c]
1 Hz <	Rayleigh ~ P	P	Rayleigh ~ P	Pressure source (wave-wave interaction) [d]

[a]The summary is a compile of results obtained by Nishida et al. [2008] and this study.

[b]Nishida et al. [2008], Fukao et al. [2010], Saito [2010]

[c]Longuet-Higgins [1950]

[d]Attenuation of high-frequency surface waves results in the dominance of P wave.

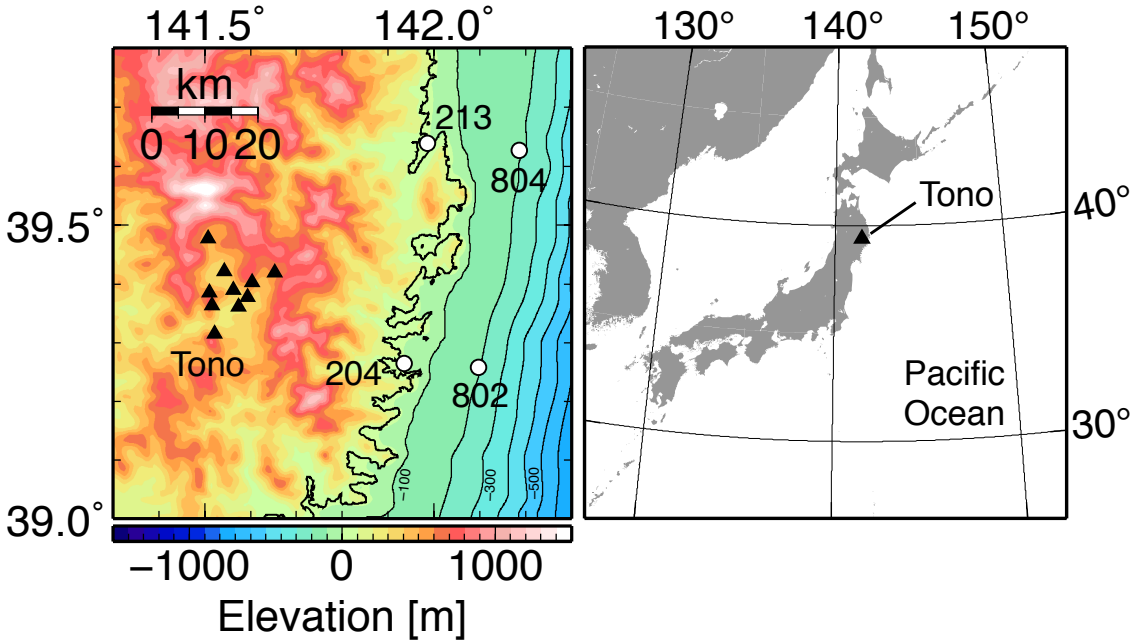

Figure 5.1. Map of Tono array (black triangles) and NOWPHAS stations and buoys (open circles). Contour in left map indicates elevation from –100 to –700 m by intervals of 100 m.

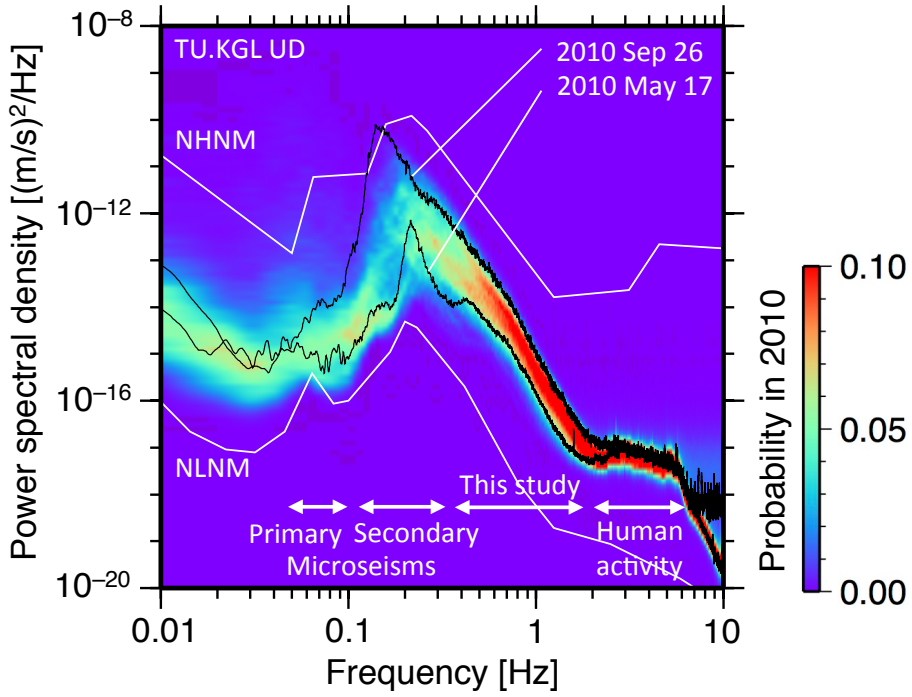

Figure 5.2. Power spectral density of vertical-component ambient noise at the central station, TU.KGL. Color shows probability of power spectra. Since the probability is computed from daily power spectra, the probability of 0.1 at a bin means that the power spectra of 36.5 days distribute in that bin. Two white lines show New Low Noise Model (NLNM) and New High Noise Model (NHNM) [Peterson, 1993]. Two black lines are power spectra on 17 May 2010 and on 26 Sep 2010.

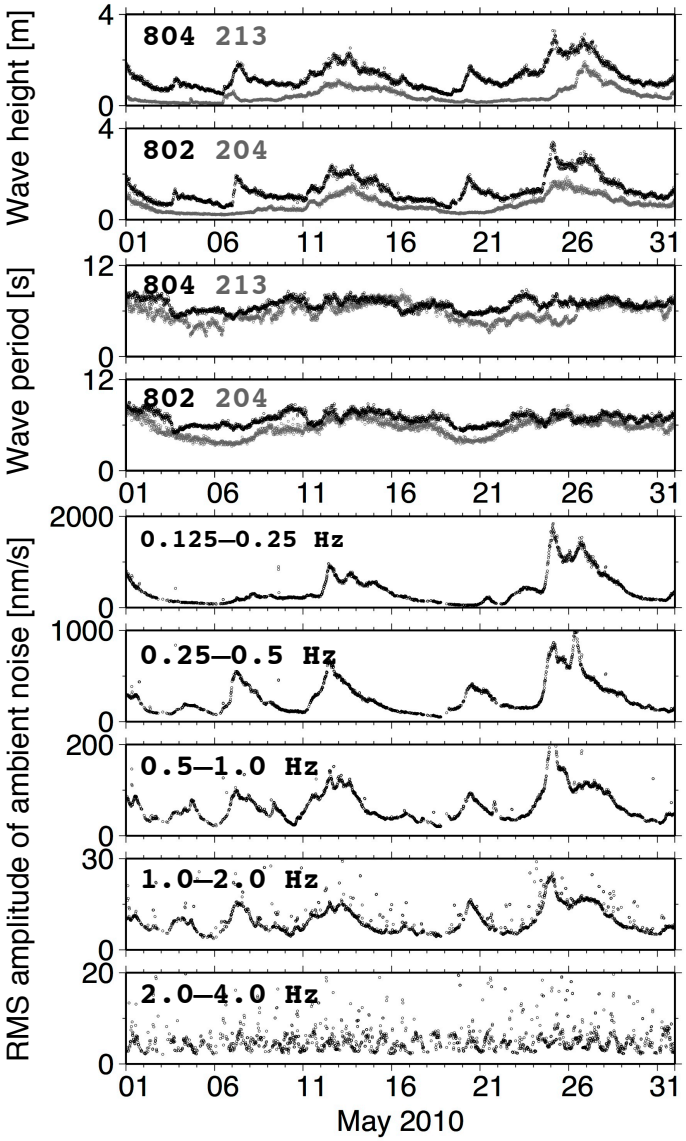

Figure 5.3. Temporal variation in the significant wave height (top), the significant wave period (middle), and the RMS amplitude of vertical-component ambient noise at the central seismic station (bottom). Ocean waves are observed at NOWPHAS station and buoys.

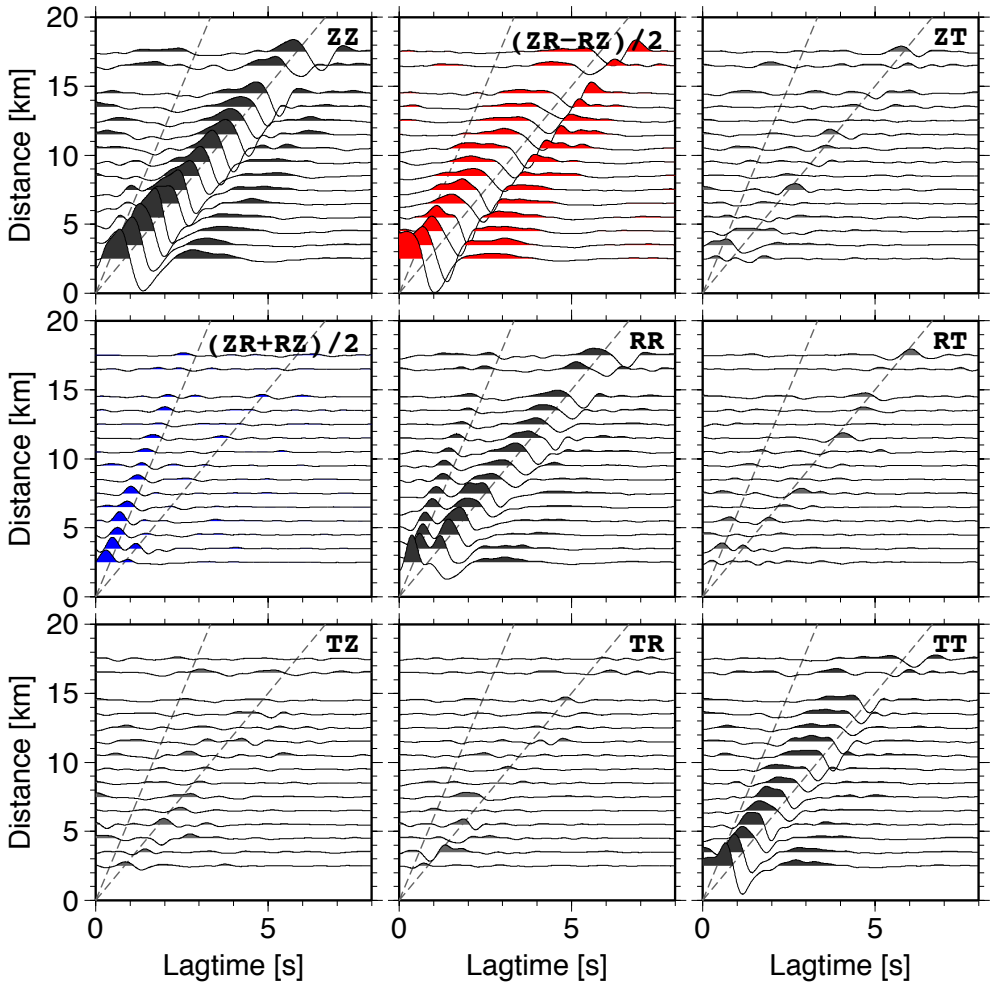

Figure 5.4. Observed cross-correlation tensor of ambient noise at Tono array. The cross-correlation functions are averaged over one year in 2010. The frequency range is 0.25-2.0 Hz. We show the sum and difference of ZR and RZ components (red and blue) instead of ordinary ZR and RZ components. In the ZR+RZ component, the time-antisymmetric part of cross-correlation functions is shown. In the other components, the time-symmetric parts are shown. Two gray dashed lines indicate propagation velocities of 6.0 km/s and 3.0 km/s.

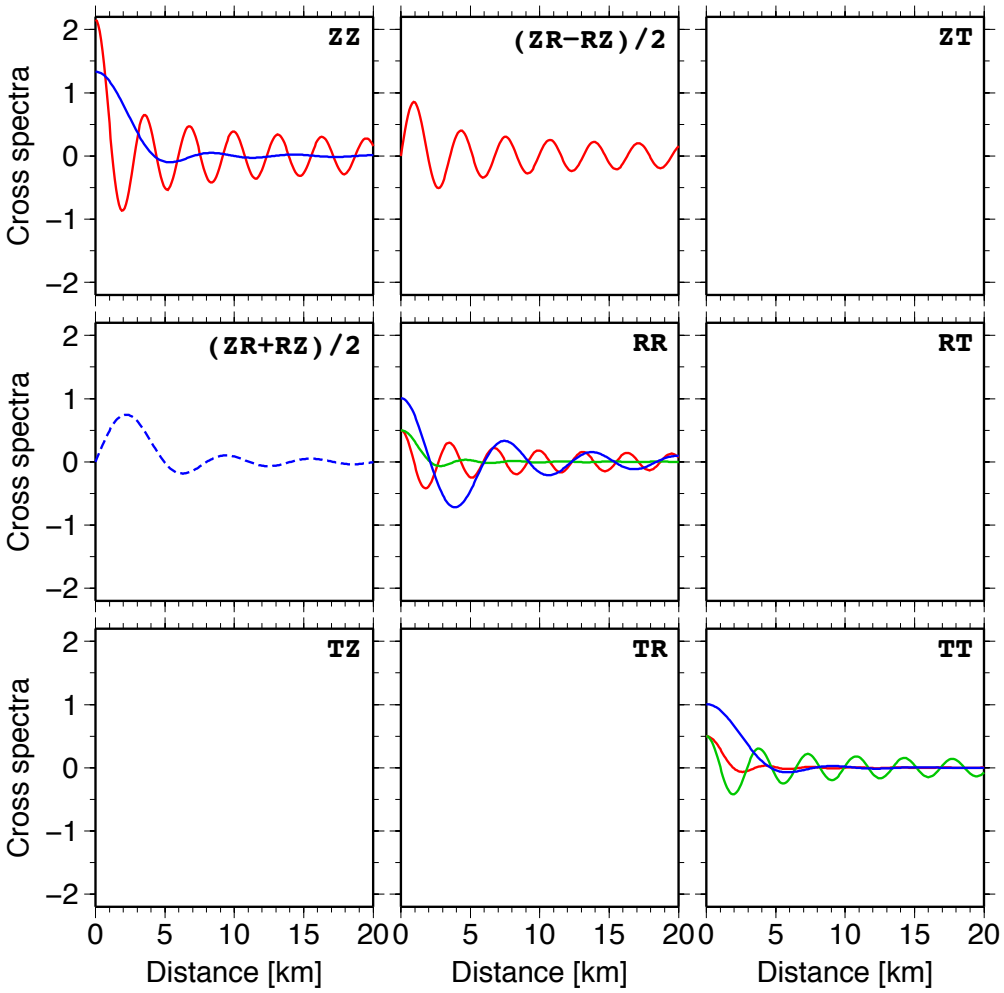

Figure 5.5. Theoretical cross-spectral tensor of Rayleigh (red), Love (green) and P (blue) waves at 1.0 Hz. Parameters are set as $c^R = 3.0$ km/s, $c^L = 3.46$ km/s, $c^P = 6.0$ km/s, $V_P/V_S = \sqrt{3}$, $H^2 a_0^R = 1.0$, $a_0^L = 1.0$, $a_0^P = 1.0$, and $H = -0.68$. Solid and dashed lines indicate real and imaginary parts of the cross spectra, respectively. Absence of solid and/or dashed lines means that the cross spectra is always zero. We again show the sum and difference of ZR and RZ components instead of ZR and RZ components.

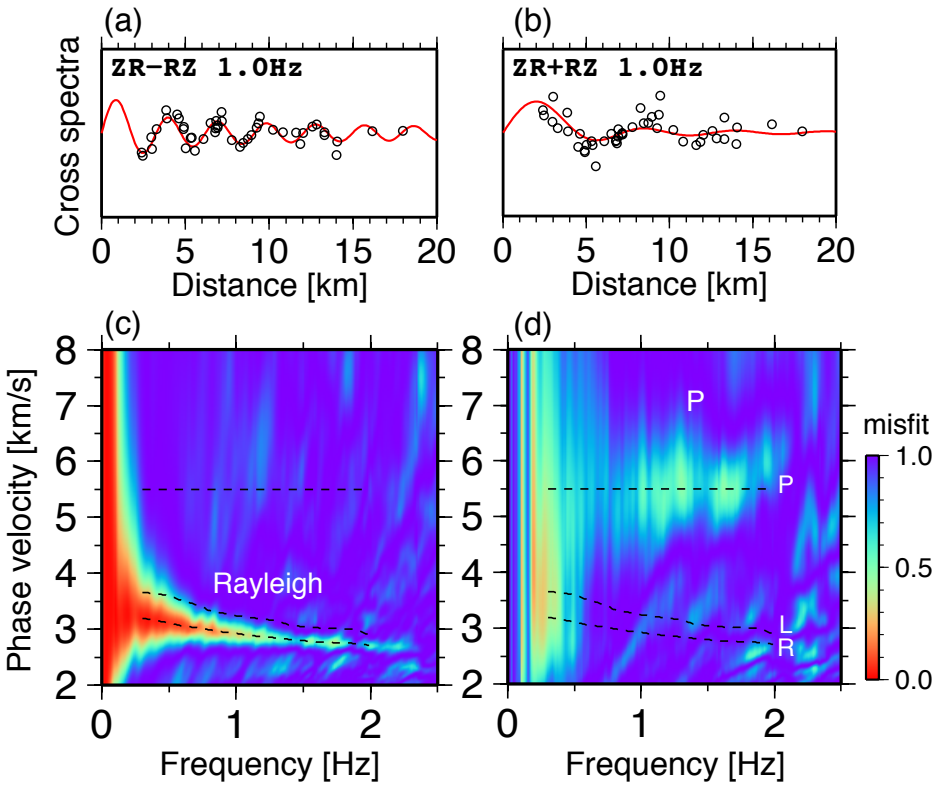

Figure 5.6. (a) Fitting between the observed cross spectra (open circles) and the theoretical cross spectra (red line) at 1.0 Hz for real part of the ZR–RZ component. Vertical axis is arbitrary amplitude. (b) Same as (a), but for imaginary part of the ZR+RZ component. (c) Normalized misfit of the ZR–RZ component with respect to frequency and phase velocity of Rayleigh wave. Broken lines indicate the estimated phase velocity of Rayleigh (slowest one), Love (intermediate one), and P (fastest one) waves. (d) Normalized misfit of the ZR+RZ component with respect to frequency and phase velocity of P wave.

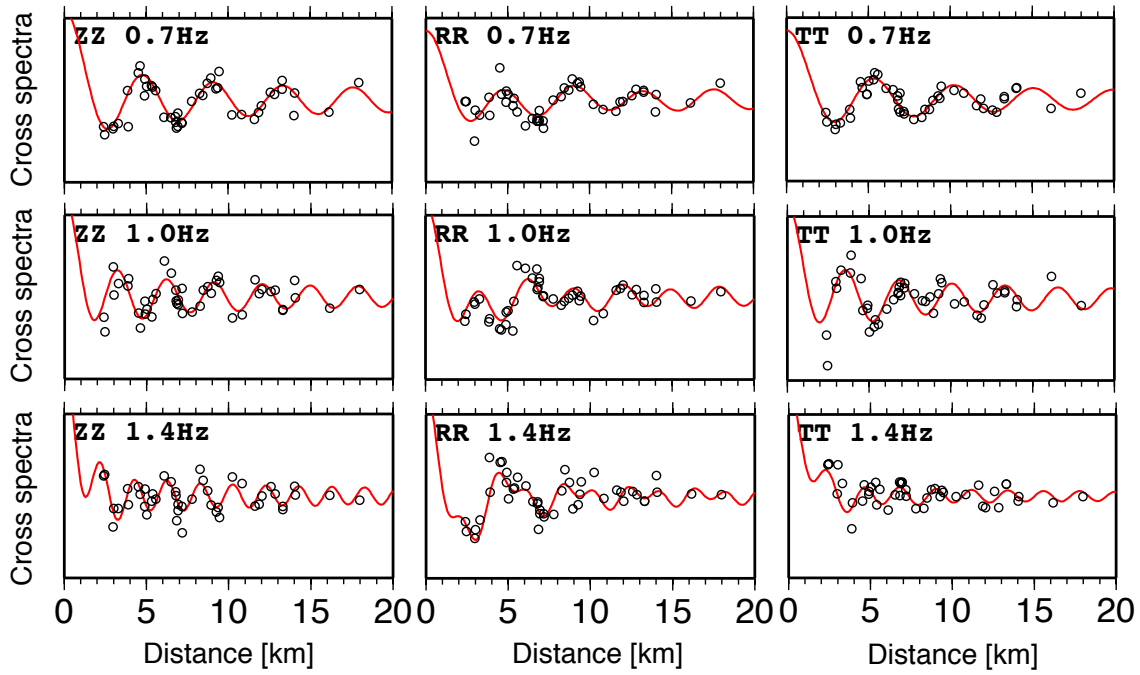

Figure 5.7. Fitting between the observed cross spectra (open circles) and theoretical cross spectra (red lines) of the diagonal components (ZZ, RR, TT) at 0.7, 1.0, and 1.4 Hz. The vertical axis is arbitrary amplitude. Rayleigh and P waves contribute to ZZ component, and Rayleigh, Love, and P waves contribute to RR and TT components.

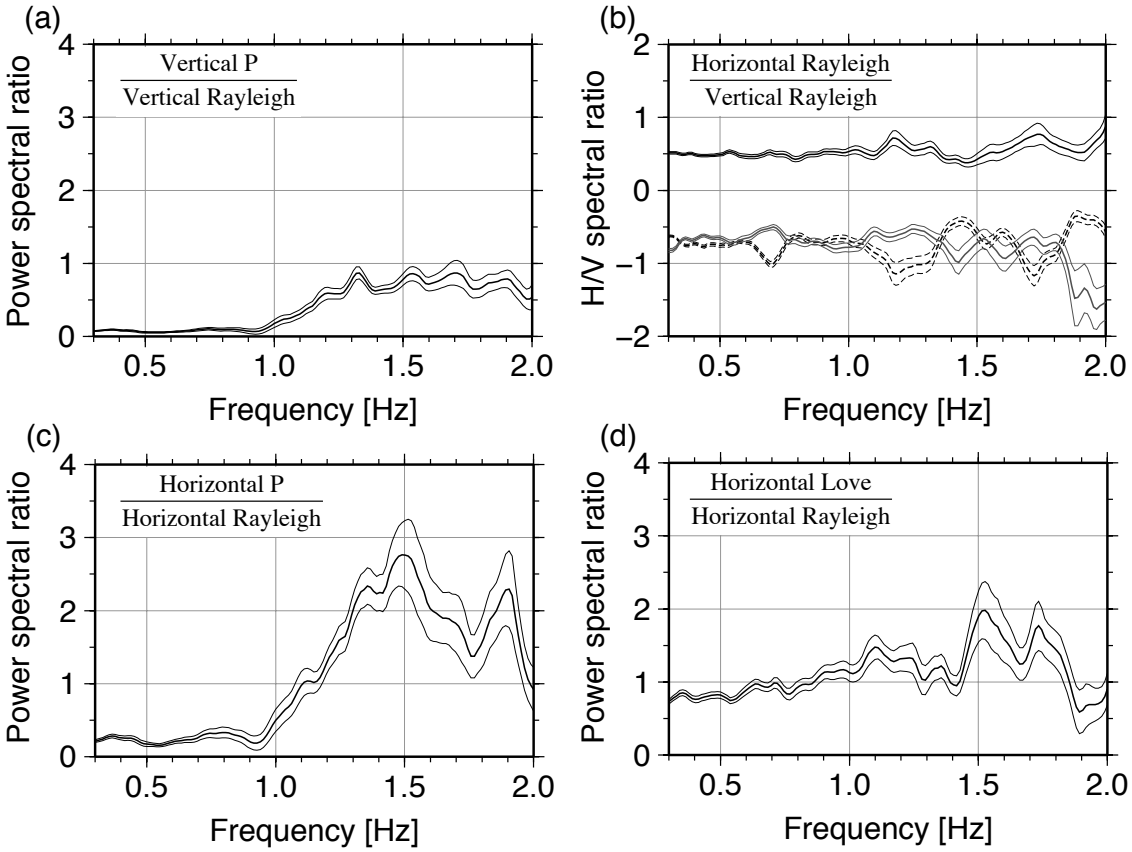

Figure 5.8. Power spectral ratio (a) between P and Rayleigh waves in vertical component, (c) between P and Rayleigh waves in horizontal component, and (d) between Love and Rayleigh waves in horizontal component. Thick and thin lines indicate the average and the standard deviation estimated by a jackknife method. (b) Horizontal-over-vertical ratio of Rayleigh wave. Black solid line is $H^2 a_0^R / a_0^R$, showing the square of the H/V ratio. Dashed line is Ha_0^R / a_0^R, and gray line is $H^2 a_0^R / Ha_0^R$. Here, a_0^R and $H^2 a_0^R$ are estimated from the diagonal component of cross-spectral tensor, and Ha_0^R is estimated from the cross terms of cross-spectral tensor.

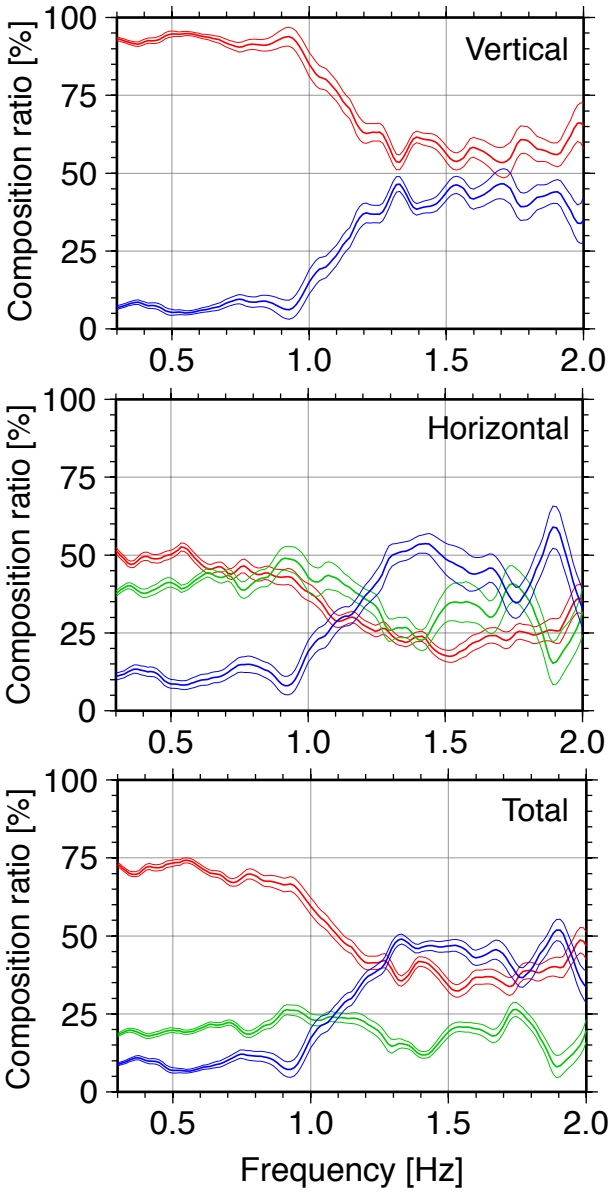

Figure 5.9. Composition ratio of Rayleigh (red), Love (green), and P (blue) waves in vertical (top) and horizontal (bottom) components, and total energy (bottom). Thick and thin lines indicate the estimated value and its standard deviation. The sum of all components is equal to 100%.

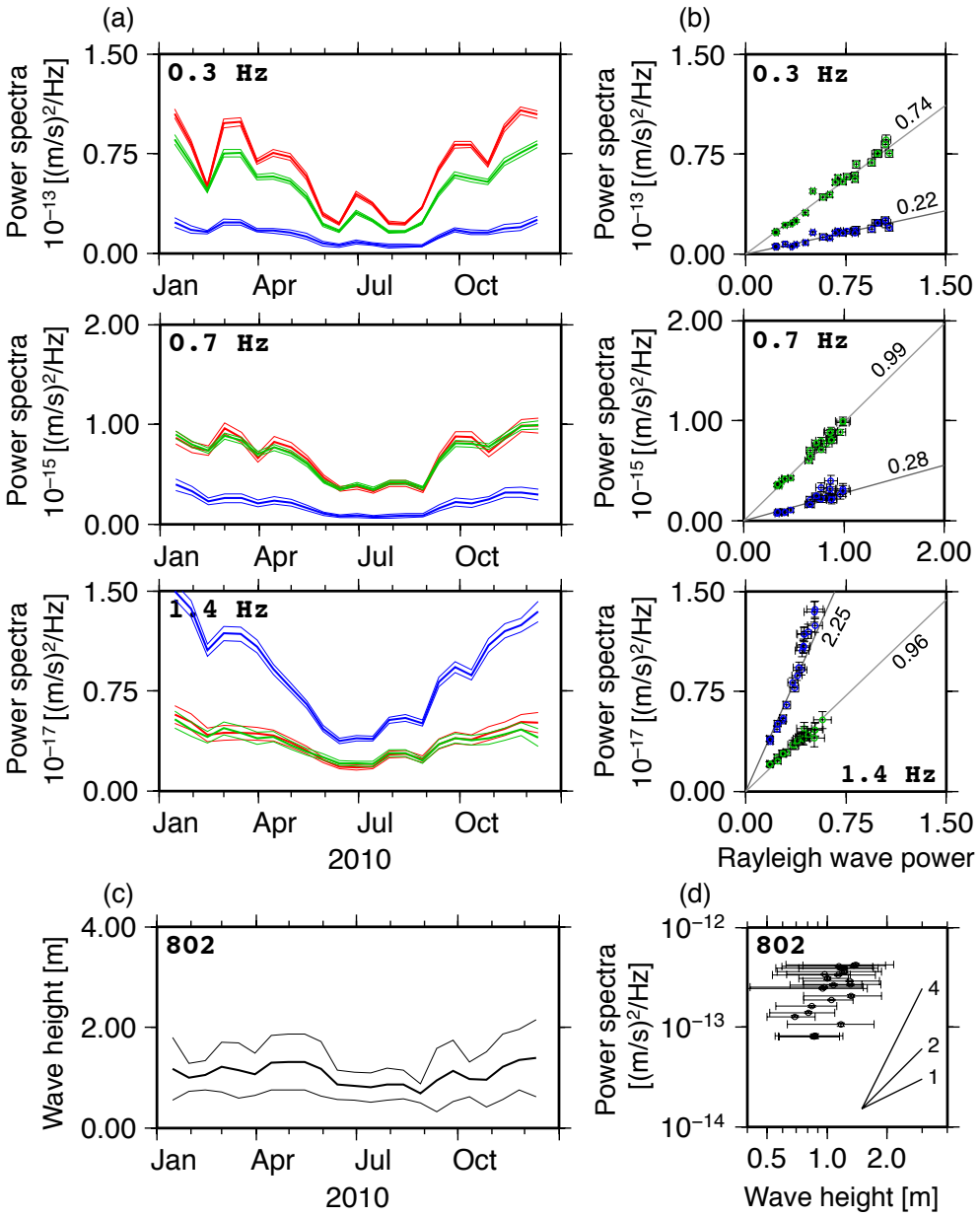

Figure 5.10. Long-term temporal variation in power spectra of seismic waves and in significant wave height of ocean wave. (a) Temporal variation in horizontal-component power spectra of Rayleigh (red), Love (green), and P (blue) waves at three frequencies of 0.3, 0.7, and 1.4 Hz. (b) Love (green) and P (blue) wave powers versus Rayleigh wave power, where the vertical and horizontal axes are the same unit. Gray lines indicate the power spectral ratios that are estimated from the annually averaged cross spectra in 2010. (c) Temporal variation in significant wave height at a NOWPHAS buoy 802. (d) Relationship between the significant wave height at buoy 802 and the vertical-component power spectra of Rayleigh wave at 0.3 Hz. Three lines show slops of 1st, 2nd, and 4th power of the significant wave height.

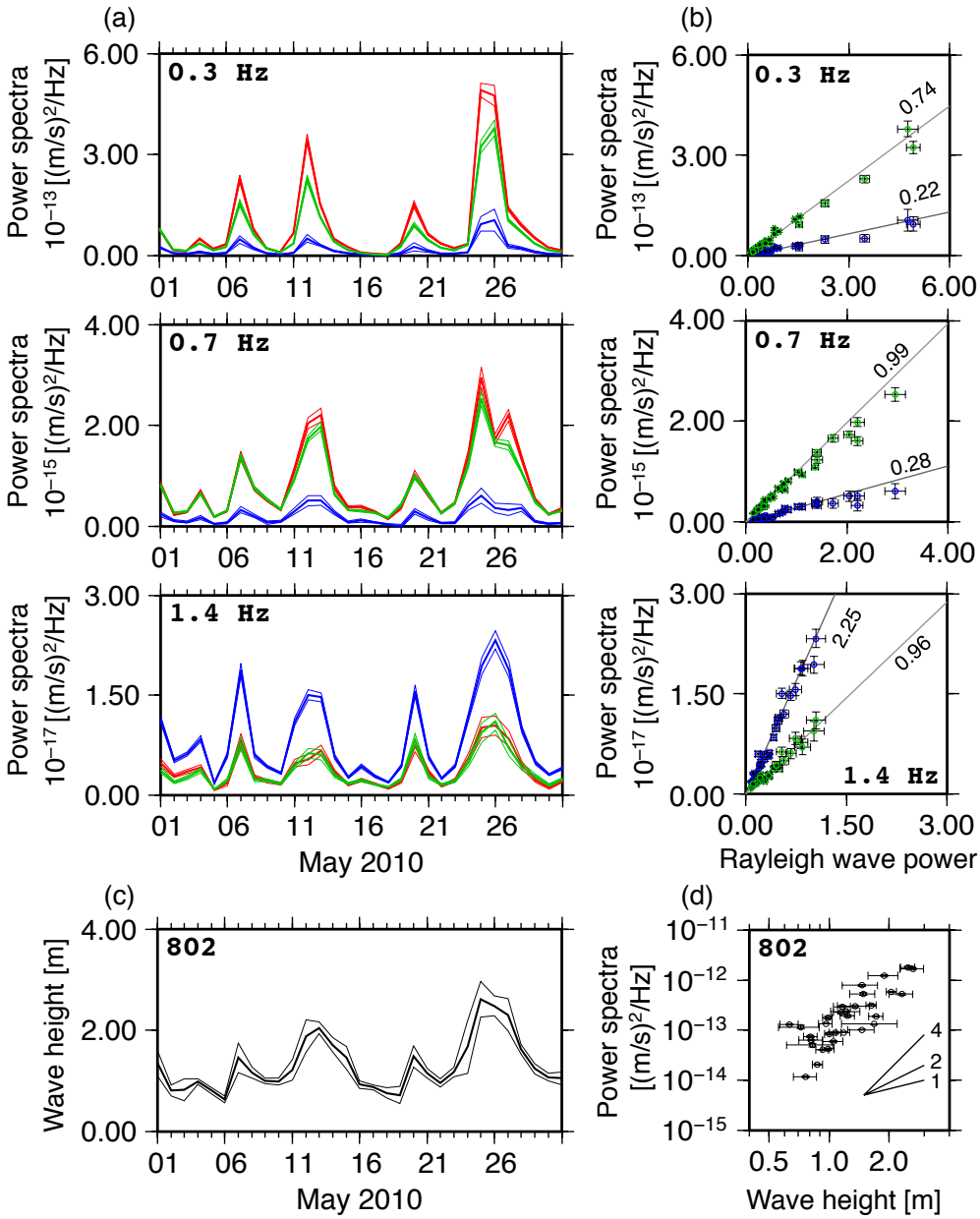

Figure 5.11. Short-term temporal variation in power spectra of seismic waves and in significant wave height of ocean wave. The following explanation is the same as Figure 5.10. (a) Temporal variation in horizontal-component power spectra of Rayleigh (red), Love (green), and P (blue) waves at three frequencies of 0.3, 0.7, and 1.4 Hz. (b) Love (green) and P (blue) wave powers versus Rayleigh wave power, where the vertical and horizontal axes are the same unit. Gray lines indicate the power spectral ratios that are estimated from the annually averaged cross spectra in 2010. (c) Temporal variation in significant wave height at a NOWPHAS buoy 802. (d) Relationship between the significant wave height at buoy 802 and the vertical-component power spectra of Rayleigh wave at 0.3 Hz. Three lines show slops of 1st, 2nd, and 4th power of the significant wave height.

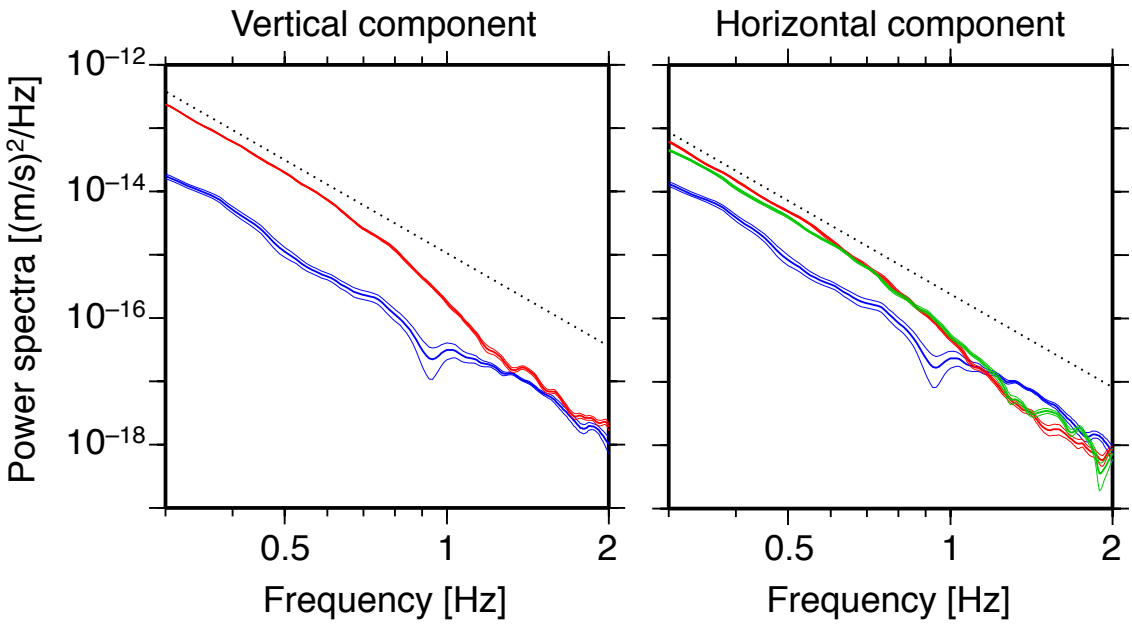

Figure 5.12. Absolute amplitude of power spectra of the three wave modes in vertical (left) and horizontal (right) components. Red is Rayleigh wave, green is Love wave, blue is P wave. Thick and thin lines indicate the average and the standard deviation estimated by a jackknife method. We plotted dotted lines just as references.

6. Discussion

6.1. Answer to the Question in Chapter 3

In Chapter 3, we examined the frequency dependence of coseismic phase velocity change of Rayleigh wave, applying the SPAC method to vertical-component record at Tono array. For the application of the SPAC method, we assumed a predominance of the fundamental mode of Rayleigh wave in ambient noise. The obtained coseismic phase velocity change shows two characteristics: linear increase in 0.3-1.1 Hz and complex behavior above 1.2 Hz (Figure 3.9). The linear increase with respect to frequency can be interpreted by the near-surface velocity reduction up to 5-10% revealed in Chapter 2 and the sensitivity kernels of phase velocity of Rayleigh wave. However, the interpretation of the strange behavior above 1.2 Hz remained as a question while the phase velocity change at high frequencies is important for giving a constraint to the determination of the depth extent of the velocity change.

In Chapter 5, we extended our analysis to three-component record, showing the clear P wave propagation in the cross-correlation tenor of ambient noise. Furthermore, we developed a method to estimate power spectrum of each wave mode by fitting theoretical cross-spectral tensor to the observed cross-spectral tensor. The analysis reveals that the composition of ambient noise changes at 1 Hz significantly. At lower frequencies blew 1 Hz, the vertical-component composition ratios of Rayleigh and P waves are 90-95% and 5-10%, respectively, indicating the predominance of Rayleigh wave. On the other hand, at higher frequencies above 1 Hz, the P wave composition suddenly increases and reaches 40-45%.

The significant P waves cause a bias of the phase velocity measurement based on the SPAC method that assumes a predominance of Rayleigh wave. The bias may be critical especially for detecting subtle temporal changes of the order of 0.1%. Figure 6.1 shows the coincidence of changes in the phase velocity decrease and the composition ratio, suggesting the strange behavior of the phase velocity change above 1.2 Hz is due to the contamination of P wave. We consider that this is the answer to the question. The answer tells us that we should use ambient noise carefully, considering the composition of ambient noise.

However, Chapter 4 provides a way to overcome the problem of the body wave contamination. The key is the use of sum and difference between ZR and RZ correlation. Figure 6.2 shows the observed cross-correlation tensor band-pass-filtered from 1.2 to 2.0 Hz. We can recognize significant P waves in small separation distance from 3 to 9 km in ZZ component. In such case, group velocity filter is not effective because of poor separation of Rayleigh and P wave in time domain. In contrast, the sum and difference of ZR and RZ efficiently separate Rayleigh and P waves. The separation will allow us to conduct a robust estimation of phase velocity of Rayleigh wave even where ambient noise contains P waves comparable to Rayleigh wave.

6.2. Future Work

Near-surface velocity changes have been confirmed by previous studies and by the present study. However, the existence of more deep change is still unknown. For studying velocity change at depth, repeating earthquakes and long-period surface waves are useful. We should remember that near surface change also affect the measurement using repeating earthquakes and long-period surface waves. For stripping the near surface effect, more understanding of near surface velocity change is important.

Mechanisms of velocity change including postseismic recovery have also not been clarified completely. Sawazaki and Snieder [2013] suggested that the use of P- and S-wave velocity and anisotropy provides a way to approach the mechanism of velocity change. The measurement of multiple subsurface properties including non-seismological parameter, such as crustal deformation and water level, will help to clarify the mechanism of seismic velocity change.

Preseismic velocity changes could precede coseismic velocity changes. Indeed, Niu et al. [2008] reported preseismic velocity changes measured at the San Andreas Fault Observatory at Depth (SAFOD) drilling site in Parkfield for small earthquakes. They owed the success to the high-accuracy measurement of experimental data. To detect preseismic velocity change from passive data, we should improve the measurement precision of velocity change with a development of measurement technique [Schaff, 2012; Schaff and Kim, 2012].

For use of ambient noise, we should gain knowledge of the nature of ambient noise. The characteristics of ambient noise depend on site condition and noise source properties [Bonnefoy-Claudet et al., 2006]. Therefore, broadband and broad-area analysis is necessary for better understanding the nature of ambient noise.

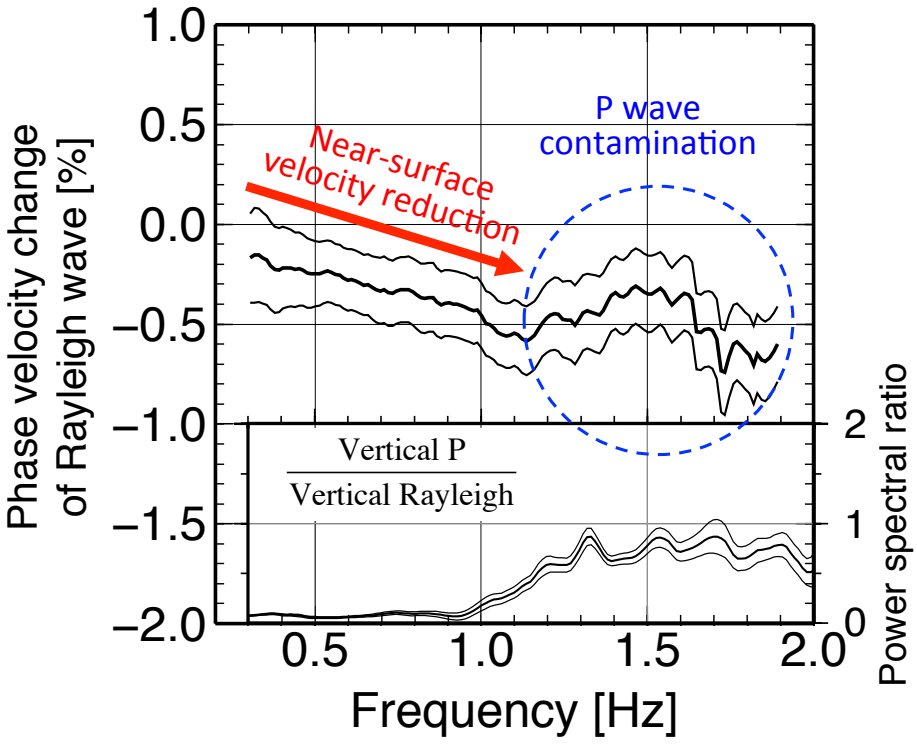

Figure 6.1. Interpretation of coseismic phase velocity change of Rayleigh wave. Phase velocity change of Rayleigh wave is obtained in Chapter 3 and same as Figure 3.9, and power spectral ration is obtained in Chanpter 5 and same as Figure 5.8(a).

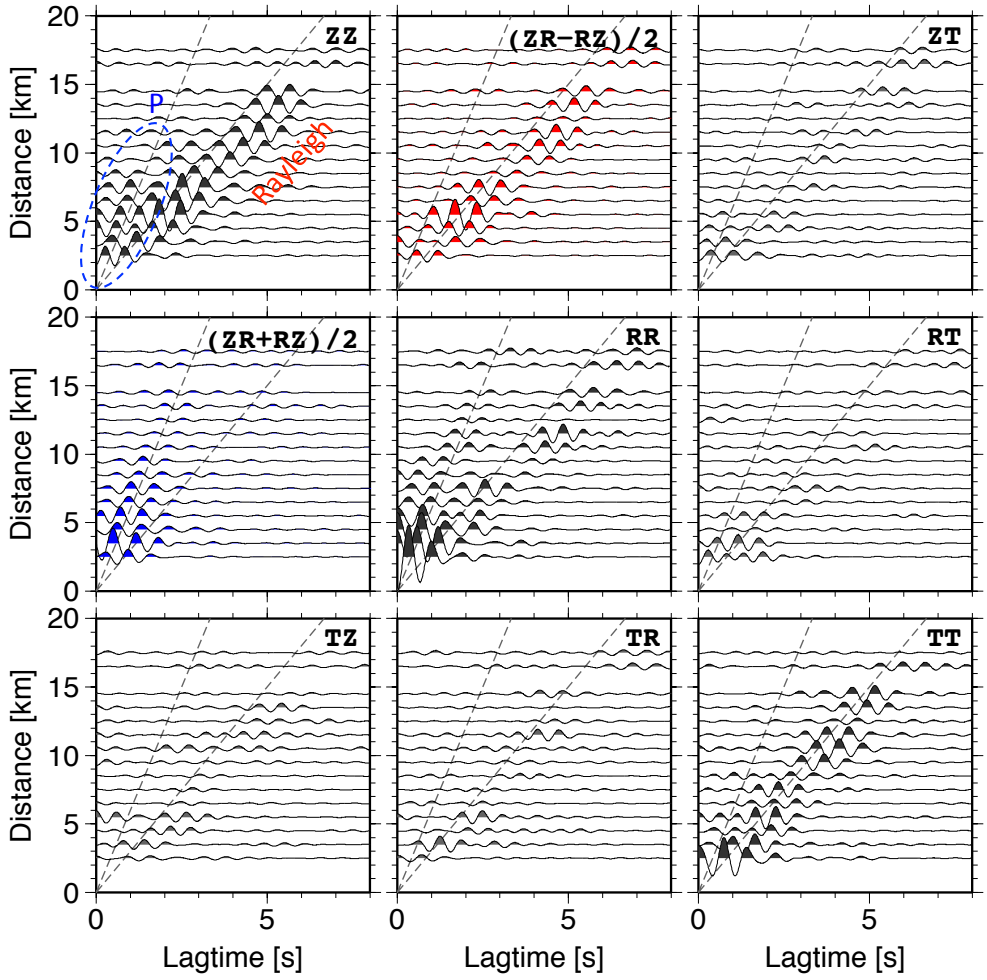

Figure 6.2. Observed cross-correlation tenor in 2010 with a band-pass filter of 1.2-2.0 Hz against their separation distance and time lag. Cross-correlation functions are averaged within bins of 1 km separation distance. ZR+RZ component shows the time-antisymmetric part of cross-correlation functions. The other components show the time-symmetric part of cross-correlation functions. Gray broken lines indicate 6.0 km/s and 3.0 km/s.

7. Conclusions

I dealt with four subjects to deepen our knowledge of temporal change in subsurface structure related to the 2011 Tohoku-oki earthquake based on seismic interferometry. With developments of seismic interferometry for measuring velocity change and for estimating wavefield composition, I succeeded in consistently interpreting two observed results from KiK-net and Tono array data. The obtained results suggest that the velocity change is mainly localized within near-surface layer.

In Chapter 2, I examined the temporal change in shear velocity and polarization anisotropy associated with the 2011 Tohoku-oki earthquake using KiK-net vertical array data. Shear velocity decrease up to 5-10% were widely observed in NE Japan. A correlation between dynamic strain due to strong motion and travel-time shift suggest damage due to the strong motion reduced the near-surface shear modulus. At five stations in Ibaraki prefecture, the time shifts are almost constant regardless of different borehole depths. The fact implies that major velocity decrease is localized in shallow layer up to 100 m at least at the five stations. In contrast to the large shear velocity reduction, change in polarization anisotropy is small. No change in fast direction of anisotropy was observed, suggesting the static stress change is not sufficient to change the crack orientations and/or the principal axes of crustal stress field. Anisotropy amplitude changes were observed in wide area. Static stress change and/or strong ground motion might affect the anisotropy amplitude.

In Chapter 3, I investigated temporal change in phase velocity of Rayleigh wave using ambient noise observed at Tono array. I developed a method to estimate the phase velocity and noise source distribution simultaneously based on the spatial auto-correlation (SPAC) method. With the method, I showed that the suppression of apparent velocity change due to the temporal change in noise source distribution at 0.4 Hz. The frequency-domain SPAC method provided a phase velocity measurement in a wide frequency band of 0.3-1.9 Hz with a high frequency resolution of 0.3 Hz. In 0.3-1.1 Hz, coseismic change in phase velocity at the time of the Tohoku-oki earthquake shows larger decrease at higher frequency by from –0.1% to –0.5%, which is consistent with the near-surface velocity reduction. However, above 1.2 Hz, the phase velocity change shows more complicated behavior. This is a question that remains in Chapter 3.

In Chapter 4, I developed a novel method to separate rectilinear P and elliptic Rayleigh wave with the cross terms of the cross-correlation tensor of ambient noise. Based on wave theory, I found two fundamental characteristics of the cross terms of cross-correlation tensor of uncorrelated plane waves. One is that vertical-radial (ZR) and radial-vertical (RZ) components have the opposite signs for Rayleigh wave and the same signs for P waves. The other is that ZR and RZ components are time-symmetric for Rayleigh wave and time-antisymmetric for P wave in the case of isotropic wave incidence. Accordingly, by just taking the time-antisymmetric part of sum and the time-symmetric part of difference between ZR and RZ components, we can separate P and Rayleigh waves. The key of the fundamental characteristics is

the difference in polarization between elliptic Rayleigh and rectilinear P waves. Using the characteristics, we succeeded in separating P and Rayleigh waves of field data at Tono array. This data analysis validated the method. This study proposed a way to make effective use of three-component observation of ambient noise.

In Chapter 5, I revealed the composition of ambient noise at Tono array. The cross-correlation tensor of ambient noise retrieved Rayleigh, Love, and P waves. In order to estimate power of each wave mode, I extended the SPAC method to body wave incidence. The extended SPAC method shows a good agreement between the theoretical and observed cross spectra. By fitting the theoretical cross spectra to the observed cross spectra, I estimated the composition ratio of each wave mode. The composition of ambient noise significantly changes at 1 Hz. Below 1 Hz, the P wave composition in total power is 5-15% and the lowest one in those of three wave modes. Above 1 Hz, the P wave composition suddenly increases and reaches 50% and the highest one. The change at 1 Hz is attributed to attenuation of high-frequency surface waves because the decay rate of the absolute value of power spectra of surface waves gets steeper around 1 Hz as compared with the constant decay of P wave. In addition, while the power spectrum of each wave mode shows the long-term and short-term variations coincident with the offshore significant wave height, the ratio of the power spectra depend little on time. The fact suggests that all of Rayleigh, Love, and P waves have the same origin and the source-receiver distance varies little with time. Therefore, near coastal region is the dominant source area of the observed ambient noise.

The composition of ambient noise revealed in Chapter 5 gives an answer to the question in Chapter 3. The significant P wave above 1 Hz causes a bias of the phase velocity measurement by the SPAC method that assumes the predominance of Rayleigh wave, which results in the complicated behavior of the phase velocity changes at high frequencies. A way to overcome the contamination is proposed in Chapter 4. More robust estimation will be possible by separating body and Rayleigh waves using the sum and difference of ZR and RZ correlations. The robust estimation in higher frequencies may allow us to estimate the depth extent of the velocity change with high depth resolution.

Seismic interferometry is a powerful tool to monitor subsurface structure. For use of ambient noise data, we should consider the effects of temporal change in noise source distribution and contamination of other wave mode to correctly interpret observed temporal velocity variation as demonstrated in Chapter 3 and Chapter 5. Moreover, the present study shows that we should make effective use of three-component array observation for detecting change in not only velocity but also anisotropy, for minimizing the effect of change in noise source distribution, for measuring velocity change in wide frequency range with high frequency resolution, for separating body and Rayleigh waves, and for understanding the composition of ambient noise.

References

Abe, S., E. Kurashimo, H. Sato, N. Hirata, T. Iwasaki, and T. Kawanaka (2007), Interferometric seismic imaging of crustal structure using scattered teleseismic waves, *Geophys. Res. Lett., 34*, L19305, doi:10.1029/2007GL030633.

Abramowitz, M. and I.A. Stegun (1972), *Handbook of Mathematical Functions with Formulas, Graphs, and Mathematical Tables*, Dover Publications, New York.

Aki, K. (1957), Space and time spectra of stationary stochastic waves, with special reference to microseisms, *Bull. Earthquake Res. Inst. Univ. Tokyo, 35,* 415–456.

Aki, K., and P. G. Richard (2002), *Quantitative Seismology*, 2nd ed, Univ. Sci., Sausalito, Calif.

Asano, Y., T. Saito, Y. Ito, K. Shiomi, H. Hirose, T. Matsumoto, S. Aoi, S. Hori, and S. Sekiguchi (2011), Spatial distribution and focal mechanisms of aftershocks of the 2011 off the Pacific coast of Tohoku earthquake, *Earth Planets Space, 63*, 669–673, doi:10.5047/eps.2011.06.01.

Bensen, G. D., M. H. Ritzwoller, M. P. Barmin, A. L. Levshin, F. Lin, M. P. Moschetti, N. M. Shapiro, and Y. Yang (2007), Processing seismic ambient noise data to obtain reliable broad-band surface dispersion measurements, *Geophys. J. Int., 169*, 1239–1260, doi:10.1111/j.1365-246X.2007.03374.x.

Boness, N. L., and M. D. Zoback (2006), A multiscale study of the mechanisms controlling shear velocity anisotropy in the San Andreas Fault Observatory at Depth, *Geophysics, 71*(5), doi:10.1190/1.2231107.

Bonnefoy-Claudet, S., F. Cotton, and P. Bard (2006), The nature of noise wavefield and its applications for site effects studies—A literature review, *Earth Sci. Rev., 79*, 205–227, doi:10.1016/j.earscirev.2006.07.004.

Bostock, M. G. (1998), Mantle stratigraphy and evolution of the Slave province, *J. Geophys. Res., 103*, 21183–21200, doi:10.1029/98JB01069.

Boué, P., P. Poli, M. Campillo, H. Pedersen, X. Briand, and P. Roux (2013), Teleseismic correlations of ambient seismic noise for deep global imaging of the Earth, *Geophys. J. Int., 194*, 844-848, doi:10.1093/gji/ggt160.

Brenguier, F., N. M. Shapiro, M. Campillo, A. Nercessian, and V. Ferrazzini (2007), 3-D surface wave tomography of the Piton de la Fournaise volcano using seismic noise correlations, *Geophys. Res. Lett., 34*, L02305, doi:10.1029/2006GL028586.

Brenguier, F., M. Campillo, C. Hadziioannou, N. M. Shapiro, R. M. Nadeau, and E. Larose (2008), Postseismic relaxation along the San Andreas Fault at Parkfield from continuous seismological observation, *Science, 321*, 1478-1481, doi:10.1126/science.1160943.

Campillo, M., and A. Paul (2003), Long-range correlations in the diffuse seismic coda, *Science, 299*, 547–549, doi:10.1126/science.1078551.

Capon, J., (1969), High-resolution frequency–wavenumber spectrum analysis, *IEEE*, 1408–1419, doi:10.1109/PROC.1969.7278.

Capon, J., R. J. Greenfield, R. J. Kolker (1967), Multidimensional maximum-likehood processing of a large-aperture seismic array, *IEEE*, 192–211, doi:10.1109/PROC.1967.5439.

Chouet, B., G. De Luca, G. Milana, P. Dawson, M. Martini, and R. Scarpa (1998), Shallow velocity of Stromboli volcano, Italy, derived from small-aperture array measurements of Strombolian tremor, *Bull. Seismol. Soc. Am.*, *88* (3), 653–666.

Claerbout, J. (1968), Synthesis of a layered medium from its acoustic transmission response, *Geophysics, 33*(2), 264–269, doi:10.1190/1.1439927.

Cox, H. (1973), Spatial correlation in arbitrary noise fields with application to ambient sea noise, *J. Acoust. Soc. Am., 54*, 1289–1301, doi:10.1121/1.1.914426.

Derode, A., E. Larose, M. Tanter, J. de Rosny, A. Tourin, M. Campillo, and M. Fink (2003), Recovering the Green's function from field-field correlations in an open scattering medium (L), *J. Acoust. Soc. Am., 113*, 2973–2976, doi:10.1121/1.1570436.

Duvall, T. L., S. M. Jeffferies, J. W. Harvey, and M. A. Pomerantz (1993), Time-distance helioseismology, *Nature, 362*, 430–432, doi:10.1038/ 362430a0.

Flinn, E. A. (1965), Signal analysis using rectilinearity and direction of particle motion, *Proc. IEEE, 53*, 1874–1876, doi:10.1109/PROC.1965.4462.

Friedrich, A., F. Kruger, and K. Klinge (1998), Ocean-generated microseismic noise located with the Grafenberg array, *J. Seismol.*, 2, 47–64.

Froment, B., M. Campillo, P. Roux, P. Gouédard, A. Verdel, and R. Weaver (2010), Estimation of the effect of non-isotropic distributed energy on the apparent arrival time in correlations, *Geophysics, 75*, SA85–SA93, doi:10.1190/1.3483102.

Fukao, Y., K. Nishida, and N. Kobayashi (2010), Seafloor topography, ocean infragravity waves and background Love and Rayleigh waves, *J. Geophys. Res., 115*, B04302, doi:10.1029/2009JB006678.

Gerstoft, P., M. C. Fehler, and K. G. Sabra (2006), When Katrina hit California, *Geophys. Res. Lett., 33*, L17308, doi:10.1029/2006GL027270.

Gerstoft, P., P. M. Shearer, N. Harmon, and J. Zhang (2008), Global P, PP, and PKP wave microseisms observed from distant storms, *Geophys. Res. Lett.*, 35, L23306, doi:10.1029/2008GL036111.

Hadziioannou, C., E. Larose, A. Baig, P. Roux, and M. Campillo (2011), Improving temporal resolution in ambient noise monitoring of seismic wave speed, *J. Geophys. Res., 116*, B07304, doi:10.1029/2011JB008200.

Haney, M. M., T. D. Mikesell, K. van Wijk, and H. Nakahara (2012), Extension of the spatial autocorrelation (SPAC) method to mixed-component correlations of surface waves, *Geophys. J.*

Int., 191, 189–206, doi:10.1111/j.1365-246X.2012.05597.x.

Harmon, N., C. Rychert, and P. Gerstoft (2010), Distribution of noise sources for seismic interferometry, *Geophys. J. Int., 183*, 1470–1484, doi:10.1111/j.1365-246X.2010.04802.x.

Hobiger, M., U. Wegler, K. Shiomi and H. Nakahara (2012), Coseismic and postseismic elastic wave velocity variations caused by the 2008 Iwate-Miyagi Nairiku earthquake, Japan, *J. Geophys. Res., 117*, B09313, doi:10.1029/2012JB009402.

Iinuma, T., M. Ohzono, Y. Ohta, and S. Miura (2011), Coseismic slip distribution of the 2011 off the Pacific coast of Tohoku earthquake (M9.0) estimated based on GPS data—Was the asperity in Miyagi-oki ruptured?, *Earth Planets Space, 63,* 643–648, doi:10.5047/eps.2011.06.013.

Iinuma, T., R. Hino, M. Kido, D. Inazu, Y. Osada, Y. Ito, M. Ohzono, H. Tsushima, S. Suzuki, H. Fujimoto, and S. Miura (2012), Coseismic slip distribution of the 2011 off the Pacific Coast of Tohoku earthquake (M 9.0) refined by means of seafloor geodetic data, *J. Geophys. Res., 117*, B07409, doi:10.1029/2012JB009186.

Ito, Y. and K. Shiomi (2012), Seismic scatterers within subducting slab revealed from ambient noise autocorrelation, *Geophys. Res. Lett., 39*, L1903, doi:10.1029/2012GL053321.

Ito, Y., K. Shiomi, J. Nakajima, and R. Hino (2012), Autocorrelation analysis of ambient noise in northeastern Japan subduction zone, *Tectonophysics*, 572–573, 38–46, doi:10.1016/j.tecto.2011.09.019.

Iwasaki, T., T. Yoshii, T. Moriya, A. Kobayashi, M. Nishiwaki, T. Tsutsui, T. Iidaka, A. Ikami, and T. Masuda (1994), Precise P and S wave velocity structures in the Kitakami Massif, Northern Honshu, Japan, from a seismic refraction experiment, *J. Geophys. Res., 99*(B11), 22187–22204, doi:10.1029/94JB00732.

Kennett, B. L. N. (1991), The removal of free surface interactions from three-component seismograms, *Geophys. J. Int., 104*, 153–163, doi:10.1111/j.1365-246X.1991.tb02501.x.

Koper, K. D., and B. de Foy (2008), Seasonal anisotropy of short-period seismic noise recorded in South Asia, *Bull. Seismol. Soc. Am., 98,* 3033–3045, doi:10.1785/0120080082.

Koper, K. D., B. de Foy, and H. Benz (2009), Composition and variation of noise recorded at the Yellowknife Seismic Array, 1991–2007, *J. Geophys. Res., 114,* B10310, doi:10.1029/2009JB006307.

Koper K. D., K. Seats, and H. Benz (2010), On the composition of Earth's short-period seismic noise field, *Bull. Seismol. Soc. Am., 100*, 606–617, doi:10.1785/0120090120.

Lacoss, R. T., E. J. Kelly, T. M. Nafi (1969), Estimation of seismic noise structure using arrays, *Geophysics, 34*(1), 21–38, doi:10.1190/1.1439995.

Lamb, H. (1904), On the Propagation of Tremors over the Surface of an Elastic Solid, *Phil. Trans. R. Soc. Lond. A., 203*, doi:10.1098/rsta.1904.0013

Landès, M., F. Hubans, N. M. Shapiro, A. Paul, and M. Campillo (2010), Origin of deep ocean microseisms by using teleseismic body waves, *J. Geophys. Res., 115*, B05302, doi:10.1029/2009JB006918.

Lin, F.C., V.C. Tsai, B. Schmandt, Z. Duputel, and Z. Zhan (2013), Extracting Seismic Core Phases with Array Interferometry, *Geophys. Res. Letts., 40*, doi:10.1002/grl.50237.

Lobkis, O. I., and R. L. Weaver (2001), On the emergence of the Green's function in the correlations of a diffuse field, *J. acoust. Soc. Am., 110*, 3011–3017, doi:10.1121/1.1417528.

Longuet-Higgins, M. S. (1950), A theory of origin of microseisms, *Philos. Trans. R. Soc. London, Ser. A*, *243*, 1–35, doi:10.1098/rsta.1950.0012.

Love, A. E. H. (1927), *Mathematical Theory of Elasticity*, Cambridge Univ., Cambridge, U. K.

Maeda, T., K. Obara, and Y. Yukutake (2010), Seismic Velocity Decrease and Recovery Related to Earthquake Swarms in a Geothermal Area, *Earth Planets Space*, *62*, 685–691, doi:10.5047/eps.2010.08.006.

Meier, U., N. M. Shapiro, and F. Brenguier (2010), Detecting seasonal variations in seismic velocities within Los Angeles basin from correlations of ambient seismic noise, *Geophys. J. Int., 181*, 985–996, doi:10.1111/ j.1365-246X.2010.04550.x.

Minato, S., T. Tsuji, S. Ohmi, and T. Matsuoka (2012), Monitoring seismic velocity change caused by the 2011 Tohoku-oki earthquake using ambient noise records, *Geophys. Res. Lett., 39*, L09309, doi:10.1029/ 2012GL051405.

Miyazawa, M., R. Snieder, and A. Venkataraman (2008), Application of seismic interferometry to exptract P- and S-wave propagation and observation of shaear-wave splitting from noise data at Cold Lake, Alberta, Canada, *Geophysics, 73*(4), D35–D40, doi:10.1190/1.2937172.

Montalbetti, J. F., and E. R. Kanasewich (1970), Enhancement of teleseismic body phases with a polarization filter, *Geophys. J. R. Astr. Soc., 21*, 119–129, doi:10.1111/j.1365-246X.1970.tb01771.x.

Nagaoka, Y., K. Nishida, Y. Aoki, and M. Takeo (2010), Temporal change of phase velocity beneath Mt. Asama, Japan, inferred from coda wave interferometry, *Geophys. Res. Lett., 37*, L22311, doi:10.1029/2010GL045289.

Nakahara, H. (2006), A systematic study of theoretical relations between spatial correlation and Green's function in one-, two- and three- dimensional random scalar wavefields, *Geophys. J. Int., 167*, 1097–1105, doi:10.1111/j.1365-246X.2006.03170.x.

Nakamura, A., A. Hasegawa, N. Hirata, T. Iwasaki, and H. Hamaguchi (2002), Temporal variations of seismic wave velocity associated with 1998 M6.1 Shizukuishi earthquake, 2002, *Pure Appl. Geophys., 159*, 1183–1204, doi:10.1007/s00024-002-8677-z.

Nakamura, Y. (1989), A method for dynamic characteristics estimation of subsurface using microtremor

on the ground surface, *Quarterly Report Railway Tech. Res. Inst*., *30*(1), 25–30.

Nakata, N., and R. Snieder (2011), Near-surface weakening in Japan after the 2011 Tohoku-Oki earthquake, *Geophys. Res. Lett., 38*, L17,302, doi:10.1029/2011GL048800.

Nakata, N and R. Snieder (2012a), Estimating near-surface shear-wave velocities in Japan by applying seismic interferometry to KiK-net data, *J. Geophys. Res., 117*, B01308, doi:10.1029/2011JB008595.

Nakata, N., and R. Snieder (2012b), Time-lapse change in anisotropy in Japan's near surface after the 2011 Tohoku-Oki earthquake, *Geophys. Res. Lett., 39*, L11313, doi:10.1029/2012GL051979.

Nishida, K., (2013a), Earth's background free oscillations, *Ann. Rev. Earth Planet. Sci*., 41, 719-740, doi:10.1146/annurev-earth-050212-124020.

Nishida, K. (2013b), Global propagation of body waves revealed by cross-correlation analysis of seismic hum, *Geophys. Res. Lett.*, *40*, 1691–1696, doi:10.1002/grl.50269.

Nishida, K., H. Kawakatsu, and K. Obara (2008a), Three-dimensional crustal S wave velocity structure in Japan using microseismic data recorded by Hi-net tiltmeters, *J. Geophys. Res., 113*, B10302, doi:10.1029/2007JB005395.

Nishida, K., H. Kawakatsu, Y. Fukao, and K. Obara (2008b), Background Love and Rayleigh waves simultaneously generated at the Pacific Ocean floors, *Geophys. Res. Lett., 35*, L16307, doi:10.1029/2008GL034753.

Nishida, K., J. P. Montagner, and H. Kawakatsu (2009), Global surface wave tomography using seismic hum, *Science, 326,* 5949, 112, doi:10.1126/science.1176389.

Nishimura, T., N. Uchida, H. Sato, M. Ohtake, S. Tanaka, and H. Hamaguchi (2000), Temporal changes of the crustal structure associated with the M6.1 earthquake on September 3, 1998, and the volcanic activity of Mount Iwate, Japan, *Geophys. Res. Lett., 27*, 2, 269-272.

Nishimura, T., S. Tanaka, T. Yamawaki, H. Yamamoto, T. Sano, M. Sato, H. Nakahara, N. Uchida, S. Hori, and H. Sato (2005), Temporal changes in seismic velocity of the crust around Iwate volcano, Japan, as inferred from analyses of repeated active seismic experiment data from 1998 to 2003, Earth Planets Space, 57, 491–505.

Niu, F., P. G. Silver, T. M. Daley, X. Cheng, and E. L. Majer (2008), Preseismic velocity changes observed from active source monitoring at the Parkfield SAFOD drill site, *Nature, 454*, 204–208, doi:10.1038/nature07111.

Nogoshi, M., T. Igarashi (1971), On the amplitude characteristics of microtremor (part 2). *Journal of Seismological Society of Japan, 24*, 26–40 (In Japanese with English abstract).

Okada, H., (2003), *The Microtremor Survey Method*, Geophys. Monogr. No. 12, Society of Exploration Geophysicists, Tulsa, OK.

Okada, T., K. Yoshida, S. Ueki, J. Nakajima, N. Uchida, T. Matsuzawa, N. Umino, A. Hasegawa, and

Group for the aftershock observations of the 2011 Off the Pacific Coast of Tohoku Earthquake (2011), Shallow inland earthquakes in NE Japan possibly triggered by the 2011 off the Pacific coast of Tohoku Earthquake, *Earth Planets Space, 63*, 749–754, doi:10.5047/eps.2011.06.027.

Okada, Y. (1992), Internal deformation due to shear and tensile faults in a half-space, *Bull. Seismol. Soc. Am., 82,* 1018–1040.

Okada, Y., K. Kasahara, S. Hori, K. Obara, S. Sekiguchi, H. Fujiwara, and A. Yamamoto (2004), Recent progress of seismic observation net- works in Japan—Hi-net, F-net, K-NET and KiK-net—, *Earth Planets Space, 56*, 15–28.

Peng, Z., and Y. Ben-Zion (2006), Temporal changes of shallow seismic velocity around the Karadere-Düzce branch of the North Anatolian Fault and strong ground motion, *Pure Appl. Geophys., 163,* 567–600, doi:10.1007/s00024-005-0034-6.

Peterson, J. (1993), Observations and modeling of seismic background noise, *U. S. Geol. Surv. Open File Rep.*, 93-322.

Poli, P., H. A. Pedersen, M. Campillo, and POLENET LAPNET working group (2012), Emergence of body waves from cross-correlation of seismic noise, *Geophys. J. Int., 188*, 549–558, doi:10.1111/j.1365- 246X.2011.05271.X.

Poupinet, G., W. L. Ellsworth, and J. Frechet (1984), Monitoring velocity variations in the crust using earthquake doublets: An application to the Calaveras Fault, California, *J. Geophys. Res., 89*(B7), 5719–5731, doi:10.1029/JB089iB07p05719.

Press, W. H., B. P. Flannery, S. A. Teukolsky, and W. T. Vetterling (1986), *Numerical Recipes*, Cambridge Univ. Press, Cambridge.

Rost, S., and C. Thomas (2002), Array seismology: Methods and applications, *Rev. Geophys., 40*(3), 1008, doi:10.1029/2000RG000100.

Roux, P. (2005), P-waves from cross-correlation of seismic noise, *Geophys. Res. Lett., 32*, L19303, doi:10.1029/2005GL023803.

Rubinstein, J. L., N. Uchida, and G. C. Beroza (2007). Seismic velocity reductions caused by the 2003 Tokachi-Oki earthquake, *J. Geophys. Res. 112*, B05315, doi 10.1029/2006JB004440.

Sabra, K. G., P. Gerstoft, P. Roux, W. A. Kuperman, and M. C. Fehler (2005), Surface wave tomography from microseisms in Southern California, *Geophys. Res. Lett., 32*, L14311, doi:10.1029/2005GL023155.

Saito, M. (1988), DISPER80: *A subroutine package for the calculation of seismic normal-mode solutions, in Seismological Algorithms: Computational Methods and Computer Programs,* edited by D. J. Doornbos, pp. 293–319, Academic, San Diego, Calif.

Saito, T. (2010), Love wave excitation due to the interaction between a propagating ocean wave and the sea-bottom topography, Geophys. J. Int., 182, 1515–1523, doi:10.1111/j.1365-246X.2010.04695.

Sánchez-Sesma, F. J., and M. Campillo (2006), Retrieval of the Green's function from cross correlation: The canonical elastic problem, *Bull. Seismol. Soc. Am., 96*, 1182–1191, doi:10.1785/0120050181.

Sawazaki, K., and R. Snieder (2013), Time-lapse changes of P- and S-wave velocities and shear wave splitting in the first year after the 2011 Tohoku earthquake, Japan: shallow subsurface, *Geophys. J. Int.*, 193, 238–251, doi:10.1093/gji/ggs080.

Sawazaki, K., H. Sato, H. Nakahara, and T. Nishimura (2006), Temporal change in site response caused by earthquake strong motion as revealed from coda spectral ratio measurement, *Geophys. Res. Lett., 33*, L21303, doi:10.1029/2006GL027938.

Sawazaki, K., H. Sato, H. Nakahara, and T. Nishimura (2009), Time-lapse changes of seismic velocity in the shallow ground caused by strong ground motion shock of the 2000 Western-Tottori Earthquake, Japan, as revealed from Coda deconvolution analysis, *Bull. Seismol. Soc. Am., 99*(1), 352–366, doi:10.1785/0120080058.

Schaff, D. P. (2012), Placing an upper bound on preseismic velocity changes measured by ambient noise monitoring for the 2004 Mw 6.0 Parkfield earthquake (California), *Bull. Seismol. Soc. Am., 102*, 1400–1416, doi:10.1785/0120110342.

Schaff, D. P., and W.-Y. Kim (2012), A rare foreshock sequence of the 20 January 2007 Odaesan, Korea, earthquake to measure the existence of preseismic velocity changes, *J. Geophys. Res., 117*, B06314, doi:10.1029/2012JB009232.

Schuster, G. T., J. Yu, J. Sheng, and J. Rickett (2004), Interferometric/daylight seismic imaging, *Geophys. J. Int., 157*, 838–852, doi:10.1111/j.1365-246X.2004.02251.x.

Sens-Schönfelder, C., and U. Wegler (2006), Passive image interferometry and seasonal variations of seismic velocities at Merapi Volcano, Indonesia, *Geophys. Res. Lett., 33*, L21302, doi:10.1029/2006GL027797.

Shapiro, N. M., and M. Campillo (2004), Emergence of broadband Rayleigh waves from correlations of the ambient seismic noise, *Geophys. Res. Lett., 31*, L07614, doi:10.1029/2004GL019491.

Shapiro, N. M., M. Campillo, L. Stehly, and M. H. Ritzwoller (2005), High-resolution surface-wave tomography from ambient seismic noise, *Science, 307*(5715), 1615–1518, doi:10.1126/science.1108339.

Shimshoni, M., and S. W. Smith (1964), Seismic signal enhancement with three-component detectors, *Geophysics, 29*, 664–671, doi:10.1190/1.1439402.

Snieder, R., A. Grêt, H. Douma, and J. Scales (2002), Coda wave interferometry for estimating nonlinear behavior in seismic velocity, *Science, 295*, 2253–2255, doi:10.1126/science.1070015.

Snieder, R. (2004), Extracting the Green's function from the correlation of coda waves: A derivation based on stationary phase, *Phys. Rev. E, 69*, 046610, doi:10.1103/PhysRevE.69.046610.

Takagi, R., and T. Okada (2012), Temporal change in shear velocity and polarization anisotropy related

to the 2011 M9.0 Tohoku-Oki earthquake examined using KiK-net vertical array data, *Geophys. Res. Lett.., 39*, L09310, doi:10.1029/2012GL051342, Chapter 2 of the present thesis.

Takagi, R., T. Okada, H. Nakahara, N. Umino, and A. Hasegawa (2012), Coseismic velocity change in and around the focal region of the 2008 Iwate-Miyagi Nairiku earthquake, *J. Geophys. Res., 117*, B06315, doi:10.1029/2012JB009252.

Takagi, R., H. Nakahara, T. Kono, and, T. Okada (2014), Separating body and Rayleigh waves with cross terms of the cross-correlation tensor of ambient noise, *J. Geophys. Res.,* accepted, Chapter 4 of the present thesis.

Takeo, A., K. Nishida, T. Isse, H. Kawakatsu, H. Shiobara, H. Sugioka, and T. Kanazawa (2013), Radially anisotropic structure beneath the Shikoku Basin from broadband surface wave analysis of ocean bottom seismometer records, *J. Geophys. Res., Solid Earth, 118*, doi:10.1002/jgrb.50219.

Tokimatsu, K., S. Wakai, H. Arai (1998), Three-dimensional soil stratification using surface waves in microtremors, *Proceeding of the First Conference on Geotechnical Site Characterization*, 537–542.

Tonegawa, T., K. Nishida, T. Watanabe, and K. Shiomi (2009), Seismic interferometry of teleseismic S-wave coda for retrieval of body waves: An application to the Philippine Sea slab underneath the Japanese Islands, *Geophys. J. Int., 178*, 1574–1586, doi:10.1111/j.1365- 246X.2009.04249.X.

Tonegawa, T., Y. Fukao, K. Nishida, H. Sugioka, and A. Ito (2013), A temporal change of shear wave anisotropy within the marine sedimentary layer associated with the 2011 Tohoku-Oki earthquake, *J. Geophys. Res. Solid Earth, 118*, 607–615, doi:10.1002/jgrb.50074.

Ueno, T., T. Saito, K. Shiomi, B. Enescu, H. Hirose, and K. Obara (2012), Fractional seismic velocity change related to magma intrusions during earthquake swarms in the eastern Izu peninsula, central Japan, *J. Geophys. Res., 117*, B12305, doi:10.1029/2012JB009580.

van Wijk, K., T. D. Mikesell, T. Blum, and M. M. Haney (2010), Surface wave isolation with the interferometric Green tensor, *SEG Technical Program Expanded Abstracts, 784*, 3996-4000, doi:10.1190/1.3513692.

van Wijk, K., T. D. Mikesell, V. Schulte-Pelkum, and J. Stachnik (2011), Estimating the Rayleigh-wave impulse response between seismic stations with the cross terms of the Green tensor, *Geophys. Res. Lett., 38*, L16301, doi:10.1029/2011GL047442.

Vidale, J. E. (1986), Complex polarization analysis of particle motion, *Bull. Seism. Soc. Am., 76*, 1393–1405.

Wapenaar, K. (2004), Retrieving the elastodynamic Green's function of an arbitrary inhomogeneous medium by cross correlation, *Phys. Rev. Lett., 93*, 254–301, doi:10.1103/PhysRevLett.93.254301.

Wapenaar, K., and J. Fokkema (2006), Green's function representations for seismic interferometry, *Geophysics, 71*, SI33–SI46, doi:10.1190/1.2213955.

Weaver, R. L. (2005), Information from seismic noise, *Science, 307*, 1568–1569, doi:10.1126/science.1109834.

Weaver, R. L., and O. I. Lobkis (2001), Ultrasonics without a source: Thermal fluctuation correlations at MHz frequencies, *Physical Review Letters, 87*, 134301, doi:10.1103/PhysRevLett.87.134301.

Weaver, R. L., and O. I. Lobkis (2002), On the emergence of the Green's function in the correlations of a diffuse field: Pulse-echo using thermal phonons, *Ultrasonics, 40,* 435–439, doi:10.1016/S0041-624X(02)00156-7.

Weaver, R., B. Froment, and M. Campillo (2009), On the correlation of non-isotropically distributed ballistic scalar diffuse wave, *J. Acoust. Soc. Am., 126*, 1817–1826, doi:10.1121/1.3203359.

Wegler, U., and C. Sens-Schönfelder (2007), Fault zone monitoring with passive image interferometry, *Geophys. J. Int., 168*, 1029–1033, doi:10.1111/j.1365-246X.2006.03284.x.

Wegler, U., H. Nakahara, C. Sens-Schönfelder, M. Korn, and K. Shiomi (2009), Sudden drop of seismic velocity after the 2004 Mw 6.6 mid-Niigata earthquake, Japan, obserbed with passive image interferometry, *J. Geophys. Res., 114*, B06305, doi:10.1029/2008JB005869.

Yamada, M., J. Mori, and S. Ohmi (2010), Temporal changes of subsurface velocities during strong shaking as seen from seismic interferometry, *J. Geophys. Res.*, 115, B03302, doi:10.1029/2009JB006567.

Yamamoto, H. (2000), Estimation of shallow S-wave velocity structures from phase velocities of Love- and Rayleigh-waves in microtremors, *Proceedings of the 12th World Conference on Earthquake Engineering*, Auckland, New Zealand.

Yang, Y., M. Ritzwoller, A. Levshin, and N. Shapiro (2007), Ambient noise Rayleigh wave tomography across Europe, *Geophys. J. Int., 168*, 259– 274, doi:10.1111/j.1365-246X.2006.03203.x.

Yao, H., R. D. Van Der Hilst, and M. V. de Hoop (2006), Surface-wave tomography in SE Tibet from ambient seismic noise and two-station analysis: I. Phase velocity maps, *Geophys. J. Int.*, 166, 732–744, doi:10.1111/j.1365-246X.2006.03028.x.

Yilmaz, O. (1987), *Seismic Data Processing, Investigations in Geophysics*, vol. 2, Soc. Explor. Geophys., Talsa, Okla.

Yoshida, K., A. Hasegawa, T. Okada, T. Iinuma, Y. Ito, and Y. Asano (2012), Stress before and after the 2011 Great Tohoku-oki earthquake, and induced earthquakes in inland areas of eastern Japan, *Geophys. Res. Lett., 39,* L03302, doi:10.1029/2011GL049729.

Zhan, Z., S. Ni, D. V. Helmberger, and R. W. Clayton (2010), Retrieval of Moho-reflected shear wave arrivals from ambient seismic noise, *Geophys. J. Int., 182*, 408–420, doi:10.1111/j.1365-246X.2010.04625.x.

Zhang, J., P. Gerstoft, and P. M. Shearer (2009), High-frequency P-wave seismic noise driven by ocean winds, *Geophys. Res. Lett., 36*, L09302, doi:10.1029/2009GL037761.